Investigation of RF Plasma Spraying Synthesis of Rare Earth Oxide Nano-Materials

Sun Xiao Long

School of Materials Science and Engineering

A thesis submitted to the Nanyang Technological University
in fulfilment of the requirement for the degree of
Doctor of Philosophy

2008

Acknowledgement

I would like to take this opportunity to express my heartfelt gratitude to my supervisor, Asst. Professor Alfred Tok, for his instructive guidance and helpful support throughout the entire work. He has always shown his complete trust in me and gave me sufficient space for my own ideas and directions. His support in my research as well as concern in my personal life has helped me achieve my goals. He has been not only a good mentor and good leader, but also a good friend all this time.

I am very grateful to Dr Rene Huebner for his diligent assistance on the XRD analysis of my research as well as patient instructions and precious suggestions. Also, thanks to Associate Professor Ng Heong Wah and Dr Kang Chang Wei for their important contribution to my modeling work. Thanks to Dr Martin Karl Schreyer for his kind help on my refinement work. I am grateful to my TAC group members Associate Professor Ma Jan, Asst. Professor Gan Chee Lip and Associate Professor Subodh G. Mhaisalkar for their precious comments and suggestions on my first and second year work. In addition, I thank Mr Éric Bouchard from TEKNA Plasma Systems Inc. for his generous technical support of my spraying system. Mr Samsudin Bin Sarim in Ceramics Processing Lab, NTU has provided his very kind and competent support for my experimental work for the three years, so I would like to convey my sincere appreciation to him. Other people I am grateful to are my research group members and friends Su Liap Tat, Happy, and Du Siwei for their encouragement and discussions on my research work. I would also like to thank the financial support of the School of Materials Science & Engineering and the Graduate Scholarship from Nanyang Technological University for my research work.

Finally, I want to express my deepest appreciation to my wonderful parents and my beloved wife, Sha Xuena, for their unselfish love, constant encouragement and support at all times.

Contents

List of Figures

List of Tables

Abstract

Nano rare earth materials have attracted great interest recently due to their unique properties and extensive applications. Among the methods for nano rare earth materials synthesis, plasma spraying is an efficient technique with great potential. However, problems such as clogging and inhomogeneous heating need to be addressed. The present study set out to improve the plasma spraying technique through experiments and modeling work.

Inductively coupled RF plasma (RF-ICP) spraying process was employed to synthesize rare earth oxide nanoparticles using powder feed spraying with Ar and Ar/O_2 plasma. In order to solve the clogging problem in powder spraying, suspension plasma spraying (SPS) was applied. To increase the enthalpy of the system, various solvents were studied and this led to the development of a novel technique named combustion-aided SPS. The morphology, productivity, and crystal structure of the as-sprayed particles were investigated and correlated with processing conditions and numerical modeling results.

Numerical models were built for various plasma fields of Ar, Ar/O_2, and (Ar/O_2+acetone) plasma, using computational fluid dynamics analysis program FLUENT V6.3.2©. The modeling results showed that the plasma field was substantially altered by the introduction of O_2 secondary gas and combustion of acetone solvent. In addition, the plasma and entrained particles' velocities decreased remarkably. Therefore, plasma with O_2 addition and acetone combustion provide an enhanced and more homogeneous heat treatment, as well as a faster quenching to the nanoparticles.

For all spraying schemes, the mean size of the obtained nanoparticles increased with increasing thermodynamic stability of rare earth oxide, and their productivities decreased in the same order. All the as-sprayed particles exhibited an inclination of cubic to monoclinic (C→B) phase transformation induced by plasma treatment, the degree of which varied with materials and processing conditions.

In powder feed spraying by Ar plasma, the resultant micron-sized particles showed both spherical and irregular shapes, suggesting an insufficient heat treatment. There was a wide particle size distribution and evidence of inhomogeneous heat treatment. This was improved when using Ar/O_2 plasma. The O_2 dissociation and recombination process

increased both the heat treatment level and the quenching rate. Consequently, the morphology of the as-sprayed micron-sized particles was improved significantly and the nanoparticles' mean size decreased and size distribution narrowed.

To solve the clogging problem in powder feed, water was used as a solvent for the suspension plasma spraying. However, water evaporation reduced the plasma enthalpy greatly. Application of organic solvents improved this situation to some extent, but induced some carbon-related impurities into the products. A novel technique named combustion-aided SPS was developed and applied. Because of the dual effects of O_2 dissociation-recombination and acetone combustion, the particles underwent an even higher level of heat treatment than powder spraying by Ar/O_2 and the quenching rate increased further. As a result, the particle morphology was improved dramatically and the particle size and distribution further reduced.

Finally, powder feed spraying by Ar plasma was successfully employed to synthesize mixed oxide nanoparticles of $Sm_{2-x}Lu_xO_3$. These as-sprayed mixed oxides particles consisted mainly of monoclinic B-type and cubic C-type solid solution phases. The particles showed a wide size distribution. The larger particles had spherical shape, ranging from submicron to micron size, whereas the nanoparticles were crystallites with a size less than 100 nm in various shapes.

Nomenclature

A	Cross section area (m^2)
B	Empirical constant (= 9.81)
C_D	Drag coefficient
C_μ	Empirical constant (= 0.09)
$C_{1\varepsilon}$	Empirical constant (= 1.44)
$C_{2\varepsilon}$	Empirical constant (= 1.92)
C_p	Specific heat capacity (J/kg K)
D	Diffusion coefficient (m^2/s)
D_p	Particle diameter (m)
E	plasma voltage (V)
G_κ	Product of the eddy viscosity and viscous dissipation terms
H_f	Latent heat of fusion (J/kg)
h	Heat transfer coefficient (W/m^2 K)
I	plasma current (A)
K	von Kármán constant (= 0.42)
k	Thermal conductivity (W/mK)
m	Mass (kg)
n_p	Number of particles
p	Pressure (Pa)
$P_{in}^{'''}$	Constant heat source (W/m^3)
$\dot{q}$	Heat flux (W/m^2)
S_ϕ	Source term
T_A	Plasma temperature at adjacent element to the wall (K)
T_b	Boiling point (K)
T_i	Turbulent intensity (%)
T_m	Melting point (K)
$\boldsymbol{u}$	Velocity vector (m/s)
$\bar{\boldsymbol{u}}$	Velocity vector fluctuation (m/s)
U	Velocity magnitude (m/s)
U_A	Plasma velocity at adjacent element to the wall (m/s)
u, v, w	Velocity components in x, y and z directions, respectively (m/s)

V	Volume (m^3)
Y_n	Mass fraction
y	Distance from element to the wall (m)
y_A	Distance from adjacent element to the wall (m)

Subscripts

∞	Far field region
l	Laminar state
p	Particle
t	Turbulent state

Greek symbols

α	Thermal diffusivity (m^2/s)
ε	Turbulent kinetic energy dissipation rate (m^2/s^3)
η	Torch efficiency (%)
Γ_φ	Diffusion coefficient
κ	Turbulent kinetic energy (m^2/s^2)
κ_A	Turbulent kinetic energy at adjacent element to the wall (m^2/s^2)
μ	Dynamic viscosity (kg/ms)
ν	Kinematic viscosity (m^2/s)
ϕ	Process variable
ρ	Density (kg/m^3)
τ	Shear stress (Pa)
τ_w	Wall shear stress (Pa)
ς	Liquid fraction

Dimensionless numbers

Pr	Prandtl number: $Pr = \nu / \alpha$
Re	Reynolds number: $Re = \rho u D / \mu$
Re_r	Relative Reynolds number: $Re_r = \rho D_p (\boldsymbol{u} - \boldsymbol{u}_p) / \mu$
U^*	Dimensionless mean velocity
y^*	Dimensionless distance from element to the wall
y_T^*	Dimensionless thermal sublayer thickness

Chapter One: Introduction

1.1 Background

Rare earth materials play a crucial role in today's technological advances in materials. The importance of rare earth materials can be seen in applications like permanent magnets [1] and luminescent materials used for television and lighting systems [2-4]. In electronic and semiconductor industries, rare earth oxides are commonly used dopants for property tuning [5] or matrix materials such as high-k dielectric gate material $(Nd_{1-x}Gd_x)_2O_3$ (NGO) [6]. Perovskite-type rare earth mixed oxides are well known for high temperature superconductors [7] and ferroelectric materials [8]. Rare earth oxides are also used in the glass industry, not only for glass components but also surface polishing [9]. In agriculture, rare earth materials can be employed to improve plant resistance and alleviate the effects of pollution by acid rain, ozone, pesticide, heavy metals etc [10]. In some applications of rare earth materials, certain objectives can be achieved by forming mixed oxides containing two different rare earth elements. Examples are Eu-doped Y_2O_3, where luminescent rare earth ions are incorporated into a nonluminescent host which is essential for energy-efficient fluorescent lighting [2], or Sm-doped CeO_2 oxygen ion conductors which are suitable for solid electrolytes [11].

Nanoparticles have attracted great interest due to their unique chemical and physical properties that are remarkably different from bulk materials. As such, they have great potential in the applications of electronics, chemical, and mechanical industries, such as superconductors, catalyst, drug carriers, sensors, magnetic materials, structural materials, and electronic materials [12]. Specifically, rare earth oxide nanoparticles have shown their superior properties in phosphors [13], magnets [14], and superconductors [15], and

also with the benefits for the miniaturization of electronic components [16]. As a consequence, the synthesis and study of nanomaterials has become an active field. Rare earth oxides are exceptionally thermodynamically stable because they have the most negative standard free energies of formation compared to any other oxides, while being chemically active [17]. Generally, the trivalent state is the most stable in aqueous solution and therefore, sesquioxides R_2O_3 exist for most rare earth ions at ambient conditions. Various techniques have been developed or tailored to synthesize rare earth oxide nanomaterials, including sol-gel, hydrothermal, and hydrolysis processing, laser ablation, flame spraying, vapor deposition, DC plasma, RF plasma, microwave plasma synthesis, and mechanical milling.

Inductively coupled radio frequency plasma (RF-ICP) has been widely used over the past two decades in a number of material processing applications involving in-flight melting and deposition of metals, ceramics, and composites, plasma reactive deposition and plasma synthesis of nanoparticles. The general schematic diagram of the RF-ICP spraying system is illustrated in **Fig. 1.1**. This process belongs to the family of thermal spraying. The heat source generated from the inductively coupled radio frequency has a temperature field of over 8000 K at atmospheric pressure, allowing the melting of any material. Compared with DC plasma and capacitive RF plasma spraying, the principal advantages of RF-ICP spraying are the relatively large volume, low velocity of the discharge coupled with the ease of access for axial injection of the materials into the plasma. This allows for the close control of the processing conditions at high throughputs. The absence of electrodes offers the added advantage of ease of operation with a wide range of inert, oxidizing or reducing gases at atmospheric and low pressure conditions. [18]

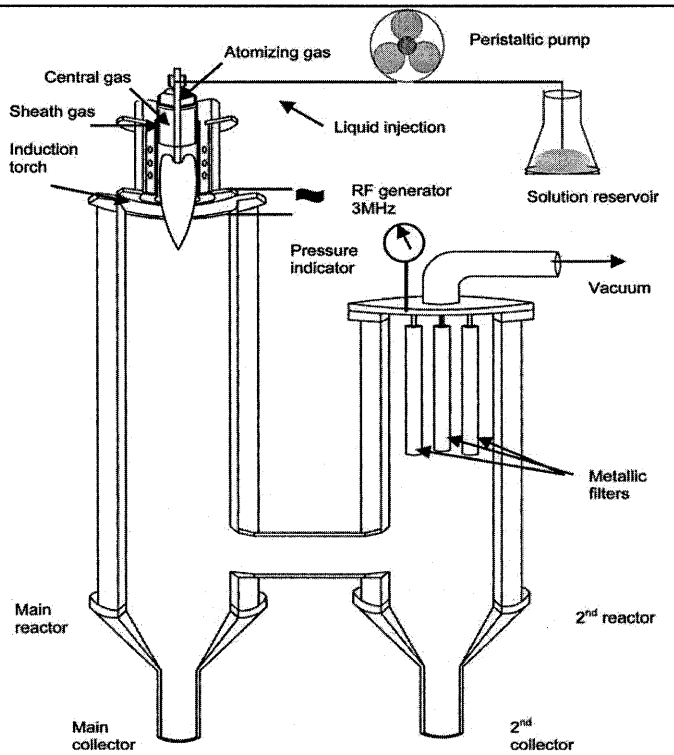

Fig. 1.1. Schematic representation of RF-ICP spraying system [19]

1.2 Motivation

Industrially available rare earth oxide micron-sized particles, prepared from chemical synthesis, usually have a wide size distribution from submicron to a few tens of microns, with irregular particle shapes. According to the current application requirements, non-agglomerated, mono-dispersed spherical nanoparticles of rare earth oxides with a narrow size distribution are the most preferable for high performance materials. Furthermore, for the purpose of industrialization, the synthesis process needs to be low cost and involve both continuous operation and a high production rate. A large number of techniques for the preparation of such nanoparticles has been developed, including chemical and physical methods. However, each of these methods has its limitations or disadvantages. For example, chemical methods usually have long reaction time and complex chemistry is needed. In addition, impurities are easily introduced into the system. On account of the very high thermodynamic stability of rare earth oxides, general

physical gas condensation methods like flame spraying is ineffective. Hence, RF-ICP spraying, which is capable of handling materials with high melting point and fulfilling low impurity requirement, has been playing an indispensable role in the synthesis of rare earth oxide nanoparticles.

The commonly used material feed method for RF-ICP spraying is powder feed. A powder feeder with screw conveyers and a carrier gas is used to inject the raw material particles into the centre of the plasma plume through an injector. In order for them to penetrate the plume and to have longer residence time in it, the particles should be injected with a momentum similar to that of the plasma jet. This is realized by adjusting the carrier gas flow rate. However, when the particle size decreases to below 5 μm, the carrier gas velocity has to be increased drastically to ensure that enough momentum is transferred to the particles. In addition, as rare earth oxides have high densities, they need even higher carrier gas flow rate to be transported. Consequently, this high carrier gas flow rate disturbs the stability of the plasma jet, thereby affecting the stability of the powder processing. As alternative feed methods, liquid feedstock including solution and suspension are being used more and more for the injection of fine particles. Rare earth salt solution feedstock has been employed in RF-ICP spraying for a long time. Various salts have been applied including nitrates, acetates, isopropoxides, and butoxides, etc. In solution spraying, the solution is vaporized and nanoparticles are formed through a nucleation and condensation process. Since the reactants are already in the ionic state, the large energy consumption for powder melting and vaporization can be saved. The sprayed nanoparticles have relatively small and uniform size. Nevertheless, the cost of rare earth organic salts is much higher than oxide powder materials, thus, it is hard to implement this method in industrial scale production. Although the price of rare earth inorganic salts is close to that of oxide powder materials, they can cause serious damage to the plasma

spraying system as the byproducts are corrosive inorganic acids.

Suspension plasma spraying (SPS), as another way for liquid feed, has been proved to be a very effective way for injecting small rare earth oxide particles [20]. The suspension with a certain concentration of reactant particles is pumped into the plasma plume through an atomization probe to form micron-sized droplets. The droplets are flash dried, and the remaining particles are melted, vaporized, and condensed into nanoparticles. However, the process parameters of SPS such as suspension concentration, solvent type, and plasma gases have not been systematically studied in relation to product properties. Typically, water is used as a solvent to disperse and carry the reactant particles. However, since the evaporation of water consumes a large portion of the plasma enthalpy (up to 20% [21]), the plasma will be quenched and the enthalpy left for particle melting and vaporization will be greatly reduced. This is one severe drawback that restricts the generalization of SPS in the plasma spraying industry.

Initially in the present research, powder feed spraying of rare earth oxides materials (Y_2O_3, Sm_2O_3, Dy_2O_3, Lu_2O_3) in Ar plasma was studied. A problem we encountered in powder feed spraying was clogging of the feed system arising from small particle size and high density of the rare earth oxide. As a consequence, the powder feed rate was inconsistent; thus the processing became discontinuous. To overcome the clogging, the SPS method was adopted. Afterwards, though material flowability was no longer a problem, the quenching effect caused by vaporization of the water solvent adversely affected the particle heat treatment so much that the results were even worse than powder feed spraying. Consequently, organic solvents ethanol and acetone were employed to substitute for water, owing to their much lower value of heat of evaporation. The results of organic solvent SPS were encouraging, but another problem surfaced. The organic

solvent decomposed into carbon at high temperatures and contaminated the final products. In order to completely combust the organic solvent, as well as to further enhance the heat treatment, oxygen was introduced into the SPS as secondary plasma gas for the first time. Oxygen introduction offered dual functions. In addition to aiding the combustion of organic solvents, oxygen also elevated the plasma enthalpy by improving the energy transfer efficiency.

In addition, since rare earth mixed oxide nanoparticles have shown promising functions in a wide range of areas, plasma spraying synthesis of rare earth mixed oxide nanoparticles would be an intriguing research topic. This technique can produce mixed oxide nanoparticles with high purity, which is crucial in some applications. In this research, a totally new trial of plasma synthesis of rare earth mixed oxide nanoparticles was investigated.

For the explanation of the effects of oxygen gas and solvent combustion on plasma thermophysical properties and as-sprayed particles, mathematical models of plasma fields are very helpful. Some of the in-situ plasma properties and in-flight particle behaviour can only be revealed by modeling. The modeling results can then be associated with experimental results to elucidate them.

1.3 Objectives

In the present research, various rare earth oxides R_2O_3 (R = Y, Sm, Dy, and Lu) were sprayed by RF-ICP to synthesize ultrafine particles. Rare earth elements with different ionic radii (large: Sm; medium: Dy; and small: Lu) and thermodynamic properties were chosen to study their different behaviour under plasma treatment. Y_2O_3 was added additionally because of its special position outside the lanthanide series. Y_2O_3 has a large

ionic radius but, unlike Sm, it is very stable in the cubic phase under ambient conditions. Thus it would be interesting to look into the plasma-induced phase transformation effect on Y_2O_3. Powder and suspension feedstock were adopted, both of which were sprayed with and without oxygen secondary plasma gas. For suspension spraying, various solvents (water, ethanol, and acetone) and suspension concentrations were studied. Three aspects of the sprayed particles were investigated and compared: particle morphology, productivity, and crystal structure. Furthermore, mathematical modeling of the plasma field was conducted by means of a commercial computational fluid dynamics (CFD) analysis program FLUENT V6.3.2©. The temperature and velocity distributions of the plasma fields as well as the particle temperatures and trajectories were simulated for Ar, Ar/O_2, and (Ar/O_2+acetone) plasma. Finally, modeling data was related to the characterization results of the as-sprayed particles to elucidate the plasma processing mechanism.

The main objectives of this research are as follows:

(i) To synthesize rare earth oxide nanoparticles with small size and narrow size distribution at high productivity.

(ii) To study the effects of using powder and suspension feedstock on particle morphology, productivity, and crystal structure.

(iii) To study the influence of various solvents (water, ethanol, and acetone) in suspension spraying.

(iv) To investigate the effects of oxygen gas introduction and combustion-aided SPS on particle morphology, productivity, and crystal structure

(v) To compare the behaviour of various rare earth oxides under plasma spraying.

(vi) To investigate the possibility of synthesizing rare earth mixed oxide nanoparticles by plasma spraying.

(vii) To simulate the plasma fields of Ar, Ar/O_2, and (Ar/O_2+acetone) by mathematical means, and study their thermophysical properties in association with the properties of as-sprayed particles.

1.4 Novelties

(1) RF-ICP spraying process for rare earth oxide nanoparticles synthesis has not been thoroughly investigated so far because of the high thermodynamic stability and poor flowability of the materials. In this research, a systematic study of powder and suspension feed plasma spraying with various solvents and plasma gases was conducted. The effects of processing conditions on different rare earth oxides of Y_2O_3, Sm_2O_3, Dy_2O_3, and Lu_2O_3 were studied in relation to particle morphology, productivity, and crystal structure.

(2) Combustion-aided SPS was developed and applied in spraying synthesis of nanoparticles for the first time in this research, in order to tackle the high thermodynamic stability and poor flowability of rare earth oxide materials. This technique takes advantages of both O_2 recombination and organic solvent combustion, improving the heat treatment and spraying results remarkably.

(3) A variety of modeling work has been done on powder feedstock and solution feedstock for plasma spraying, but modeling of the SPS process has not been done. This research carried out a computational simulation on the SPS process for the first time. In particular, oxygen recombination and solvent combustion effects were

incorporated in the plasma spraying model, which is a new step in plasma modeling. This will provide valuable experience for future researchers.

(4) Synthesis of rare earth mixed oxide nanoparticles by RF-ICP spraying and their crystallographic characterization is another novelty. The work made contributions to both industrial applications and crystallographic fundamentals.

Chapter Two: Literature Review

2.1 Rare earth oxide materials

2.1.1 Basics of rare earth oxides

The rare earth oxides have the greatest negative standard free energies of formation for any oxides, which accounts for their exceptional thermodynamic stability. The ionic size of the rare earth atom in combination with oxygen to form oxides contracts smoothly across the series. The solid-state chemistry of individual atoms in combination with oxygen is primarily dependent upon its electronic configuration and ionic size. In the rare earth series of elements, the increasing nuclear charge, as electrons are added to the 4f orbitals, is effectively shielded by the outer $5d^1$ and $6s^2$ valence electrons. This causes the valency to hold favorably in a trivalent state for the rare earth atom whose energy varies gradually across the series [22]. The rare earth sesquioxides R_2O_3 (R stands for rare earth element) are the stable well-defined solids usually obtained as the final product of the calcination in air of most rare earth metals and salts such as oxalates, carbonates and nitrates. Therefore, in this research, we will focus only on rare earth sesquioxides. However, some rare earth elements take a divalent or a tetravalent state, and in the case of Ce, Pr, and Tb, the intermediate phase also appears designated as R_nO_{2n-2m}. **Fig. 2.1** shows some basic physicochemical data of rare earth oxides.

OXIDES
Ln_mO_n

Ln	stable oxide	formula wt.	element %	color	structure type†	density gcm^{-3}	m.pt. °C
Y	Y_2O_3	225.8	78.7	white	C	5.0	2430
La	La_2O_3	325.8	85.3	white	A	6.6	2305
Ce	CeO_2	172.1	81.4	off-white	fluorite	7.3	≈2600
Pr	Pr_6O_{11}	1021.5	82.8	black	[fluorite]	6.9	≈2200
Nd	Nd_2O_3	336.5	85.7	pale blue	A	7.3	2320
Sm	Sm_2O_3	348.8	86.2	cream	B/C	7.1	2335
Eu	Eu_2O_3	351.9	86.4	white	B/C	7.3	2350
Gd	Gd_2O_3	362.5	86.8	white	B/C	7.6	2420
Tb	Tb_4O_7	747.7	85.0	dark-brown	[fluorite]	7.7	≈2410
Dy	Dy_2O_3	373.0	87.1	white	C	8.2	2408
Ho	Ho_2O_3	377.9	87.3	white	C	8.4	2415
Er	Er_2O_3	382.5	87.5	pink	C	8.6	2418
Tm	Tm_2O_3	385.9	87.6	pale green	C	8.9	2425
Yb	Yb_2O_3	394.1	87.8	white	C	9.2	2435
Lu	Lu_2O_3	397.9	87.9	white	C	9.4	2490

Fig. 2.1. Physicochemical properties of rare earth oxides [11]

An unusual characteristic of rare earth oxides is the ionic motion. Oxide ions migrate in the oxides even at relatively low temperatures and this feature strongly influences the variation of the oxygen content in the oxides. The fluorite-related rare earth oxides show very unusual diffusion characteristics. Up to the temperature of one-half of the melting point (called the Tammann temperature), atomic mobility in the oxide solid does not become significant. Around the Tammann temperature, the metal atoms in rare earth oxides just begin to migrate. In the rare earth oxides, the metal substructure is rigid up to the temperatures of 1200-1400°C, which is approximately half of the melting point. However, in the case for the counter anion of the oxide, the oxygen substructure becomes mobile far below the Tammann temperature and in some cases even at temperatures lower than 300°C. In spite of the high oxide mobility, the rare earth oxides are mostly thermodynamically stable compounds, with melting temperatures above 2300°C. Oxide anion transport rapidly decreases as the atomic number of the rare earth element in the oxide increases. For example, the mobility between lanthanum and erbium varies by a factor of 10^2. [23]

In the polymorphism, five distinct crystalline types have been identified for the rare earth sesquioxides (**Fig. 2.2**). The A-type (hexagonal) and B-type (monoclinic) structures are adopted by the lighter rare earth element whereas the C-type (cubic) is found for the heavier (smaller) rare earth element and similarly sized Yttrium. The H and X structures are found only at very high temperatures [24]. All the sesquioxides transform to high-temperature forms (two phases in some cases) above 2000°C. At, and near ambient temperatures, the conversion from A- (or B-) to C-type is so slow that the A and B forms are stable once prepared. The B (and A) to C conversion on cooling is unusual in that it is accompanied by a volume increase of around 10%. The A form of hexagonal sesquioxides is of space group $P32/m$ with one formula per unit cell. The metal atoms are in a seven coordination with four oxygen atoms closer than the other three. The four oxygen atoms are bonded to five metal atoms and the other three to four metal atoms. The A-type structure has been found from La_2O_3 to Nd_2O_3. The B form sesquioxide is a monoclinic distortion of the A form. The B-type sesquioxide has the space group $C2/m$ with six formula units per cell. The metal atoms in the B-type polymorph are seven and six coordinated. The C form structure is of the cubic bixbyite type, cubic space group, $Ia\bar{3}$, containing 32 metal atoms and 48 oxygen atoms per unit cell related to a doubled-edge fluorite structure with one-fourth of the oxygen sites vacant and regularly ordered. To consider the relationships between the RO_2 dioxide on one hand and the A, B and C form sesquioxides on the other is very beneficial. In the dioxide, the metal atoms are eight fold coordinated with cubic coordination polyhedra sharing all edges to form a three-dimensional network (**Fig. 2.3**). In the case where one-fourth of the oxygen atoms of this network are removed along nonintersecting strings in the four <111>. directions, this results in the situation where every atom is six fold coordinated, and the C type is

obtained. In this case, one-fourth of the atoms have oxygen atoms missing across the body-diagonal and three-fourths have oxygen atoms missing across the face-diagonal. On the other hand, if the oxygen substructure of the fluorite RO_2 is preserved completely and the metal atoms are moved into interstitial sites in such a manner that slabs of RO_2 two atom-layers wide are sustained, shearing occurs at these regular intervals and the A type with seven fold coordination is formed. The B form is very alike to the A type with six- and seven fold coordination [25]. Only in the middle range of ionic radius can all five polymorphic phases be formed by each oxide. With increasing temperature, the order of transition is C→B→A for these rare earth oxides. Besides this, high pressure decreases the transformation temperature of the sesquioxide, while a decrease of ionic radius of the rare earth component of the sesquioxide requires the transformation pressure to increase. C-type Eu_2O_3, for example, transforms to the B form at about 1100 °C and then to the A form at 2040°C. By further heating, the A form transforms to the H form at about 2140°C and then finally to the X form at about 2280 °C just below the melting point at 2340°C. For the lighter rare earth oxides from La_2O_3 to Nd_2O_3, the C form oxide might be metastable. As the A form transforms to H, an abrupt decrease in the *c*/*a* ratio is observed as does the density. Both *a* and *c* increase sharply but the lattice *a* increase is more rapid, and reduces the ratio *c*/*a*. The temperature region of stability of each polymorph except the C form becomes narrower as radius of the rare earth decreases. Finally lutetium (and scandium) directly makes a transition from C-type solid to the molten state.[26]

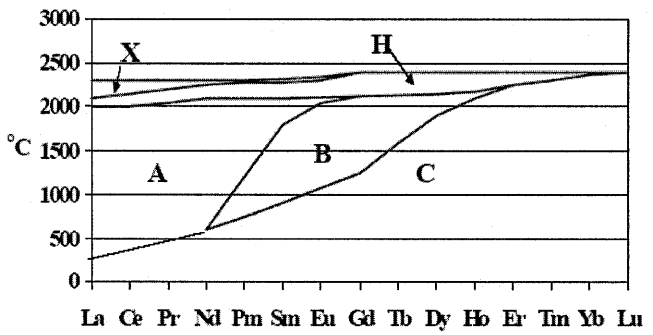

Fig. 2.2. Phase diagram of rare earth sesquioxides

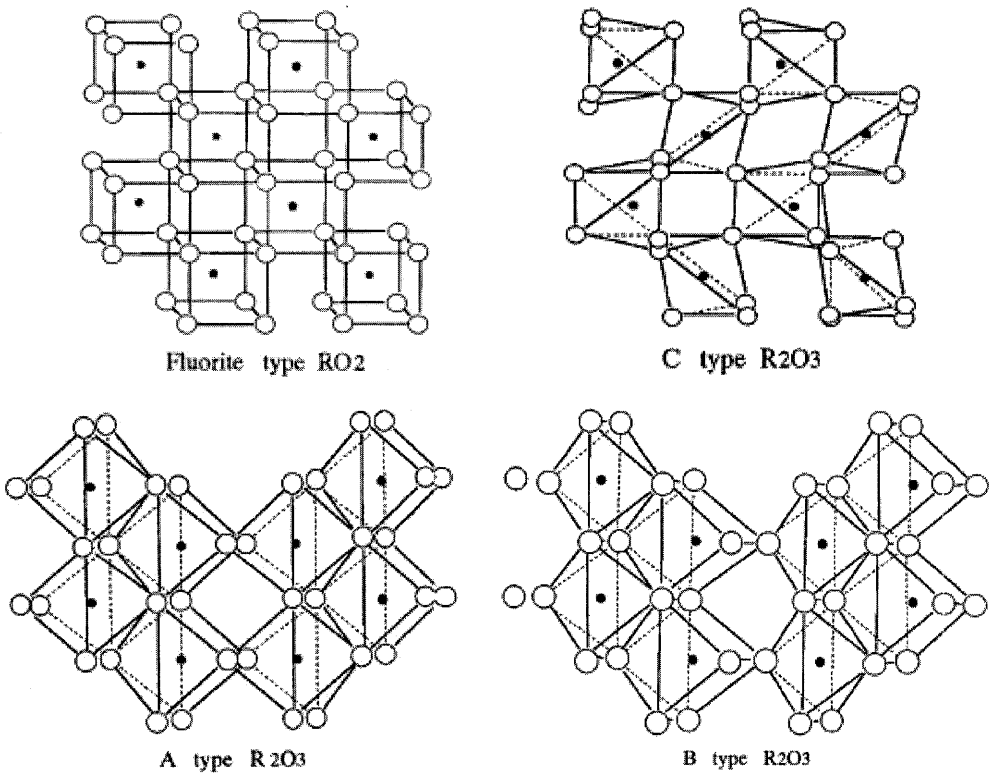

Fig. 2.3. Crystal structure of fluorite-type RO_2, C-type, A-type and B-type R_2O_3. The solid dots indicate the metal atoms

2.1.2 Synthesis of rare earth oxide nanoparticles

Rare earth oxides have unique properties that make them versatile functional materials in many fields, including phosphors [27], catalysts [28], and fuel cells [29]. Nanoparticles of rare earth oxides possess unusual physical and chemical properties in comparison with conventional bulk materials, owing to size-dependent surface effects, quantum-mechanical effects, and coulomb-charging effects. Therefore, they present an attractive potential for technological applications. Recent advances in the synthesis of rare earth oxides nanoparticles is attributed to the development of sophisticated preparation techniques. This contributes greatly to opening a door to the next stage of applications of rare earth oxides. The synthesis methods of nanoparticles can be classified as two categories: chemical methods, such as sol-gel [30], hydrothermal [31], hydrolysis

processing [32]; and physical methods, including laser ablation [33], flame spraying [34]and plasma spraying [35].

Chemical methods are commonly used for rare earth oxide nanoparticle production. The oxides are dissolved in aqueous acids to produce the corresponding salt, e.g. nitrates, chlorides. The reactivity with acid is noticeably slower for C-type structures, i.e. the heavy rare earth oxides, than for the A- and B-types, the light rare earth oxides. All the oxides will absorb water and/or carbon dioxide onto their surface forming a layer of hydrate, carbonate or hydroxy-carbonate [36]. The A and B- types do this more readily with lanthanum oxide, the most hygroscopic of the series. To avoid hydrolysis of the hydrated lanthanide ion the solutions should be kept acidic, pH<4. After separation by solvent extraction into individual pure rare earth containing solutions, a precursor, usually oxalate but possibly carbonate, is precipitated out, then calcined at around 1000°C to produce the desired oxide. Control of the precursor precipitation stage determines the particle morphology and also the size. As usually produced, the oxide particle sizes range from a micron or so to a few tens of microns in size. Finer particle material can be made by controlled nucleation, either in dilute solutions or by hydrolysis in situ of an additive, e.g. urea, that creates the precipitating anion [37]. The high surface area of the nanoparticles is quite useful in applications such as catalysis. Furthermore, a dopant can be deliberately introduced into the bulk phase at the precipitation step to form mixed oxides. The very similar ionic size means that a luminescent rare earth ion is easily incorporated, at the desired few percent, into a stable non-luminescent host, for example, to prepare the Eu-doped Y_2O_3 essential for energy-efficient fluorescent lighting [38]. This potential control over composition is also used to produce oxygen ion conductors, e.g. Sm-doped CeO_2, suitable for solid electrolytes.

The gas condensation process is a very important physical method to produce rare earth nanoparticles. In this process, a chamber is first pumped to ultrahigh vacuum under 10^{-5} Pa, and then it is filled with a few hundred Pa of a high-purity inert gas. The source material, usually in the form of a solid powder (mostly a metal), is vaporized by resistive heating in a boat or crucible made from a refractory metal (e.g. Mo, W or Ta). Analogous evaporation energy can be employed, such as high-power lasers, ion bombardment (sputtering), or electron beam. The metal vapor produced by evaporation collides with the inert gas atoms, and nanoparticles are formed by the condensation of vapor atoms. The characteristics of the particles depend on the inert gas pressure, the evaporation rate, and the gas composition. For example, decreasing either the gas pressure in the chamber or the rate of evaporation decreases the particle size. Metal oxide nanoparticles can be produced by mixing or replacing the inert gas with oxygen or by the subsequent oxidation of metal nanoparticles. Y_2O_3 nanoparticles were prepared by gas condensation and subsequent oxidation of Y metal particles, where the Y metal was evaporated from a tungsten crucible by direct current heating in a pressure of 659 Pa pure He gas [39]. It is notable that the crystalline structure is not cubic but hexagonal. The average particle size and BET (Brunauer, Emmett and Teller) specific surface area of the Y_2O_3 nanoparticles were 7 nm and 78 m^2/g, respectively. It has also been reported that Y_2O_3 nanoparticles as-prepared by gas phase synthesis have the monoclinic structure of the high pressure phase, which transforms into cubic Y_2O_3 above 873 K [40, 41]. It has been deduced from the dependence of the phase transformation temperature on the state of compaction that the stability of the high pressure phase is due to the nanostructured particle size.

Spray pyrolysis is another effective method to prepare homogenous and

non-agglomerated spherical particles [42]. A starting solution is prepared by dissolving the metal salt of the product in a solvent. The particles are generated by spraying the droplets atomized from the starting solution into an electronic furnace. The atomization process is carried out using a variety of atomizers (pressure, ultrasonic, vibration, disk rotation, electrostatic force, etc.) Heating the droplets in air converts them to oxide after evaporation of the solvent. Instead an electronic furnace, radio frequency (RF) inductively coupled plasma (ICP) is also used to generate high temperatures. This method is named spray-ICP technique and has been applied for a wide variety of oxides [43]. The average size and size distribution of the final particles depend on the size of the atomized droplet and the initial concentration of the starting solution as well as the concentration and velocity of the droplet generated by the atomizers. Because a high temperature RF-ICP is electrodeless, it can be operated in reactive gases, such as oxygen and halogen. Contamination of electrode materials can also be avoided by this technique.

2.2 Inductively coupled radio frequency plasma (RF-ICP) spraying

2.2.1 Fundamentals of plasma physics

Plasma is matter heated beyond its gaseous state, heated to a temperature so high that atoms are stripped of at least one electron in their outer shells, so that what remains are positive ions in a sea of free electrons. Not all the atoms in plasma have to be ionized. In cooler plasmas, there are still some species in the form of neutral atoms or molecules. An accurate definition of 'plasma' was given by Irving Langmuir in 1928 [44]: an approximately electrically neutral collection of ions and electrons which may or may not contain a background neutral gas, and which is capable of responding to electric and magnetic fields. The species in plasmas are usually in thermal equilibrium, meaning that they have a Maxwellian (Gaussian) velocity distribution as follows:

$$f(v) = Ae^{-(\frac{mv^2}{2KT})} \quad (2\text{-}1)$$

where A is a normalization factor, and K is the Boltzmann's constant. T is the temperature, which determines the width of the distribution. m and v are the mass and velocity of the species, respectively. In a plasma, the different species (ions, electrons, and neutrals) may have different temperatures: T_i, T_e, and T_n, because they may not collide often enough to equalize the temperatures, as the densities are usually much lower than for a gas at atmospheric pressure. However, each species usually collides with itself often enough to have a Maxwellian distribution. Examples of plasmas in everyday life and in nature include fluorescent lighting, lightning, auroras, solar coronas, comet tails, and black holes.

2.2.1.1 Debye length and quasineutrality

Plasmas are charged fluids which obey Maxwell's equations, but in a complex way. The electric and magnetic fields in the plasma control the particle orbits. At the same time, the motions of the charged particles can form charge bunches, which create electric fields or currents, which in turn create magnetic fields. Thus, the particle motions and the electromagnetic fields have to be solved in a self-consistent way. Consider a finite-temperature plasma consisting of a statistically large number of electrons and ions and assume that the ion and electron densities are initially equal and spatially uniform. Each species, denoted as σ, may be considered as a 'fluid' having a density n_σ, a temperature T_σ, a pressure $P_\sigma = n_\sigma K T_\sigma$, and a mean velocity u_σ. Assume that a charged test particle is inserted into an initially unperturbed, spatially uniform neutral plasma. Particles having the same polarity with the test particle will be slightly repelled whereas particles of opposite polarity will be slightly attracted. The slight displacements resulting from these repulsions and attractions will result in a small, but finite, potential in the

plasma. This potential will be the superposition of the test particle's own potential and the potential of the plasma particles that have moved slightly in response to the test particle. This slight displacement of plasma particles is called shielding or screening because the displacement tends to reduce the effectiveness of the test particle field. A cloud of particles with opposite polarity to the test particle will be surrounding it, and the cloud potential will partially cancel the test particle potential. The nominal radius of the shielding cloud is called the Debye length λ_D. Derived from Poisson's equation, Debye length λ_D is defined by

$$\lambda_D = \left(\frac{\varepsilon_0 K T_e}{n_e e^2}\right)^{\frac{1}{2}} \tag{2-2}$$

The condition $n_i \approx n_e$ is called quasineutrality and is a very important characteristic of a plasma. Charged particles will always find a way to move to shield out large potentials and maintain equal densities of the positive and negative species. In the main body of the plasma, the potential of the electrostatic field would vary over a distance L. If L is much larger than λ_D, the plasma is quasineutral. If L is the order of the λ_D, the quasineutrality conditions can be violated, and the screening region is called sheath. This is what happens near the walls around a plasma and near objects, such as probes inserted into the plasma. Inside the sheath, there is a Coulomb barrier, or potential drop, which repels electrons from and accelerates ions toward the sheath. [45]

2.2.1.2 Particle collisions in plasma

Now we consider what happens to the momentum and energy of the test particle in the plasma. This test particle will make a sequence of random collisions with the plasma particles; these collisions will alter both the momentum and the energy of the test particle. A collision is characterized by a deflection (or scattering) of the test particle by an angle θ

from its original direction of motion. The scattering angle θ depends on a number of parameters, including the test and target particle masses, the speed of the test particle relative to the target particle, and whether the collision is a bull's-eye collision or merely a grazing collision. The collision species could be like particles (e.g. electron-electron or ion-ion) or unlike particles (e.g. electron-ion, electron-atom, or ion-atom). The collision process will randomize the velocity distribution of the electrons until this distribution becomes Maxwellian (the maximum entropy distribution). One of the fundamental physical constants influencing plasma behaviour is the ion to electron mass ratio. The large value of the ratio often causes electrons and ions to experience qualitatively distinct dynamics. In high collision frequency cases, the electrons will transfer momentum to the ions, i.e. sharing their momentum with the ions, in which case the electrons will slow down and the ions will speed up until the average electron velocity and the average ion velocity become identical. Similarly, the electrons will share energy with the ions, in which case the ions will heat up while the electrons will cool. The collisional sharing of momentum and energy and thermalization of velocity distribution functions to make Maxwellians is the process by which thermodynamic equilibrium is achieved. Collision frequencies vary as $T^{-3/2}$ and so, for hot plasma, collisions are often slower than many other phenomena. Since collisions are the means by which thermodynamic equilibrium is achieved, plasmas are typically not in thermodynamic equilibrium, although some components of the plasma may be in a partial equilibrium (for example, the electrons may be in thermal equilibrium with each other but not with the ions).

If a plasma is weakly ionized then the collisions with neutrals must be considered. These collisions differ fundamentally from collisions between charged particles because now the interaction forces are short-range but not long-range Coulomb interactions. When a

particle hits a neutral it can simply scatter with no change in the internal energy of the neutral; this is called elastic scattering. It can also transfer energy to the structure of the neutral and so cause an internal change in the neutral; this is called inelastic scattering. Inelastic scattering includes ionization and excitation of atomic level transitions with accompanying optical radiation. Another process can occur when ions collide with neutrals. The incident ion can capture an electron from the neutral and become neutralized while simultaneously ionizing the original neutral. This process is called charge exchange. Because ions have approximately the same mass as neutrals, ions rapidly exchange energy with neutrals and tend to be in thermal equilibrium with the neutrals if the plasma is weakly ionized. As a consequence, ions are typically cold in weakly ionized plasmas, because the neutrals are in thermal equilibrium with the walls of the container. [46]

2.2.1.3 Simple transport phenomena

If an electric field E is applied to a plasma, electrons will move in the $-E$ direction and carry a current. In a weakly ionized gas, the electrons will come to a steady velocity as they lose energy in neutral collisions but regain it from the E-field between collisions. This average drift velocity u is of course proportional to E, and the constant of proportionality is called the mobility μ, which is related to the collision frequency:

$$u = -\mu E \tag{2-3}$$

The plasma density will usually be nonuniform, being high in the middle and tapering off toward the walls. Each species will diffuse toward the wall; more specifically, toward regions of lower density. The diffusion velocity is proportional to the density gradient ∇n, and the constant of proportionality is the diffusion coefficient D:

$$u = -D\nabla n / n \tag{2-4}$$

and similarly for the ions. The diffusion flux is then given by

$$\Gamma = -D\nabla n \quad (2\text{-}5)$$

Note that D has dimensions of an area, and Γ is in units of number per square meter per second. The sum of the fluxes toward the wall from mobility and diffusion is then

$$\Gamma_e = -n\mu_e E - D_e \nabla n \quad (2\text{-}6)$$

$$\Gamma_i = +n\mu_i E - D_i \nabla n \quad (2\text{-}7)$$

Since μ and D are larger for electrons than for ions, Γ_e will be larger than Γ_i, and there will soon be a large charge imbalance. To stay quasineutral, an electric field will naturally arise so as to speed up the diffusion of ions and retard the diffusion of electrons. This field, called the ambipolar field, exists in the body of the plasma where the collisions occur, not in the sheath. [45]

2.2.2 Development of RF-ICP spraying engineering

Thermal plasma systems always contain some mechanism for inducing the flow of electric current through an ionized working gas. The current flow heats the gas to very high temperatures through the mechanism of resistive, or Joule, heating. Through electronic, atomic, and molecular collisions the gas is maintained in an ionized state and the plasma becomes self-sustaining. Typical thermal plasma temperatures are in the range of 10,000 K to 30,000 K and result in heat transfer rates that are difficult to match by alternative processing techniques. In addition to heating, the current also interacts with the magnetic fields present to produce electromagnetic stirring, or Lorentz, forces which produce high velocity (100 to 10,000 m/s) flows in the plasma. In a DC plasma, a true current was drawn from the power supply in the form of ions or electrons to the electrodes to form an "electrical road" of the discharge. The physical processes in DC plasma are dominated by the axial DC electric fields. This situation is not greatly changed by the application of a low frequency AC voltage to the electrodes at the power supply

frequency of 50 or 60 Hz. The period of the applied frequency is so much longer than the time scale of most physical processes in the plasma that such discharges can be treated as though they were DC. However, when the applied frequency becomes high enough, the period of the oscillation will become comparable to the time that it takes electrons or ions, particularly ions, to traverse the sheath between the plasma and the electrodes. At such radio frequency, the power supply interacts with the plasma almost exclusively by displacement rather than real currents, the entirely different physical processes come into play. [44]

The general principle of inductively coupled radio frequency plasma is as follows. High frequency electric current passes through a solenoid coil where the resulting high-frequency magnetic field is induced along the axis of the discharge tube. In turn, the magnetic field induces a high-frequency vortex electric field concentric with the elements of the coil, which is able to provide breakdown and sustain the inductively coupled discharge. Electric currents in this discharge are also concentric with the coil elements and the discharge is apparently electrodeless. Generated in this way, inductively coupled plasma can be quite powerful and effectively sustained at atmospheric and even higher pressures. The magnetic field in the inductively coupled discharge is determined by the current in the solenoid; the electric field there, according to the Maxwell equations, is also proportional to frequency of the electromagnetic fields. As a result, to achieve electric fields sufficient to sustain the ICP, a radio frequency of about 0.1 to 100 MHz is usually required. The most common RF used in industrial plasma chemistry and plasma engineering is 13.6 MHz (corresponding wavelength is 22 m) [47]. The general eddy currents are limited to the external cylindrical shell of the plasma. The thickness of this shell, generally know as skin depth δ, is a function of the oscillator frequency f, the

average electrical conductivity of the plasma σ, and its magnetic permeability ξ_0:

$$\delta = (\pi \xi_0 \sigma f)^{-\frac{1}{2}} \quad (2\text{-}8)$$

Under typical low power operating conditions (i.e. f = 3 MHz, P < 100 kW), the skin depth is of the order of a few millimeters (3-5 mm). The corresponding discharge will have a diameter of the order of 20-30 mm [18].

RF-ICP spraying has been applied for many fields in materials processing. These include in-flight melting and deposition of metals, ceramics, composites, plasma reactive deposition and synthesis of ultrafine powders. The early researches on RF-ICP plasma were conducted by Reed [48] in 1961. After that, extensive research in this area has been done over the past 4 decades and renewed interest has now been manifested in both laboratory scale and industrial applications. The research on RF-ICP spraying can be categorized according to the forms of the feedstock: powder, solution, and suspension. Each feeding method has its advantages that suit different applications. Furthermore, various plasma gases, such as O_2, N_2, and H_2, are used to match the special requirements of the material reaction in the plasma as well as to elevate the plasma enthalpy.

2.2.2.1 Powder plasma spraying

With the growing demand for nanomaterials, RF-ICP has become an effective means for ultrafine powders synthesis of ceramics, metals and composites, due to its ability to tackle refractory materials and synthesize high purity nanoparticles. In 1989, Savkar and Siemers [49] prepared metal matrix composites of titanium aluminates reinforced with silicon carbide fibers using inductive plasma spray. Later on, Jiang et al. [50] and Jackson et al. [51] demonstrated the possibility of melting and processing larger refractory metal particles by plasma spraying, revealing the capability of this process. In Japan, Sugasawa

et al. [52-54] spent a few years on the RF-ICP synthesis of Y-Fe-O ultrafine particles. They used both powder and solution as starting materials of Y and Fe mixture with a certain ratio, and applied Ar/O_2 plasma with a controlled cooling process to achieve a higher quenching rate. In both methods, ultrafine particles which comprised an almost pure new phase Y-Fe-O compound were synthesized with a mean size of 20 nm. It was found that the feedrate of the stock had the primary influence on the particle shape and size distribution. The particle diameter was proportional to the concentration of the condensable species. A similar reactive plasma spraying done by Watanabe et al. [55] was to prepare electrically conductive nanoparticles of borides and nitrides by Ar/N_2 plasma spraying. The starting materials were powder mixtures of B and metals. When injected into Ar/N_2 plasma, the mixture evaporated immediately, and boride and nitride nanoparticles were formed through gas phase reactions between the mixture and the N_2 gas, followed by high rate quenching. The composition of the nanoparticles was correlated with Gibbs free energy of nitridation and boridation. The one that had lower Gibbs free energy predominated. Watanabe [56] also studied the synthesis of oxide nanoparticles by spraying metal powders in an Ar/O_2 plasma. This method has advantages such as effective evaporation enhancement of the metal powder resulting from exothermic reaction heat of the powder oxidation in the plasma. To control the particle size and yield, a tangential gas flow was injected to the plasma tail flame. TiO_2, Al_2O_3, and SiO_2 nanoparticles were synthesized in this way. A phase transformation phenomenon was present in TiO_2 and Al_2O_3 nanoparticles. With increasing O_2 quenching gas flow, the high temperature metastable phases increased in both cases. This dependency of phase composition was related to the nucleation rate, which is determined by the Gibbs free energy as well as the interfacial energy between liquid and solid. More importantly, the quenching gas flow had a strong influence on the particle size. The higher the gas flow,

the larger is the nanoparticle diameter. With the help of modeling, they argued that smaller surface tension or higher temperature at supersaturation leads to a higher homogeneous nucleation rate, resulting in the preparation of smaller nanoparticles.

2.2.2.2 Solution plasma spraying

Solution plasma spraying accounts for a large portion of the overall plasma spraying researches due to its low cost, smooth feed, and accurate stoichiometry. The early research on solution spraying was conducted by Suzuki et al. [57]. Various rare earth nitrate solutions were sprayed by Ar RF-ICP to form thin films with a thickness about 0.4 μm. The phases and orientation of the films were studied. Afterwards, they continued to study the solution spraying for ultrafine oxide particle synthesis [58]. Nitrates of various metals were used as precursors to spray in Ar plasma under the same conditions. The metal salts decomposed in the plasma and the metals recombined with oxygen to form nano-sized oxides. The morphology of the sprayed particles was different, including spherical, plate-like, cubical, and foil-like shapes. This was explained by the different thermodynamic properties of the metal oxides. Different effects of aqueous and organic solutions on the sprayed particles were investigated by Karthikeyan et al. [59]. The precursors were isopropoxide, butoxide, acetate and nitrate salts dissolved in organic solvents isopropanol or butanol, or dissolved in water. The results showed that aqueous solutions resulted in a larger particle size and wider distribution, whereas organic solutions produced finer particles with a narrower size distribution. The reason given was that organic and aqueous solvents have different thermodynamic properties, which resulted in different plasma enthalpy, particle nucleation and growth processes. In 2005, Ishigaki et al. [60] synthesized TaC nanopowders from tantalum ethoxide precursor in Ar/H_2 plasma. The addition of H_2 aimed to remove carbon by forming C_xH_y. The study

discussed the pressure effect on particle size and concluded that higher pressure induces larger particle size due to the higher residence time and lower cooling rate, while lower pressure causes a smaller size. Unlike previous research [56], the radial quenching Ar gas in this research had no significant influence on the particle size, which was attributed to the turbulent flow caused by the quenching gas. When the quenching gas was changed to He, which is lighter than Ar and thus cannot cause turbulence, the mean particle size decreased from 12 to 8 nm. In Canada, Castillo and Munz [19] synthesized rare earth doped CeO_2 fine powders by an Ar/O_2 RF-ICP for solid oxide fuel cell application. Nitrate precursors were chosen because the chlorides or hydroxides are highly toxic and corrosive, and organic salt is more expensive. The sprayed powders retained the elemental composition of the initial solution, and exhibited a high degree of purity and crystallinity. The particle size was in the range of 25-28 nm, independent of plasma operating parameters, dopant, and amount. However, with a similar method, Li et al. [61] did not succeed in producing Er-doped TiO_2. Er^{3+} was hardly dissolved in the TiO_2 lattice but mainly formed $Er_2Ti_2O_7$ and coexisted with TiO_2. The possible reason could be that their plasma power was only half as much as that of Canadian researchers' and the oscillator frequency was lower.

2.2.2.3 Suspension plasma spraying (SPS)

Powder feed has disadvantages such as the high cost of the metal raw materials, clogging, or inhomogeneous mixing and heating. Solution feed can produce acid by-products corrosive to the plasma system and introduce impurities. Therefore, suspension plasma spraying (SPS) was developed to solve these problems by Bouyer et al. in 1997 [62]. In this process, a suspension made by dispersing powder in a solvent is introduced into the center of an RF-ICP through a water-cooled gas-atomizing probe. As the formed droplets

are fed into the plasma, they are flash dried, melted, partially vaporized, and condensed into nanoparticles. The process was applied to spheroidize hydroxyapatite (HA) particles which had needle shapes initially. After spraying, the particles became spherical and had a narrow size distribution. However, the sprayed HA had partial decomposed as a result of overheating, and the by-products were lime and tricalcium phosphate. To minimize the HA decomposition, Ar/O_2 sheath gas was used instead of Ar/H_2, as the former has lower enthalpy than the latter. The presence of water in the spray also contributed to the stabilization of the HA structure. These results of SPS indicated a great potential of application in powder processing. The process is also suitable for in-flight reaction, which can take place if the suspension is constituted by a mixture of a few solid phases with a reactive liquid phase. After Bouyer, the research on SPS processing was mainly on HA materials for the synthesis of its ultrafine particles and composite [63-65]. Although much effort has been put on the optimization of the plasma parameters, such as plate power, chamber pressure, probe position, and gas flowrate, the decomposition of HA is still the main problem. More recently, French researchers applied SPS in SOFC to form $LaMnO_3$ thin films [66]. Instead of water, ethanol was employed as the liquid to make the suspension, with a small amount of dispersant to decrease the viscosity. It was found that Ar/H_2 and $Ar/H_2/He$ mixture plasma gas caused a complete decomposition of the $LaMnO_3$, while pure Ar plasma induced only partial decomposition, indicating the necessity of lower temperature. The chemical composition was also modified to reduce decomposition. MnO_2 was doped in $LaMnO_3$ before spraying to suppress the decomposition. Finally, a minimal perovskite decomposition, less than 5 wt% was realized by spraying 20 mol% MnO_2 doped $LaMnO_3$ in Ar plasma.

2.3 Simulation and modeling of RF-ICP spraying

2.3.1 Progress in RF-ICP spraying modeling

Mathematical models of the plasma spraying process have existed for more than twenty years and are now in an advanced stage of development. A complete mathematical model of the process would allow the rapid estimation of the effects of the operating parameters and the prediction of the trajectory and the temperature history of the sprayed particles, thus allowing optimization of the system. The thermal, or collision dominated, plasma exists at temperatures and pressures where the continuum assumption is valid and where the plasma can be modelled as a variable property fluid. Consequently, computer modeling of thermal plasma systems involves the solution of the Navier-Stokes equation, the continuity equation, one or more energy equations, and Maxwell's Equations. From the modeling point of view plasma processing systems are highly non-linear. All physical properties are strongly temperature dependent and the governing equations are fully and interactively coupled.

2.3.1.1 Modeling of plasma plume

The first task in modeling the plasma spraying process is the calculation of the flow and temperature fields of the plasma gas. A full description of the plasma plume was done by El-Kaddah in 1984 [67]. The governing partial differential equations were the Navier-Stokes equations coupled with the energy and the Maxwell's equations. The principal assumptions of the model were as follows: the plume has azimuthal symmetry and the governing equations are two-dimensional when expressed in terms of cylindrical polar coordinates; the plume is time-independent; the plume is in a state of local thermodynamic equilibrium. The model used a control volume finite difference technique

[68] to solve the continuity equation, the turbulent Navier-Stokes equation, and a single plasma enthalpy equation. In addition, a diffusion equation was solved to represent the mixing of the plasma with the surrounding air. Turbulence was modelled using the k- two equation model with the standard set of constants [69]. The plume model has been validated by comparing its predictions against a wide range of experimental data [70, 71]. In all test cases, the model gave accurate predictions of the velocity and temperature of the plume at the torch nozzle exit. A laminar version of the model gave very accurate predictions of the temperature in a laminar plasma plume. In general, the predictions of the model for turbulent plasma plumes were in acceptable overall agreement with experiments. However, it should be noted that the experimental measurements for turbulent plasma plumes exhibit a considerable degree of scatter and it was difficult to draw concise conclusions about the validity of the model as applied to these systems. While the predicted decay rates of the velocity and temperature along the axes of the plumes were consistent with the experimental measurements, the model did have a tendency to over-predict the length of the potential core at the start of the jet. It was, however, consistently found that the standard turbulence model constants gave more accurate predictions for turbulent plasma plumes than predictions made using the isothermal jet correction. Same in 1984, Mostaghimi et al. [72] reported their solution of RF-ICP governing equations with the appropriate boundary conditions taking into account the strongly nonlinear plasma properties. Their modeling results also matched the experimental results quite well. Later on in 1989, Mostaghimi et al. calculated the electromagnetic fields in an RF-ICP torch based on the electromagnetic vector potential representation [73]. The model offers an effective means of accounting for variations in the coil geometry on the flow and temperature fields in the discharge and for achieving a better representation of the electromagnetic fields under higher frequency conditions (*f*

>10 MHz). These modeling works illustrated the importance of numerical modeling techniques in the analysis of RF-ICP systems, and provided the theoretical framework for the succeeding in-depth analysis of powder processing in such systems.

Because of the significant influence of the turbulence on the heat and mass transport phenomena in the RF discharge and the difficulty of obtaining detailed turbulence measurements in the high temperature discharge region, emphasis was placed on the use of mathematical modeling as a means of studying the turbulence behaviour in the RF-ICP torch. A number of models were proposed for computation of the plasma flow and temperature field with turbulent flow conditions. The k-ε fluid model was adopted by El-Hage et al. [74] in 1989 to determine the turbulent viscosity in a two-dimensional representation of RF-ICP. They pointed out that there are two regions in a RF plasma, i.e., the laminar region and the turbulent region. The central high temperature region is dominated by the laminar flow, whereas the near wall and upstream regions are dominated by turbulent flow. They also found that the swirl in the plasma gas increased the overall turbulence level in the torch. Later in 1994, Chen et al. [75] combined the standard k-ε turbulent model and the 2D formulation of the electromagnetic field through the concept of vector potential. This formulation took into account the coil-plasma interaction and coil geometry, and gave more realistic results of the electromagnetic field and fluid dynamics aspect of the turbulent flow. To elucidate the basic of turbulence phenomena, in 1999, Rubin Ye et al. [76] carried out a mathematical modeling of the flow and temperature fields in RF-ICP. Temperature and density fluctuation were included in the k-ε turbulence model to investigate their effect on the plasma turbulence and energy transfer. Their results showed that the density and temperature fluctuations have negligible effect on the turbulence and temperature field. The plasma turbulence, either its

intensity or its viscosity, is considerably larger in the near wall and upstream regions of the torch, for example, the relative turbulent viscosity can reach as much as 20 or more. The turbulence effect is negligible in the region with the plasma temperature over 5000 K. It was also found that the turbulence becomes significant when the gas flow rate is increased. By reducing the operation pressure, the turbulent field will move to the downstream of the torch. Moreover, the plasma turbulence can be reduced by increasing the dissipation power.

2.3.1.2 Modeling of gas mixture plasma

All of the modeling works mentioned above assumed pure argon as the working fluid. However, for particular applications, e.g. chemical synthesis spraying, it is often necessary or advantageous to add a molecular gas such as hydrogen, oxygen, or nitrogen, or to operate with a pure molecular gas or with air. The strong effects of adding molecular gases on the character of the plasma can be visually observed and are obvious also from the greater required power inputs, due to the molecular dissociation energies. The first comprehensive study on mixture gas plasma was reported by Girshick et al. [77] in 1990. They used the two-dimensional electromagnetic field model for atmospheric-pressure RF-ICP consisting of mixtures of argon with a diatomic gas, either hydrogen, nitrogen, or oxygen. The governing equations and boundary conditions were discretized and solved using the SIMPLER algorithm. In each case the relative volumetric flow rates of diatomic gas and argon were maintained at 1:4. The results for the different mixtures and for pure argon were compared, and the numerical results were compared to observations of the laboratory plasmas. Even at only 20% mole fraction the addition of molecular gases has a large effect on the plasma thermophysical properties and shapes. The calculated isotherms and streamlines for each mixture are shown in **Fig.2.4.** The calculations and the

experimental observations were in good agreement. The different behavior of the four plasmas was attributed to the different gas properties. Modeling of N_2 and Ar/N_2 plasma was also studied by Paul et al. [78] in 2000. A two-dimensional, optically thin and local thermodynamic equilibrium axisymmetric RF ICP model at various pressures from 100 to 760 Torr was solved numerically to study the pressure effect on the plasma. The modeling results showed that with the rise of the pressure, the electromagnetic forces decreased, plasma temperature on the axis of symmetry dropped, and the plasma shrank radically.

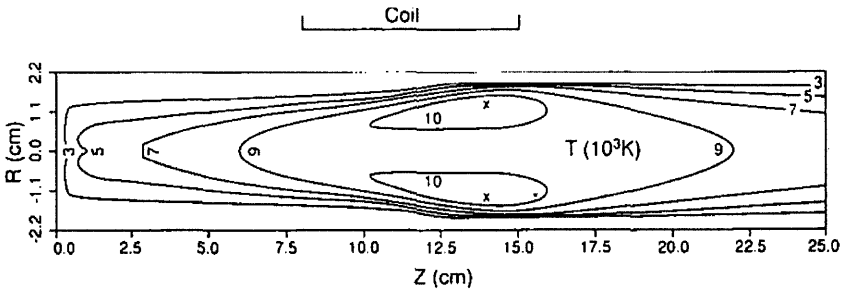

(a) Calculated isotherms, pure argon case.

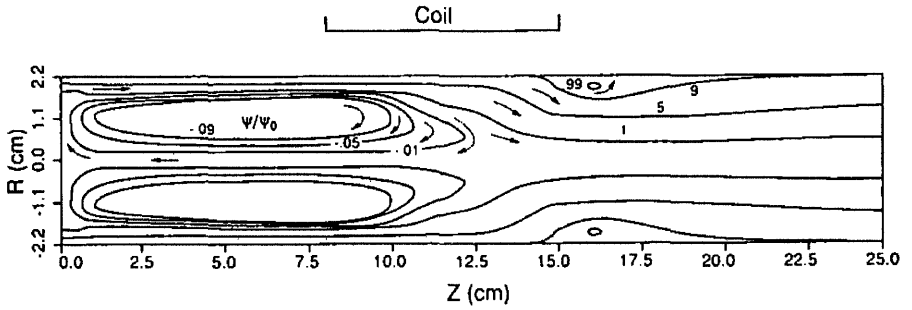

(b) Calculated streamlines, pure argon case.

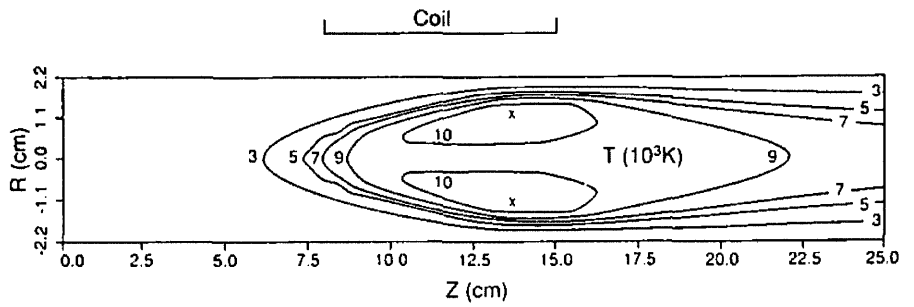

(c) Calculated isotherms, argon-oxygen case.

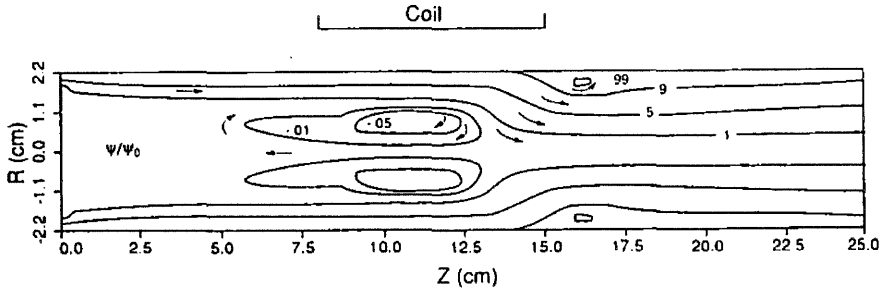

(d) Calculated streamlines, argon-oxygen case.

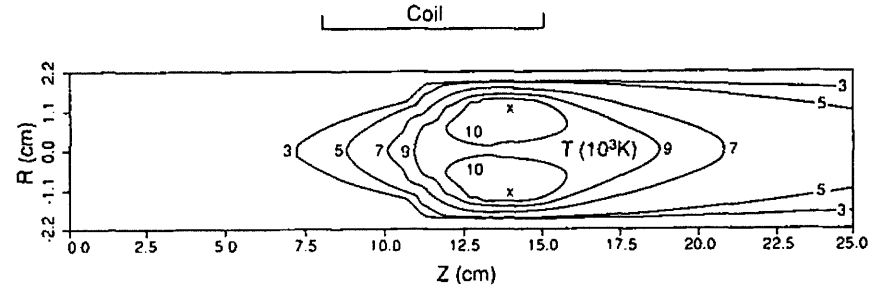

(e) Calculated isotherms, argon-nitrogen case.

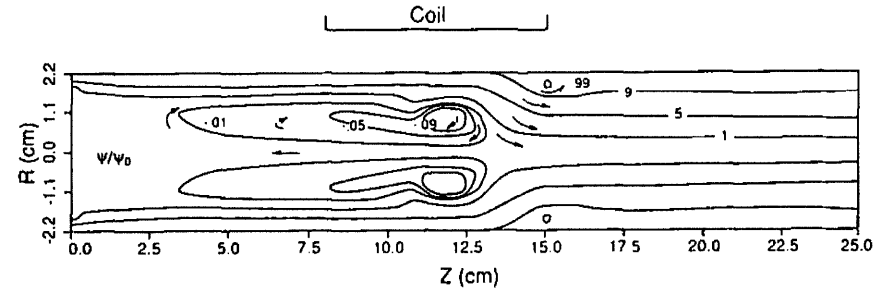

(f) Calculated streamlines, argon-nitrogen case.

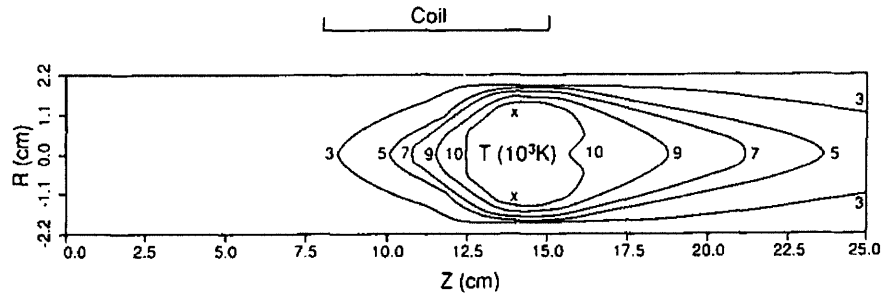

(g) Calculated isotherms, argon-hydrogen case.

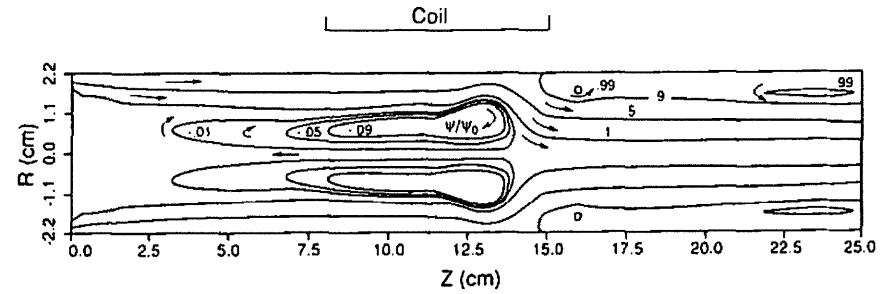

(h) Calculated streamlines, argon-hydrogen case.

Fig. 2.4. Modeling results of mixed-gas plasma

Most of the research on mixture plasma has been focused on O_2 or Ar/O_2 plasma as they have been widely used for many applications. Using a simplified two-dimensional spatially varying Ar/O_2 mixture discharge model, Takechi et al. [79] found that a mixture plasma ($Ar:O_2$ =1:1) increased the plasma density by enhancing the O-atom concentration. It was discovered that argon metastables Ar* played an important role in facilitating the dissociation of O_2. The mixture plasma density increased as the Ar fraction increased. Nevertheless, oversimplified estimation, such as use of equilibrium properties and use of the first-order approximation of Chapman-Enskog method, would cause errors in the numerical results. In 2006, Atsuchi et al. [80] performed more sophisticated computations for Ar/O_2 plasma under atmospheric pressure to investigate chemically non-equilibrium effect for dissociation and ionization. Higher-order approximation of the Chapman-Enskog method was employed for the estimation of transport properties. They reported that Ar/O_2 induction plasmas can be partially treated as equilibrium, but the diffusion effect cannot be negligible near the torch wall. A chemical non-equilibrium state appears near the torch wall region due to both dissociation and ionization. A steep temperature gradient causes moderate concentration gradient and a large number of oxygen atoms exist near the torch wall. Whereafter, they extended this research to argon and other diatomic gases such as hydrogen, with the exact same methodology [81]. It was revealed that the degree of thermal non-equilibrium is decreased in an Ar/H_2 plasma. This is mainly due to the larger collision frequency between electrons and hydrogen heavy particles, and the small mass of hydrogen resulting in the high energy exchange ratio. Also in 2006, Lee et al. [82] reported their simulation of Ar/O_2 plasma by means of a one-dimensional particle-in-cell/Monte Carlo-collision and two-dimensional fluid model. The results showed that as the pressure increases, the density of O^- and O_2^+ in the plasma

decreases due to mutual recombination. As the Ar/O_2 ratio increases, the plasma density increases and the dominant collision affecting the ion energy distribution function of O_2^+ changes from charge exchange to momentum transfer. Their simulation results agreed well with experimental data. In the meantime, Hsu et al. [83] carried out a systematic and detailed 2D modeling of Ar, Ar/O_2 and $Ar/O_2/Cl_2$ RF-ICP and compared the predictions with experimental data. The equations solved in their model were as follows.

(i) The neutral equations include overall mass continuity, that solves for pressure p, or interchangeably mass density ρ, momentum balance, that solves for radial and axial mass-averaged velocity, respectively, energy balance, that solves for neutral temperature T and mass continuity for species j, that solves for the species mass fractions w_j.

(ii) Maxwell's equations that reduce to the Holmholtz wave equation due to azimuthal symmetry.

(iii) Plasma equations include continuity equations for positive and negative ions, that solve for positive and negative ion density, respectively, as well as the electron energy equation, that solves for electron temperature.

The model equations were solved using commercially available packages (FEMLAB™ and MATLAB™), in part to demonstrate that these packages are sufficiently mature and flexible to be applied to the relatively complex set of equations that model chemically reactive plasmas. With strong diagnostic tools, the spatially-resolved electron density, electron temperature, total ion flux and ion composition at the wall, and radical densities at the wall were measured. Compared with the measurement, the non-Maxwellian electron energy probability (EEPF) modeling underestimated T_e and overestimated n_e of the pure Ar plasma. In O_2-rich conditions, the EEPFs are more Maxwellian and more accurate model predictions are obtained. In pure O_2 plasmas, the EEPF appears to be nearly Maxwellian and the model n_e predictions agree quantitatively with experimental

measurements as a function of power and pressure. Model predictions of total ion wall flux and ion composition are in good agreement with measurements for Ar/O_2 mixtures. Charge exchange reactions become increasingly important as pressure increases under the conditions investigated. However, model predictions for mixtures of Ar, O_2, and Cl_2 are in partial agreement with measurements, which was attributed to the inaccurate database for plasma with mixtures of Ar, O_2 and Cl_2.

2.3.1.3 Modeling of particles in plasma

To represent the trajectory and thermal history of the particles being processed in the plasma, a particle model is necessary. The basic assumptions of the particle model are as follows: the particles are spherical and their temperature distributions possess spherical symmetry; the particle trajectories are not affected by the turbulent fluctuations in the plasma plume; the particles do not interact with each other. Mckelliget et al. [84] proposed a particle model that was part of an integrated plasma spraying model. The motion of individual particles within the plasma was governed by the Basset-Boussinesq-Oseen equation in the absence of history effects. One-dimensional heat conduction and phase change was calculated within the particle. Convective and radiative heat transfer between the particle and the plasma was included. The initial particle velocities at the exit of the injector and the particle diameters were assumed to have Gaussian distributions. The mean velocity was obtained by dividing the volume flow rate of injector gas by the cross-sectional area of the injector outlet. The mean particles diameter and standard deviation were taken from the powder manufacturer's specification. All particles were assumed to originate from the center of the injector exit and to be travelling along the injector axis. A total of 500 particle trajectories were calculated. The predications of the particle model were compared with previous measurements for glass

spheres injected into a turbulent room temperature jet of air. The agreement between theory and experiment was very good, especially at the downstream locations. The calculated particle spray cone clearly demonstrated the presence of zones exhibiting different degrees of particle melting.

A complete model of particle formation in plasma should also include the particle nucleation and growth. The nucleation process is both a crucial and a poorly understood aspect of this problem. In 1994, based on homogeneous nucleation theory, Grishick [85] employed two different approaches to model the nucleation and growth process and compared the results.

(i) 'Discrete' models, in which separate rate equations are written for the populations of monomers, dimers, trimers and so on, up to some specified size, with larger sizes treated either in terms of a continuous distribution or by grouping sizes into sections, these sections typically being spaced logarithmically by particle volume.

(ii) 'Moment-type' models, in which an analytical expression for the nucleation rate serves as a source term to equations that describe evolution of the stable aerosol in terms of the first few moments of the size distribution.

Discrete models are more rigorous than moment-type models. Unlike moment-type models, they can treat coagulation among subcritical clusters, and they require no a priori assumptions concerning the form of the size distribution. They are capable of simulating evolution of the entire size distribution, including subcritical clusters, thereby resolving the behavior of the size distribution during the nucleation burst. By applying the discrete representation in on-dimensional plasma spraying model, a typical solution for time evolution of the silicon particle size distribution was obtained. It was demonstrated that the higher the cooling rate, the smaller the particle that is produced. The major advantage

of moment-type models is computational economy. Thermal plasma reactors have steep temperature gradients. As nucleation rates are extraordinarily sensitive to the vapor saturation ratio, acceptable accuracy in modeling nucleation by either approach requires extremely small time steps (equivalently, an extremely fine numerical grid). Discrete models require solution of a large set of coupled equations at each point, as a result of which their use is presently restricted to one-dimensional simulations. In contrast, moment-type models require solution of only a few equations at each point, and thus can realistically be coupled to a two-dimensional plasma reactor model. Although moment type models calculate only the first few moments of the size distribution (for example, the number of particles, a measure of their mean diameter, and the width of the size distribution), this information is adequate for most purposes. A moment-type model for heating and evaporation of the feed ion powder, together with iron vapor diffusion, was coupled into a set of two-dimensional flow equations. The results clearly reproduced the experimental trends and the right magnitudes of particle size, although the measurement data obtained at specific radial locations indicated that there was more cross stream mixing than predicted by the model.

2.3.1.4 Modeling of interaction between plasma and particles

As well as modeling the plasma itself it is also necessary to account for its interaction with the system being processed, which may take the form of powder or gas phases dispersed within the plasma or as a workpiece upon which the plasma impinges. The transfer of momentum and heat from the plasma to the particles is a very complex and important issue. There have been many studies that assume negligible effect of the particles on the plasma fields. This assumption implies that the presence of the particles does not alter the plasma fields and offers a means of decoupling the plasma and the

particle conservation equations. Although this significantly simplifies the computational task, the results obtained are of limited value since in most realistic cases, the loading is sufficiently high for the particles to act as a local heat sink and reduce the local plasma temperatures and, to a lesser degree, the local plasma velocities. The decrease in the plasma temperature, in turn, results in a reduction of the heat transfer rate to the particles. It has been shown by Proulx et al. [86] in 1985 that even for low overall particle loading the plasma-particle coupling effects can be important. For example, for copper particles injected into an argon inductive plasma with a loading rate (total mass flow rate of the particles to that of the plasma gas) of 0.3, the energy transferred to the particles, taking into account the plasma-particle interaction effects, is 50% smaller than if such an interaction were not taken into account. Obviously in this case the coupling between the plasma and the particle transfer equations is significant and should not be neglected. In 1987, to further investigate the plasma-particle interaction effects, Proulx and his co-workers [87] adapted the PSI-Cell concept developed earlier by Crowe et al. [88] to the RF ICP torch system and built a mathematical model. In this model, the momentum, mass, and energy exchange rates per unit volume between the gas phase and the particles are introduced as source/sink terms in the corresponding conservation equations for the gas and particle phases. An iterative technique involving the solution of the gas-phase conservation equations and the solution of the particle trajectories is used until convergence. In a way, the PSI-Cell model offers a means of coupling the Lagrangian system of equations used to describe the particulate phase to the Eulerian system of equations for the continuous phase. Their modeling work revealed that the plasma was significantly cooled by the densely-loaded particles, which in turn, gave rise to a corresponding drop of the efficiency of the melting of the particles in the plasma. The effect was found to depend strongly on the thermodynamic properties of the materials of

the powder. Later in 1990, McKelliget [89] carried out another simulation of RF-ICP torch to study the plasma field and the interaction between plasma and injected particles with similar theoretical principles and equations. They employed different solution methods to solve the equations, including control volume finite difference procedure, mutual inductance, and fifth order Runge-Kutta technique. At last, the calculated and the experimental results match quite well, and they drew the same conclusion as Proulx that the high particle loading rates caused a severe reduction in the extent of particle melting. The extreme nature of this effect can be traced to the mode of injection of the particles, which results in high particle concentrations in a highly localized region of the plasma. They also proposed that the use of smaller radius particles is likely to enhance particle melting at the cost of partially deposition on the walls of the torch.

In 1994, McFeaters et al. [90] developed a model that concurrently considers the chemical kinetics and particle growth mechanisms for the simulation of the synthesis of TiC particles by a thermal plasma process. This model uses a one-dimensional representation and thus it follows only one representative streamline within the reactor. However, a thermal plasma reactor for the reactive synthesis of ultra-fine powders exhibits important radial nonuniformities. To deal with this disadvantage, Desilets et al. [91] advanced the reactive synthesis modeling by using a two-dimensional, comprehensive model. The overall model consists of two parts for different domains (**Fig.2.5**). The first part was based on their previous work [92], concerning the generation of the atmospheric pressure high frequency plasma that used here for the synthesis of the ultra-fine particles. Essentially it presents the fluid dynamics of the plasma flow in the presence of the electromagnetic field. The second part deals with the complete model and special attention is given to species-conservation equations. The multi-component diffusion and

reaction aspects of these equations were then developed. The reactor model was completed by the addition of particle-nucleation and particle-growth equations. The model was then applied to the synthesis of ultra-fine silicon particles through the thermal decomposition of $SiCl_4$, to study plasma power and radial quenching effects. The simulation with the highest power shows the greatest temperature gradients, which are favourable to the homogeneous nucleation of silicon particles. The radial quenching is responsible for the more uniform particle size distribution.

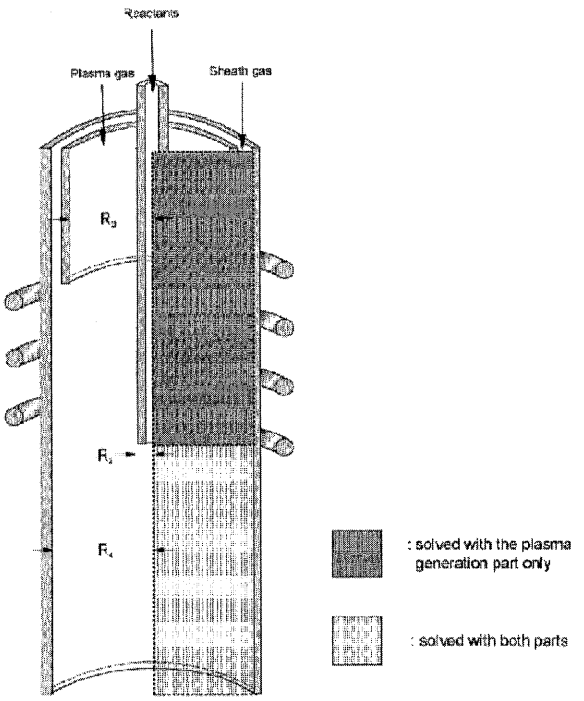

Fig. 2.5. The calculational domain for the two-part model

More recently, with the development of in-flight particle characterization techniques such as laser Doppler anemometry (LDA), phase Doppler anemometer (PDA), and two-color pyrometric method, the influence of process parameters on the particles has been extensively studied in plasma spray modeling. In 2004, Watanabe et al. [56] studied the effects of tangential quenching gas flow on the diameter and yield of oxide nanoparticles using numerical analysis. The tangential gas was injected to the plasma tail flame to control the diameter and the yield of the oxide nanoparticles. Homogeneous nucleation

and particle growth of oxide vapor were considered for the nanoparticle formation, with several assumptions to simplify the modeling. A two-dimensional numerical analysis of the plasma temperature, velocity, and concentration distribution in the torch was conducted with the SIMPLER algorithm. It was revealed that the quenching gas prevents the oxide vapor from diffusion to the wall. Increasing the flow rate of the quenching gas leads to the preparation of nanoparticles with larger diameter. In addition, smaller surface tension or higher temperature at supersaturation leads to a higher homogeneous nucleation rate, resulting in the preparation of smaller diameter nanoparticles. In the same year, Shigeta et al. [93] also investigated the quenching gas effects on the particle size in RF-ICP with the help of a two-dimensional axisymmetric plasma model incorporated with a one-dimensional particle model, and came to the same conclusion as Watanabe. Moreover, the model showed that an increasing powder feedrate leads to the increase of particle size due to the existence of more vapour to condense. Both of the above works were primarily conducted in 2D configurations. However, the plasma plume cannot be accurately modeled with an axisymmetric assumption. In view of this, again in 2004, a three-dimensional transient model was developed by Xiong et al. [94] to investigate the plasma jet perturbation by carrier gas and particle loading, and their effects on the in-flight particle behavior. The plasma jet and the particle trajectory were described in the three-dimensional geometry, and the non-thermal equilibrium of the particle in-flight was considered by employing a one-dimensional thermal model. This model was incorporated into the LAVA code, and the modified computational code LAVA-P-3D was tested by experiment and further applied to thermal spray process. Results showed that the carrier gas and multi-particles injection perturbed the plasma jet due to the impact of side jet, as well as the cooling and slowing effects. It was found that the particle spray trajectories were greatly influenced by the carrier gas flow rate, while particle temperature and

velocity is not sensitive to it.

2.3.2 Computational fluid dynamics (CFD) and finite volume method

Computational Fluid Dynamics or CFD is a very powerful tool for plasma modeling. It is strong at analysis of systems involving fluid flow, heat transfer and associated phenomena such as chemical reactions by means of computer-based simulation. This technique spans a wide range of industrial and non-industrial application areas, such as aerospace, automobile, and biomedical engineering. CFD codes are structured around the numerical algorithms that can tackle fluid flow problems. In order to provide easy access to their solving power, all commercial CFD packages include sophisticated user interfaces to input problem parameters and to examine the results. Hence all codes contain three main elements: a pre-processor, a solver, and a post-processor.

(i) Pre-processor. Pre-processing consists of the input of a flow problem to a CFD program by means of an operator-friendly interface and the subsequent transformation of this input into a form suitable for use by the solver. The user activities at the pre-processing stage involve:

- Definition of the geometry of the region of interest: the computational domain.
- Grid generation—the sub-division of the domain into a number of smaller, non-overlapping sub-domains: a grid (or mesh) of cells (or control volumes or elements).
- Selection of the physical and chemical phenomena that need to be modelled.
- Definition of fluid properties.
- Specification of appropriate boundary conditions at cells which coincide with or touch the domain boundary.

The solution to a flow problem (velocity, pressure, temperature etc.) is defined at nodes inside each cell. The accuracy of a CFD solution is governed by the number of cells in the grid. In general, the larger the number of cells, the better is the solution accuracy. Both the accuracy of a solution and its cost in terms of necessary computer hardware and calculation time are dependent on the fineness of the grid. Optimal meshes are often non-uniform: finer in areas where large variations occur from point to point and coarser in regions with relatively little change.

(ii) Solver. There are three distinct streams of numerical solution techniques: finite difference, finite element and spectral methods. The main differences between the three streams are associated with the way in which the flow variables are approximated and with the discretization processes. As the basis of the solver, all these methods perform the following steps:

- Approximation of the unknown flow variables by means of simple functions.
- Discretization by substitution of the approximations into the governing flow equations and subsequent mathematical manipulations.
- Solution of the algebraic equations.

The finite volume method was originally developed as a special finite difference formulation. The main commercially available CFD codes are: FLUENT, PHOENICS, FLOW3D, and STAR-CD. The numerical algorithm consists of the following steps:

- Formal integration of the governing equations of fluid flow over all the control volumes of the solution domain.
- Discretization involves the substitution of a variety of finite-difference-type approximations for the terms in the integrated equation representing flow processes

such as convection, diffusion and sources. This converts the integral equations into a system of algebraic equations.

- Solution of the algebraic equations by an iterative method.

The first step, the control volume integration, distinguishes the finite volume method from all other CFD techniques. The resulting statements express the conservation of relevant properties for each finite size cell. This clear relationship between the numerical algorithm and the underlying physical conservation principle forms one of the main attractions of the finite volume method and makes its concepts much simpler to understand by engineers than other methods.

(iii) Post-processor. For post-processing, the leading CFD packages are equipped with versatile visualization tools, include:

- Domain geometry and grid display
- Vector plots
- Line and shaded contour plots
- 2D and 3D surface plots
- Particle tracking

More recently these facilities may also include animation for dynamic result display and in addition to graphics all codes produce trusty alphanumeric output and have data export facilities for further manipulation external to the code. [95]

2.3.2.1 Conservation laws of fluid motion and boundary conditions

The governing equations of fluid flow represent mathematical statements of the conservation laws of physics:

- The mass of a fluid is conserved.

- The rate of change of momentum equals the sum of the forces on a fluid particle (Newton's second law).
- The rate of change of energy is equal to the sum of the rate of heat addition to and the rate of work done on a fluid particle (first law of thermodynamics).

The fluid is regarded as a continuum. We consider a small element of fluid with sides δx, δy, and δz. The element is so small that fluid properties at the faces can be expressed accurately enough by means of the first two terms of a Taylor series expansion. All fluid properties are functions of space and time. So we define $\rho(x, y, z, t)$, $p(x, y, z, t)$, $T(x, y, z, t)$, and $\mathbf{u}(x, y, z, t)$ for the density, pressure, temperature, and the velocity vector respectively. The governing equations of fluid flow are:

(i) Mass conservation or continuity equation at a point in a compressible fluid.

$$\frac{\partial \rho}{\partial t} + div(\rho \mathbf{u}) = 0 \qquad (2\text{-}9)$$

The first term on the left hand side is the rate of change in time of the density (mass per unit volume). The second term describes the net flow of mass out of the element across its boundaries and is called the convective term.

(ii) Navier-Stokes equations. Rates of increase of x-, y-, and z- momentum per unit volume

$$\frac{\partial(\rho u)}{\partial t} + div(\rho u \mathbf{u}) = -\frac{\partial p}{\partial x} + div(\mu\, grad\, u) + S_{Mx} \qquad (2\text{-}10)$$

$$\frac{\partial(\rho v)}{\partial t} + div(\rho v \mathbf{u}) = -\frac{\partial p}{\partial y} + div(\mu\, grad\, v) + S_{My} \qquad (2\text{-}11)$$

$$\frac{\partial(\rho w)}{\partial t} + div(\rho\, w\, \mathbf{u}) = -\frac{\partial p}{\partial z} + div\,(\mu\, grad\, w) + S_{Mz} \qquad (2\text{-}12)$$

u, v, and w are the momentums of x, y, and z directions. μ is the dynamic viscosity of Newtonian fluid. The overall body forces effect is included by defining a momentum source S_M.

(iii) Energy conservation equation

$$\frac{\partial(\rho i)}{\partial t} + div(\rho\, i\, \mathbf{u}) = -\,p\, div\, \mathbf{u} + div(k\, grad\, T) + \Phi + S_i \qquad (2\text{-}13)$$

i is internal energy; k is thermal conductivity. The overall effect due to viscous stresses is described by dissipation function Φ. The overall effect of potential energy change is included by defining a source term S_i.

(iv) Equations of state of perfect gas

$$p = \rho RT \qquad (2\text{-}14)$$

$$i = C_v T \qquad (2\text{-}15)$$

2.3.2.2 Turbulence and its modeling

If a fluid has a Reynolds number below the so-called critical Reynolds number Re_{crit}, the flow is smooth and adjacent layers of fluid slide past each other in an orderly fashion. If the applied boundary conditions do not change with time, the flow is steady. This regime is called laminar flow. At values of the Reynolds number above Re_{crit}, a complicated series of events takes place which eventually leads to a radical change of the flow character. The flow behavior is random and chaotic. The motion becomes intrinsically unsteady even with constant imposed boundary conditions. The velocity and all other flow properties vary in a random and chaotic way. This regime is called turbulent flow. In

a turbulent flow, particles of fluid which are initially separated by a long distance can be brought close together by the eddying motions. As a consequence, such effective mixing gives rise to high values of diffusion coefficients for mass, momentum and heat.

For most engineering purposes it is unnecessary to resolve the details of the turbulent fluctuations. Only the effects of the turbulence on the mean flow are usually sought. The most common turbulence models are mixing length model, k-ε model, Reynolds stress equation model, etc. The k-ε model, or the two-equation model, is the most widely used and validated model. It focuses on the mechanisms that affect the turbulent kinetic energy, and perform particularly well in confined flows where the Reynolds shear stresses are most important. It is also the simplest turbulence model for which only initial and boundary conditions need to be supplied. Details about k-ε model can be found in Launder and Spalding's work [96].

2.3.2.3 Finite volume method

Based on the transport equations governing fluid flow described above, the finite volume (or control volume) method is developed as the numerical tool to solve the equations. The general solution process is as follows. [95]

Step 1: Grid generation

The first step in the finite volume method is to divide the domain into discrete control volumes. A number of nodal points are put in the studied space. The boundaries of the control volumes are positioned mid-way between adjacent nodes. Thus each node is surrounded by a control volume or cell. A system of notation is then established for the use of next step.

Step 2: Discretization

To integrate the governing equations over a control volume to yield a discretized equation at its nodal point.

Step 3: Solution of equations

Discretized equations are set up at each of the nodal points. The resulting system of linear algebraic equations is then solved to obtain the distribution of the property at nodal points.

Chapter Three: Experiment Details

3.1 Materials and properties

3.1.1 Rare earth oxide raw materials

The raw materials for spraying in this research were Y_2O_3, Sm_2O_3, Dy_2O_3, and Lu_2O_3 (from AMR Technologies Inc., purity 99.5 wt.%). Their physicochemical properties are listed in **Table 3.1**. Sm, Dy, and Lu were chosen because they are typical large, medium, and small ionic radii rare earth, respectively in the rare earth series. They have sequential electron configurations and melting points, which will cause them to respond to the plasma treatment much differently from each other. Y_2O_3 was chosen because of its special position outside the lanthanide series and its wide range of applications in various fields. All the raw material particles are in irregular shapes, with a wide particle size distribution from submicron to 20 μm. The Sm_2O_3 raw material comprises a majority of B-type monoclinic phase, space group C12/m1 (JCPDS-ICDD 42-1464), and a minor C-type cubic phase (7 wt.%), space group $Ia\bar{3}$ (JCPDS-ICDD 15-0813). In contrast, the raw materials of Y_2O_3, Dy_2O_3 and Lu_2O_3 only contain C-type cubic phase, space group $Ia\bar{3}$ (JCPDS-ICDD 41-1105, 22-0612 and 12-0728, respectively).

Table 3.1. Physicochemical properties of rare earth oxide raw materials [23]

Mater.	Formula wt.	Color	Density ($g \cdot cm^{-3}$)	m.pt. (°C)	b.pt. (°C)	Structure type	Ionic radii (C.N.=6) (pm)	Element electron conf.
Y_2O_3	225.8	white	5.0	2430	4300	C	104	$4d^15s^2$
Sm_2O_3	348.8	cream	7.1	2335	3780	B/C	110	$4f^66s^2$
Dy_2O_3	373.0	white	8.2	2408	3900	C	105	$4f^{10}6s^2$
Lu_2O_3	397.9	white	9.4	2490	3980	C	100	$4f^{14}5d^16s^2$

3.1.2 Auxiliary materials

The properties of auxiliary materials including plasma gases and suspension solvents are listed in **Table 3.2**.

Table 3.2. Physicochemical properties of auxiliary materials

Material	Formula	Molecular weight	Purity	Function	Heat of vaporization (kJ/kg)	Heat of combustion (kJ/kg)
Argon	Ar	39.948	99.9%	Plasma gas	-	-
Oxygen	O_2	32	99.9%	Plasma gas	-	-
Deionized water	H_2O	18.016	-	Solvent	2258	-
Ethanol	C_2H_6O	46.07	99.5%	Solvent	838	26800
Acetone	C_3H_6O	58.081	99.5%	Solvent	525	29000

3.2 Equipment

The spraying was carried out using a 35 kW TEKNA plasma system with PL-35 induction RF plasma torch operating at 3 MHz (**Fig. 3.1**). The installation consists of a RF power supply, a plasma torch, plasma gas control system, vacuum pumping system, water cooling system, a powder feeder, a suspension feeder, and three powder collection chambers. The discharge is sustained through the inductive coupling of energy from the oscillator circuit into the plasma. The plasma torch in **Fig. 3.2** is constructed of a water-cooled plasma confinement tube surrounded by a 4 turn induction coil connected to the RF power supply through the tank circuit. The upstream part of the torch is the gas distributor head which is responsible for the introduction of the different gas streams into the discharge chamber. It is designed to create the proper flow pattern necessary to insure the stability of the discharge in the center of the coil region. A water-cooled stainless steel probe, which penetrates through the torch head, is used to introduce the powder or liquid form reactants into the center of the discharge. Due to the complexity of the flow pattern in the discharge region, the position of the tip of the injection probe is of critical importance. If located too high above the plasma, it could result in the excessive deposition of the processed material on the walls of the plasma confinement tube which

may lead to its eventual failure. Too low of a position of the tip of the injection probe will cause, on the other hand, an excessive cooling of the plasma, and a reduction of the residence time in the discharge. This will give rise to a reduction of the ability of the plasma to completely melt and process the material in-flight. The downstream end of the torch is a water-cooled exit nozzle, which acts essentially as an interface between the plasma torch and the processing chamber insuring vacuum tightness through proper seals.

Argon was used as plasma central gas, sheath gas, and powder carrier gas or suspension atomization gas. The corresponding flow rates were fixed at 20, 50, and 6 slpm (standard liters per minute), respectively. In addition, oxygen was used as a secondary plasma gas in some cases. Spraying was done at a power input of 22 kW and a chamber pressure of 400 Torr. For powder spraying, the raw material was fed by a pair of screw conveyers of the powder feeder at a constant rate, carried by argon gas, and injected axially into the center of the plasma plume through a probe. For suspension spraying, raw material powder was dispersed in various solvent at a certain concentration to make a suspension. With constant stirring, the suspension was fed at a fixed flowrate by a peristaltic pump and was atomized by Ar gas before being axially injected into the center of the plasma plume. After plasma treatment, the material was quenched at an extremely high speed and was subsequently collected by cyclone into three water-cooling chambers. The chambers enabled the classification of particles with different size ranges. The principle is that particles with different size have different weight, thus they subside at different stages of the path when carried by the cyclone. From chamber 1 (C1), chamber 2 (C2) to chamber 3 (C3), the collected powders have a tendency of decreasing particle size. Basically, C1 collects mostly micron-sized particles, C2 has the mixture of submicron and nanoparticles, and C3 are mainly nanoparticles.

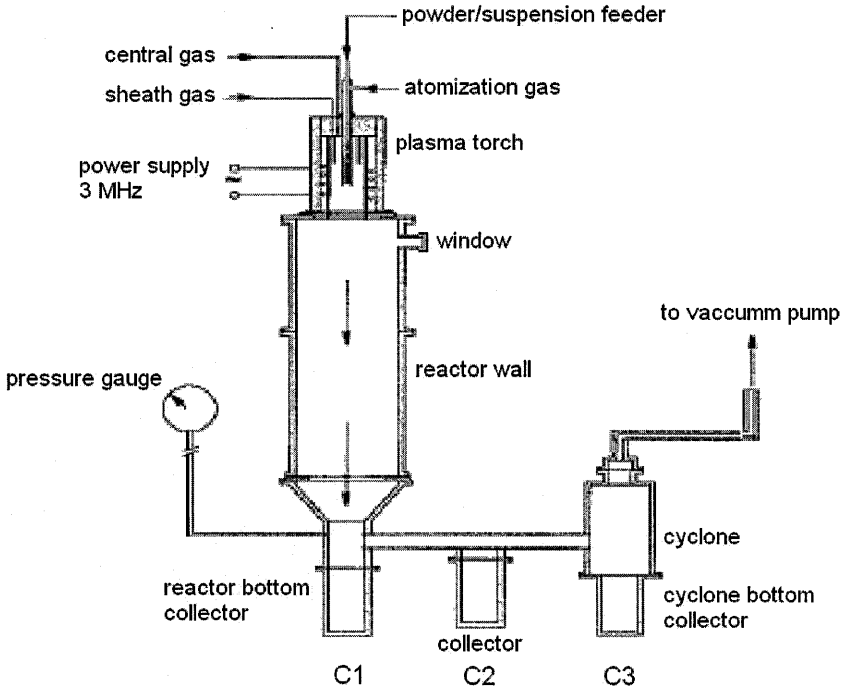

Fig. 3.1. Installation of TEKNA induction RF plasma spraying system

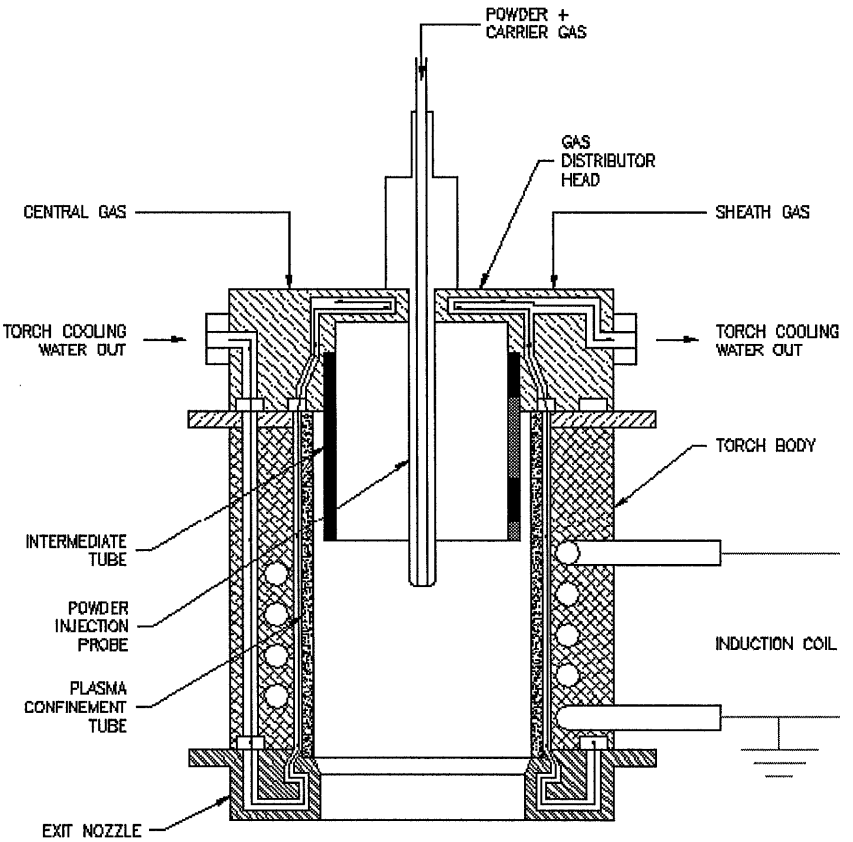

Fig. 3.2. Schematic diagram of TEKNA induction plasma torch

3.3 Plasma spraying scheme

3.3.1 Powder feed spraying of R_2O_3 by Ar and Ar/O_2 plasma

At the beginning of this research, a traditional powder feed method was employed for the plasma sprayings of rare earth oxides R_2O_3 (R = Y, Sm, Dy, and Lu). Initially Ar was used as central, sheath, and carrier gas. Afterwards, to elevate the plasma enthalpy and the heat treatment degree, O_2 was introduced as secondary plasma gas in both central and sheath gas with Ar. The maximum O_2 ratio was limited by system conditions. Exceeding the maximum value will result in extinguishing of the plasma. The detailed experimental parameters are listed in **Table 3.3**.

Table 3.3. Experimental parameters of powder feed spraying

Exp.	Mater.	Central gas (slpm)	Sheath gas (slpm)	Carrier gas (slpm)	Power (kW)	Pressure (Torr)	Feedrate (g/min)	Injector inside torch (mm)
1	R_2O_3	Ar: 20	Ar: 50	Ar: 6	22	400	1	120
2		Ar: 15 O_2: 5	Ar: 10 O_2: 40	Ar: 6	22	400	1	120

3.3.2 Suspension feed spraying of Y_2O_3 with various solvents and concentrations by Ar plasma

Because powder feed induced serious clogging problem at the feeder and tubes, suspension feed (SPS) method was adopted. As the feedstock, Y_2O_3 was dispersed in solvent and constantly stirred by magnetic stirrer to form a suspension during spraying. Water, ethanol, and acetone were used as solvent. For water suspension, suspensions with concentrations of 10, 20, and 30 wt.% were studied. For organic solvents, only 10 wt.% concentration was studied. In addition, to eliminate the carbon impurity caused by organic solvent decomposition, O_2 was introduced as secondary plasma gas for the acetone runs. The detailed experimental parameters are listed in **Table 3.4**.

Table 3.4. Experimental parameters of suspension feed spraying of Y_2O_3

Exp.	Mater.	Solvent	Concen-tration (wt.%)	Central gas (slpm)	Sheath gas (slpm)	Atomiza-tion gas (slpm)	Power (kW)	Pressure (Torr)	Feedrate (g/min)	Injector inside torch (mm)
3	Y_2O_3	water	10	Ar: 20	Ar: 50	Ar: 6	22	400	11	120
			20	Ar: 20	Ar: 50	Ar: 6	22	400	11	120
			30	Ar: 20	Ar: 50	Ar: 6	22	400	11	120
		ethanol	10	Ar: 20	Ar: 50	Ar: 6	22	400	11	120
		acetone	10	Ar: 20	Ar: 50	Ar: 6	22	400	11	120
		acetone	10	Ar: 15 O_2: 5	Ar: 30 O_2: 20	Ar: 6	22	400	11	120

3.3.3 Suspension feed spraying of R_2O_3 with various solvents by Ar and Ar/O_2 plasma

Suspension plasma spraying (SPS) was applied to all four rare earth oxides studied in this research. The suspensions were made of water solvent and acetone solvent, with a concentration of 10 wt.%. The sprayings were conducted in both Ar plasma and Ar/O_2 plasma, aiming to study the O_2 effects on SPS with different solvents. As the suspension injection affected the plasma conditions substantially, the O_2 ratio did not reach the same level as in powder spraying. The detailed experimental parameters are listed in **Table 3.5**.

Table 3.5. Experimental parameters of suspension feed spraying of R_2O_3

Exp.	Mater.	Solvent	Concen-tration (wt.%)	Central gas (slpm)	Sheath gas (slpm)	Atomiza-tion gas (slpm)	Power (kW)	Pressure (Torr)	Feedrate (g/min)	Injector inside torch (mm)
4	R_2O_3	water	10	Ar: 20	Ar: 50	Ar: 6	22	400	11	120
		water	10	Ar: 15 O_2: 5	Ar: 30 O_2: 20	Ar: 0	22	400	11	120
5		acetone	10	Ar: 20	Ar: 50	Ar: 6	22	400	11	120
		acetone	10	Ar: 15 O_2: 5	Ar: 30 O_2: 20	Ar: 0	22	400	11	120

3.3.4 Spraying synthesis of $Sm_{2-x}Lu_xO_3$ rare earth mixed oxide nanoparticles

$Sm_{2-x}Lu_xO_3$ (x = 0, 0.1, 0.2, 0.4, 0.6, 0.68, 0.8, 0.87, 1.0, 1.06, 1.2, 1.4, 1.6, 1.8, 2.0) rare earth mixed oxide series nanoparticles were synthesized by plasma spraying with two approaches. In the first approach, the in-flight synthesis of mixed oxides nanoparticles

was tried. A mixture of Sm_2O_3 and Lu_2O_3 with various atomic ratios was prepared by ball milling for 14 h. After that, this mixture was sprayed using the experimental parameters listed in Table 3.6. However, the mixture failed to combine into mixed oxides. In a second approach, the ball milled mixture of Sm_2O_3 and Lu_2O_3 was initially pressed into pellets at a pressure of 100 MPa, and then sintered at a temperature $T = 1600°C$ for a duration of $t =$ 8 h. Using an agate mortar, the sintered pellets were crushed and ground into powders. Afterwards, plasma sprayings of the ground powders were done using the same process parameters in **Table 3.6**. XRD analysis confirmed that mixed oxides were formed in this way. A detailed study on their crystal structure was carried out using XRD and Rietveld refinement.

Table 3.6. Experimental parameters of powder feed spraying of $Sm_{2-x}Lu_xO_3$

Exp.	Mater.	Central gas (slpm)	Sheath gas (slpm)	Atomization gas (slpm)	Power (kW)	Pressure (Torr)	Feedrate (g/min)	Injector inside torch (mm)
6	$Sm_{2-x}Lu_xO_3$	Ar: 20	Ar: 50	Ar: 6	22	400	1	120

3.4 Characterization

The size distributions of the as-sprayed particles were studied using Fritsh Analysette 22 Laser Particle Sizer (for submicron to micron-sized particles), Malvern Zetasizer Nano ZS (for nanoparticles), and Brookhaven BI-APD Dynamic Light Scattering (for nanoparticles). The morphology of the particles was studied using Scanning Electron Microscopy (SEM, JEOL JSM 6340F) and transmission electron microscopy (TEM, JEOL JEM 2010). For phase analysis, X-ray diffraction (XRD) experiments were done in Bragg-Brentano geometry employing a Shimadzu 6000 diffractometer with Cu-$K\alpha$ radiation (λ = 1.5418 Å). To determine the lattice parameters as well as the quantitative phase composition, further evaluation of the diffraction patterns by means of the Rietveld refinement method was carried out using the TOPAS software [97]. Space group and

structure information of relevant phases from ICSD (Inorganic Crystal Structure Database) was taken as reference. Elemental analysis was performed using X-ray Fluorescence Spectrometry (XRFS, Philips PW 2400). Differential scanning calorimetry (NETZSCH DSC 404) was employed to determine the phase transformation temperature of sprayed particles.

Chapter Four: Results

4.1 Powder feed spraying of R_2O_3 by Ar plasma

At the beginning, a traditional powder feed method was adopted for the spraying of Sm_2O_3, Dy_2O_3, and Lu_2O_3, which have large, medium, and small ionic radii respectively. The properties of the as-sprayed particles that we examined included particle morphology (shape, mean size, and size distribution), productivity, and crystal structure. Y_2O_3 was also sprayed and studied here for comparison.

4.1.1 Particle morphology

Fig. 4.1 shows the SEM micrographs of Sm_2O_3, Dy_2O_3, and Lu_2O_3 materials before and after plasma spraying. The micrographs of Y_2O_3 sprayed particles are not shown here because of their resemblance to those of Dy_2O_3. As indicated in **Fig. 4.1**, (a_0), (b_0), and (c_0), the raw materials particles have dimensions mostly in the micron range, with irregular shapes. After plasma spraying, the size and morphology changed. Particles collected in chambers C1 and C2 consisted mainly of micron-sized spheres with smooth surfaces (**Fig. 4.1**, (a_1), (b_1), (c_1) and (a_2), (b_2), (c_2)), which indicated that the particles underwent a melting history during processing. The presence of a small amount of irregularly shaped large particles can be explained by insufficient heat treatment and, consequently, incomplete melting of the raw material particles. Additionally, the sprayed powders collected in chambers C1 (**Fig. 4.1**, (a_1), (b_1), (c_1)) and C2 (**Fig. 4.1**, (a_2), (b_2), (c_2)) contained a small fraction of nanoparticles which were exhibited as the light-gray clusters visible in the background of the pictures. Taking C3 powders (**Fig. 4.1**, (a_3), (b_3), (c_3)) into consideration, it can be observed that the fraction of nanoparticles increased in

the order of C1→C2→C3. Comparing the morphology of different rare earth oxide particles collected in the same chamber indicates another tendency. With increasing atomic number of the rare earth metal, the fraction of the micron-sized spherical particles increases and, accordingly, that one of the nanoparticles decreases, as can be seen for the C3 powders in **Fig. 4.1**, (a_3), (b_3), (c_3).

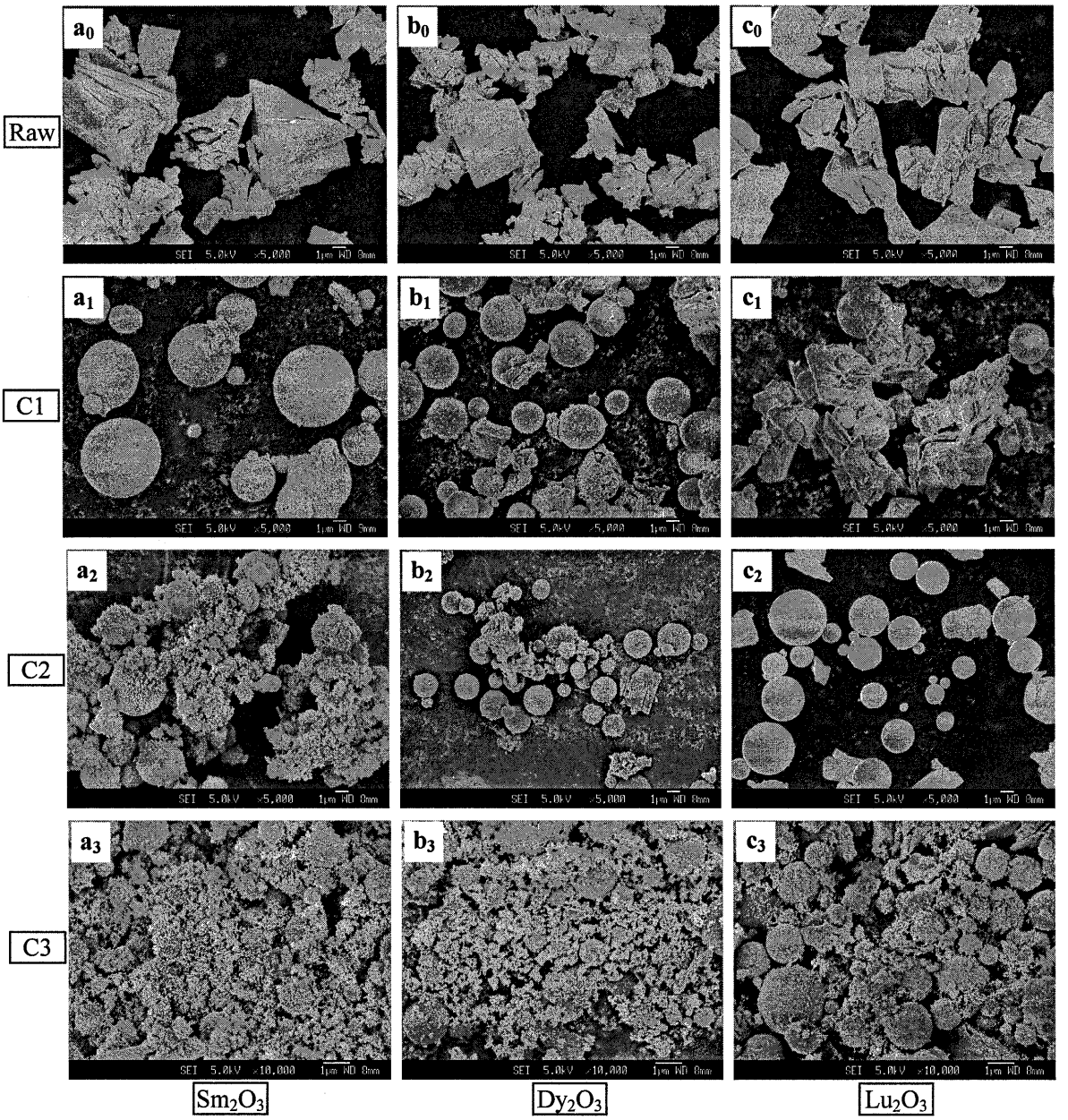

Fig. 4.1. SEM micrographs of particles from raw materials and powder feed spraying by Ar plasma. (a, b, and c stand for Sm_2O_3, Dy_2O_3, and Lu_2O_3. The footnotes 0, 1, 2, and 3 represent raw material, C1, C2, and C3 particles in sequence)

TEM micrographs of R_2O_3 nanoparticles from chamber C3 in **Fig. 4.2** exhibit a particle size distribution from 5 to 80 nm. Instead of being totally spherical, some of the nanoparticles are of elliptical or irregular shape. Additionally, high resolution TEM pictures (**Fig. 4.2** (d)) show that nanoparticles with sizes below 50 nm are monocrystalline. In some cases, there is a small amount of amorphous phase connecting the single crystallites (**Fig. 4.2** (c)). This amorphous phase might be the consequence of extremely high speed cooling of the vapor phase material.

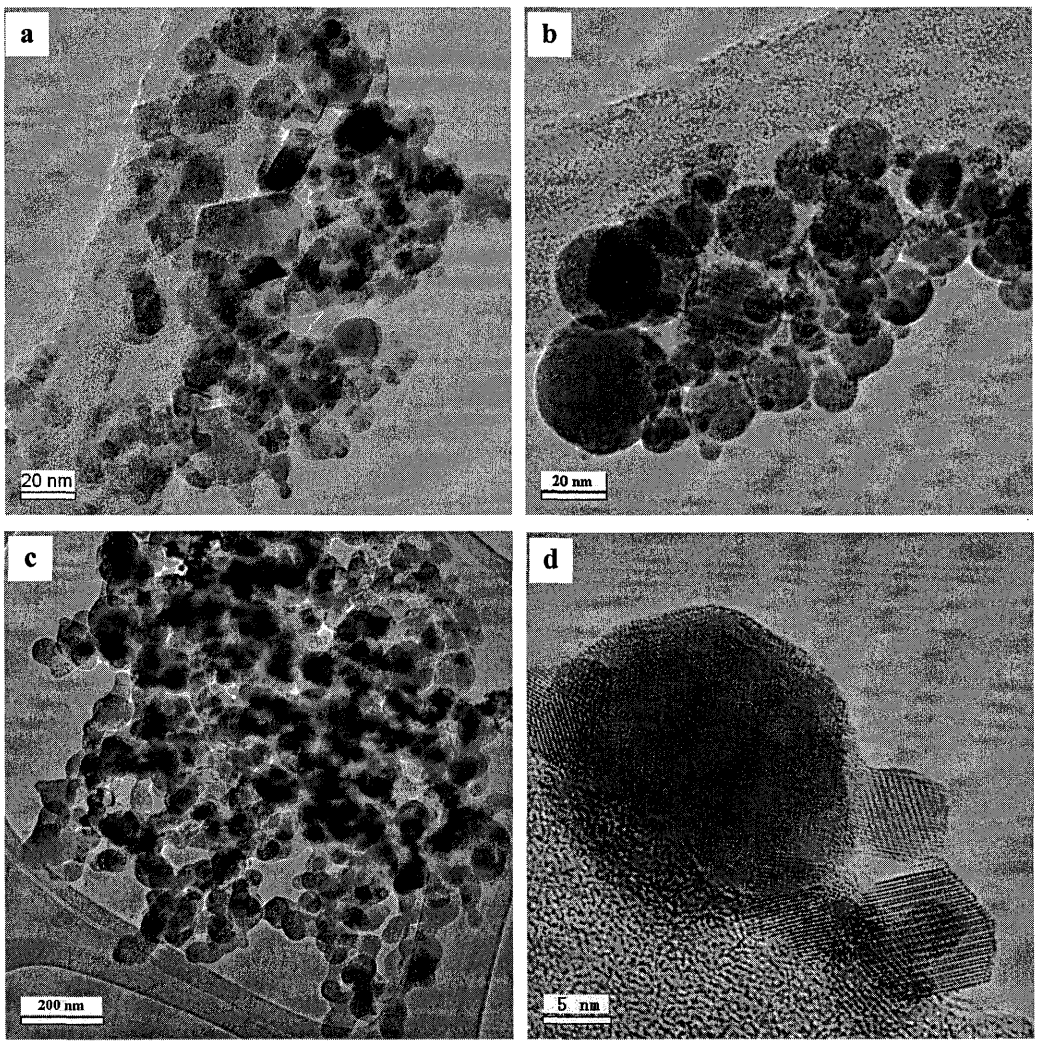

Fig. 4.2. TEM micrographs of nanoparticles from powder feed spraying by Ar plasma in chamber C3. (a) Y_2O_3; (b) Sm_2O_3; (c) Dy_2O_3; (d) Lu_2O_3

In order to quantitatively examine the particle size change before and after spraying, raw material, C1, and C2 particles were measured by micron-sized particle analyzer, while C3

particles by nanoparticle analyzer. Before spraying, Sm_2O_3, Dy_2O_3, and Lu_2O_3 raw material particles were mainly in micron size, with a wide particle size distribution from submicron to 20 μm (**Fig. 4.3** (a)). After spraying, for the same material, the mean size of the collected particles decreased in the order of Raw→C1→C2→C3, and the size distribution became narrower in the same order (e.g. Dy_2O_3 results in **Fig. 4.3** (b)). Furthermore, for different materials in a certain chamber, combing the results in **Fig. 4.3** (a), (c), and (d), C1 and C2 particles both had a size decreasing and distribution narrowing trend in the order of Lu_2O_3→Sm_2O_3→Dy_2O_3, which is relative to their raw materials. As for the nanoparticles from C3, the results in **Fig. 4.4** suggest that they have average particle sizes around 50 nm. Their mean sizes and distributions have a similar trend across Lu_2O_3→Sm_2O_3→Dy_2O_3 as C1 and C2 do. Nevertheless, due to the effect of agglomeration, nanoparticles below 30 nm, which can be observed under TEM, were unable to be detected by the laser.

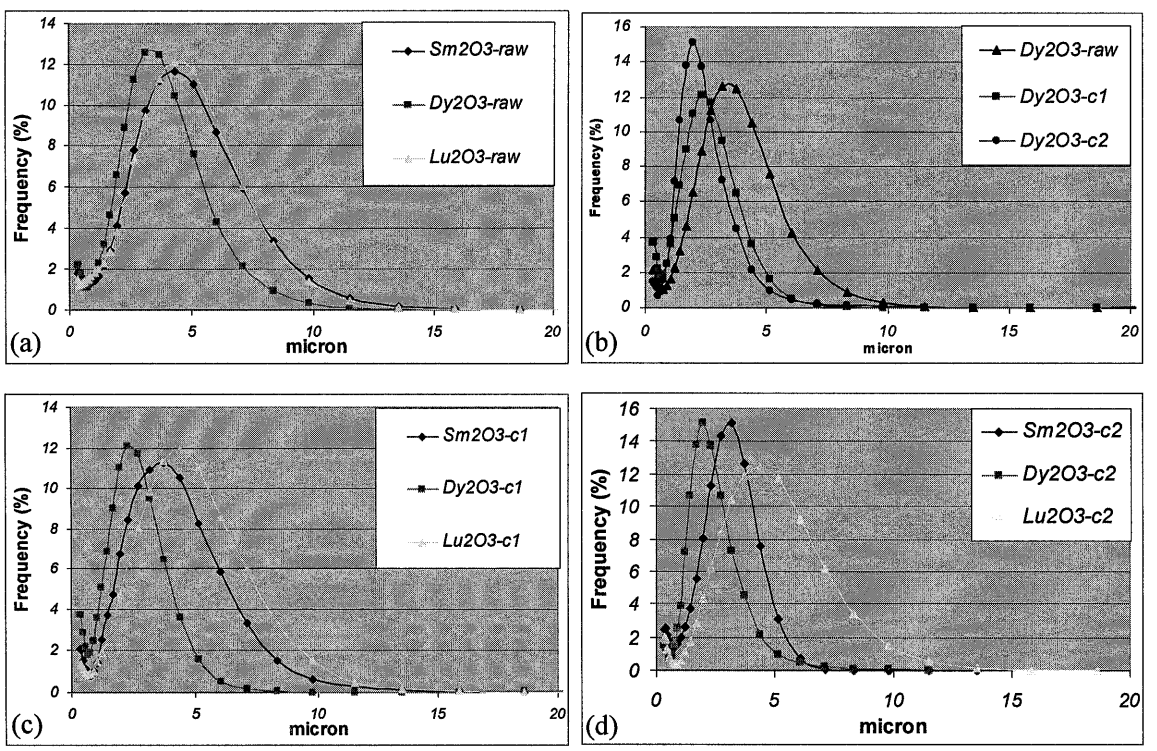

Fig. 4.3. Size distribution of particles of raw materials and powder feed spraying by Ar plasma. (a) raw materials; (b) Dy_2O_3 raw material and sprayed particles; (c) C1 sprayed particles; (d) C2 sprayed particles

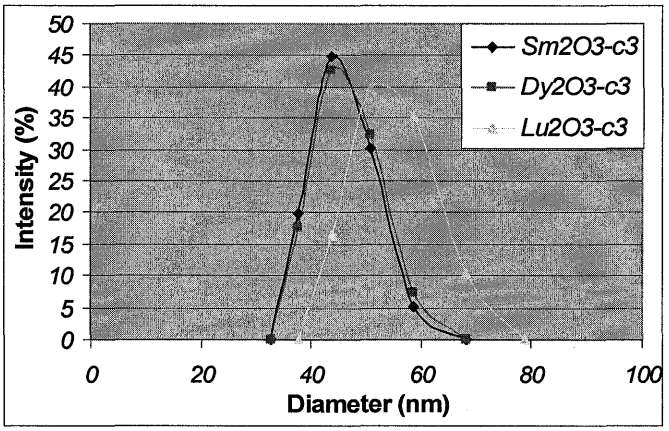

Fig. 4.4. Size distributions of C3 nanoparticles from powder feed spraying by Ar plasma. (a) Sm_2O_3; (b) Dy_2O_3; (c) Lu_2O_3

4.1.2 Productivity

The productivity of sprayed particles in any chamber C_x was calculated using the following formula:

$$\text{Productivity of } C_x = \frac{\text{Weight of particles collected in } C_x}{\text{Weight of total collected particles}}, \qquad x = 1, 2, \text{ or } 3.$$

The productivities of sprayed R_2O_3 particles from C3 are illustrated in **Fig. 4.5**. It can be seen that they have a descending sequence across $Sm_2O_3 \rightarrow Dy_2O_3 \rightarrow Y_2O_3 \rightarrow Lu_2O_3$.

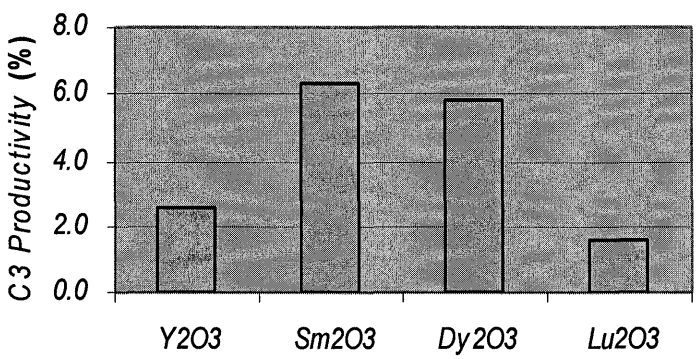

Fig. 4.5. Productivities of C3 nanoparticles of powder feed spraying by Ar plasma

4.1.3 Crystal structure

To determine the phase composition and lattice parameters changes of the sprayed particles, XRD measurements were conducted and the results were analyzed by Rietveld

refinement. As there was no reliable structure information for monoclinic Y_2O_3, Dy_2O_3 and Lu_2O_3 from JCPDS database, structure data of monoclinic Sm_2O_3 was used for Rietveld refinement. The Sm_2O_3 raw material consists mainly of monoclinic B-type phase (JCPDS-ICDD 42-1464). Additionally, there is a small amount (7 wt.%) of the cubic C-type phase (JCPDS-ICDD 15-0813). In contrast, the raw materials of Dy_2O_3 and Lu_2O_3 only contain the cubic C-type phase (JCPDS-ICDD 22-0612 and 12-0728, respectively). Structure analysis of Y_2O_3 will be discussed in section 4.3. For all rare earth oxide particles, plasma spraying resulted in an increase of the fraction of the monoclinic B-type phase. Taking Dy_2O_3 for example (**Fig. 4.6**), it can be clearly identified that after spraying there are both cubic and monoclinic Bragg reflections in the diffraction patterns. Moreover, the monoclinic phase is more pronounced. Comparing the diffraction diagrams for the sprayed Dy_2O_3 particles in more detail (**Fig. 4.6**, curves (b), (c), and (d)), it can be seen that there is an intensity decrease for the cubic Bragg reflections in the order C1→C2→C3. Correspondingly, as shown in **Fig. 4.7,** the fraction of the monoclinic phase increases by quantitative phase analysis results. It should be mentioned that calcination of sprayed Dy_2O_3 particles in chamber C2 at 900°C for 4 h did not result in obvious phase composition change. Thus, this monoclinic high-temperature equilibrium phase is quite stable. Similar as Dy_2O_3, there was a plasma induced cubic→monoclinic phase transformation for the other rare earth oxides too. However, the degree of the phase transformation was different. Comparing the diffraction patterns for Sm_2O_3, Dy_2O_3, and Lu_2O_3 particles collected in chamber C3 (**Fig. 4.8**), there is an intensity decrease for the monoclinic Bragg reflections and, thus, a decrease of the fraction of the monoclinic B-type phase with increasing atomic number of the rare earth metal. This observation is confirmed by the results of the quantitative phase analysis (**Fig. 4.7**).

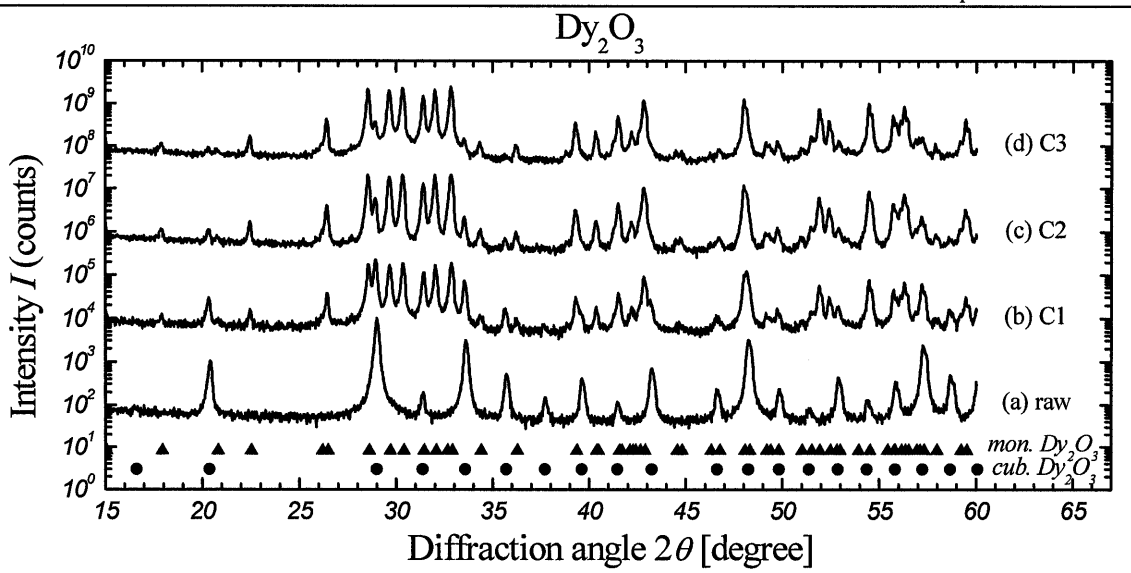

Fig. 4.6. XRD patterns of Dy_2O_3 particles from raw material and powder feed spraying by Ar plasma

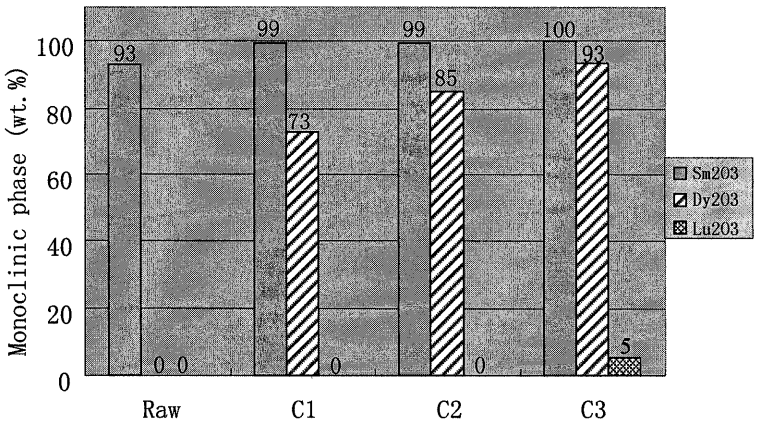

Fig. 4.7. Quantitative phase analysis using Rietveld refinement for particles from raw materials and powder feed spraying by Ar plasma

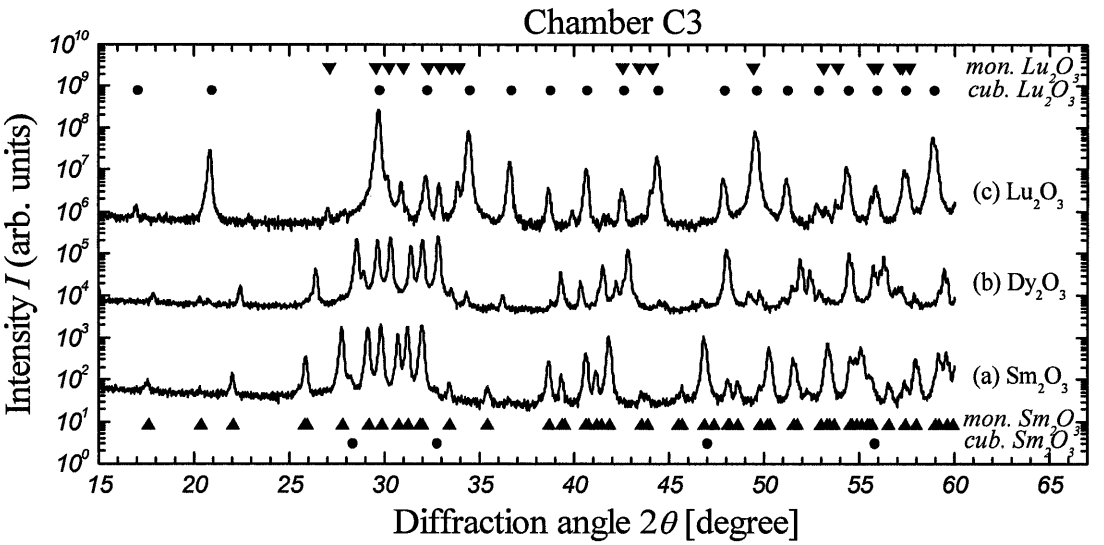

Fig. 4.8. XRD patterns of Sm_2O_3, Dy_2O_3, and Lu_2O_3 C3 particles from powder feed spraying by Ar plasma

Besides phase composition, Rietveld refinement of XRD patterns also provided lattice parameter information of the sprayed particles. The lattice parameters of Sm_2O_3, Dy_2O_3 and Lu_2O_3 sprayed particles from chamber C3 are listed together with the associated unit cell volume V as well as the equivalent volume V_{R2O3} of one molecular unit R_2O_3 in **Table 4.1**. As the fractions of cubic Sm_2O_3, cubic Dy_2O_3, and monoclinic Lu_2O_3 are very small (**Fig. 4.7**), the corresponding lattice parameters were determined with high uncertainties, resulting in large errors. Concerning the cubic phase, the lattice parameter a and, thus, the associated unit cell volume V decreased with increasing atomic number of the rare earth metal. This result can be explained by the lanthanide contraction effect and is in accordance with the shift of the cubic Bragg reflections to higher diffraction angles (**Fig. 4.8**), which can be observed best for the (222) reflection (Sm_2O_3: $2\theta = 28.2°$; Dy_2O_3: $2\theta = 28.9°$; Lu_2O_3: $2\theta = 29.7°$). A similar tendency is observed for the monoclinic phase. With decreasing lattice parameters a, b, c and increasing monoclinic angle β, the unit cell volume decreases in the order $Sm_2O_3 \rightarrow Dy_2O_3 \rightarrow Lu_2O_3$. In the case of the cubic phase, the calculated unit cell volumes are in good accordance with already published values (V_{Dy2O3} = 1214.97(24) Å^3 [98], V_{Lu2O3} = 1121.95 Å^3 [99]) whereas for the monoclinic cell, there are slight differences [100, 101], which might be caused by trace impurities in the raw material. Furthermore, for each rare earth oxide, the sprayed particles from different chambers show another unit cell contraction tendency for both cubic and monoclinic phases in the order of Raw→C1→C2→C3, as indicated in **Fig. 4.9**.

Table 4.1. Lattice parameters of as-sprayed Sm_2O_3, Dy_2O_3, and Lu_2O_3 C3 particles (the number in brackets is error)

		Sm_2O_3	Dy_2O_3	Lu_2O_3
monoclinic	a (Å)	14.1791(3)	13.9496 (8)	13.7483 (10)
	b (Å)	3.6268 (1)	3.5179 (2)	3.4044 (2)
	c (Å)	8.8540 (2)	8.6614 (5)	8.4410 (7)
	β (°)	100.043 (2)	100.169 (1)	100.256 (7)
	V (Å^3)	448.35 (2)	418.36 (4)	388.77 (5)
	$V_{R2O3,mon}$ (Å^3)	74.725	69.727	64.795
cubic	a (Å)	-	10.6657(7)	10.3927 (1)
	V (Å^3)	-	1213.30 (25)	1122.49 (3)
	$V_{R2O3,cub}$ (Å^3)	-	75.831	70.156

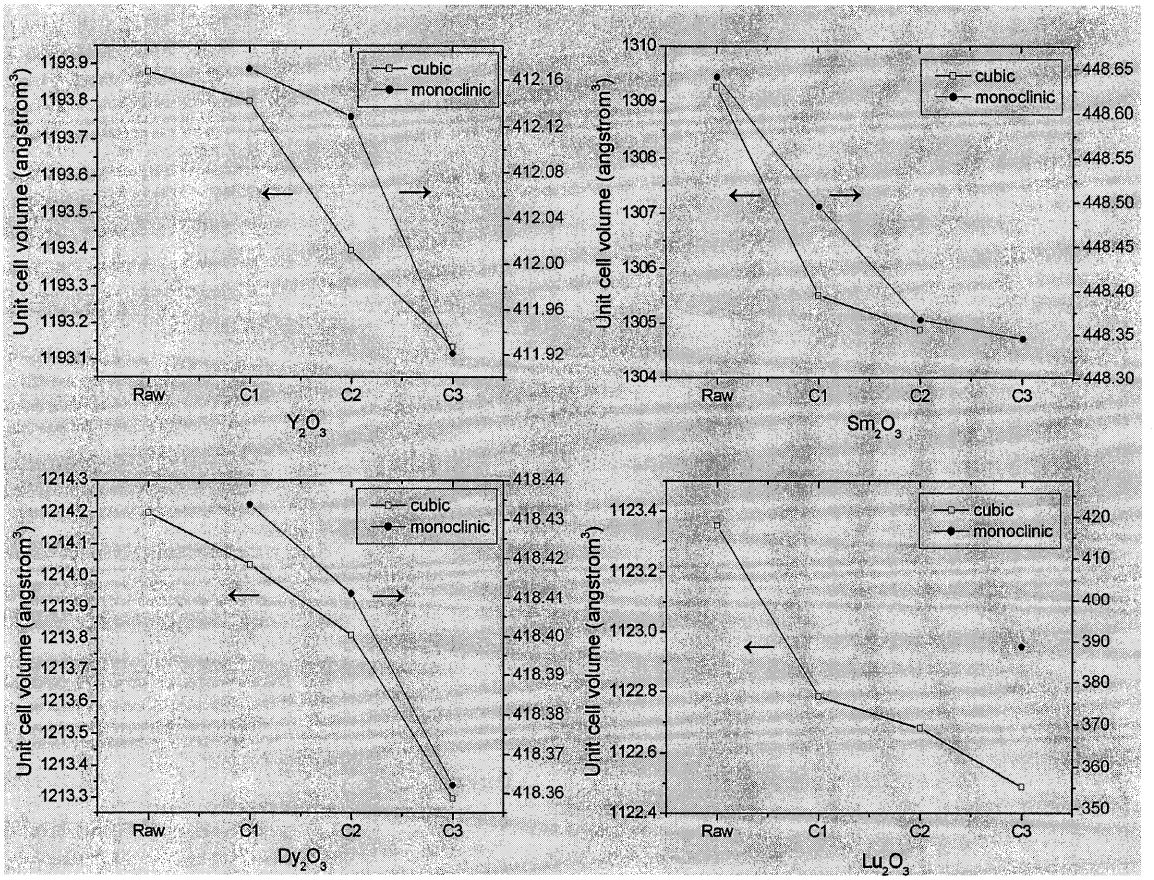

Fig. 4.9. Unit cell volumes of R_2O_3 particles from raw materials and powder feed spraying by Ar plasma

4.2 Powder feed spraying of R_2O_3 by Ar/O_2 plasma

In powder spraying by Ar plasma, a large portion of the sprayed particles remained irregular shape as raw material and the yield of nanoparticles was low, which suggests insufficient heat treatment. To elevate the plasma enthalpy, O_2 was introduced as

secondary plasma gas. As a result, the heat treatment was much improved and the particle morphology, productivity, and crystal structure changed substantially. The changing degree varies with rare earth oxides. Only the results of Y_2O_3 and Dy_2O_3 are discussed here as their changes in crystal structure were more significant.

4.2.1 Particle morphology

SEM micrographs of sprayed particles from C2 of Y_2O_3 and Dy_2O_3 are shown in **Fig 4.10**. It can be seen that particles sprayed by Ar/O_2 plasma (**Fig. 4.10**, (b) and (d)) comprise much less of irregular-shaped particles and more of nanoparticles than those sprayed by Ar plasma (**Fig. 4.10**, (a) and (c)). This suggests that a higher heat treatment level was achieved by O_2 introduction. In addition to alter the morphology of micron-sized particles, O_2 introduction also changed the particle size distribution of nanoparticles. DLS analysis of Y_2O_3 and Dy_2O_3 C3 nanoparticles in **Fig. 4.11** indicates that not only did the mean particle sizes decrease remarkably after O_2 addition, but the size distributions also became narrower. TEM micrographs of Y_2O_3 and Dy_2O_3 nanoparticles in **Fig. 4.12** confirm the size decrease. As seen from the TEM pictures, the nanoparticles are also in various shapes, and loosely agglomerated.

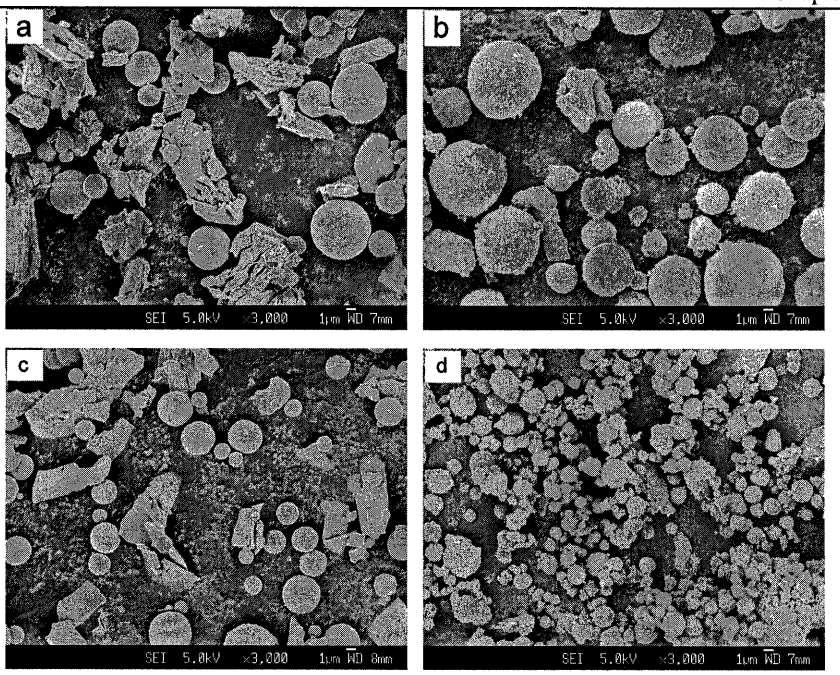

Fig. 4.10. SEM micrographs of Y_2O_3 and Dy_2O_3 C2 particles from powder feed spraying by Ar and Ar/O_2 plasma. (a) Y_2O_3 by Ar; (b) Y_2O_3 by Ar/O_2; (c) Dy_2O_3 by Ar; (d) Dy_2O_3 by Ar/O_2

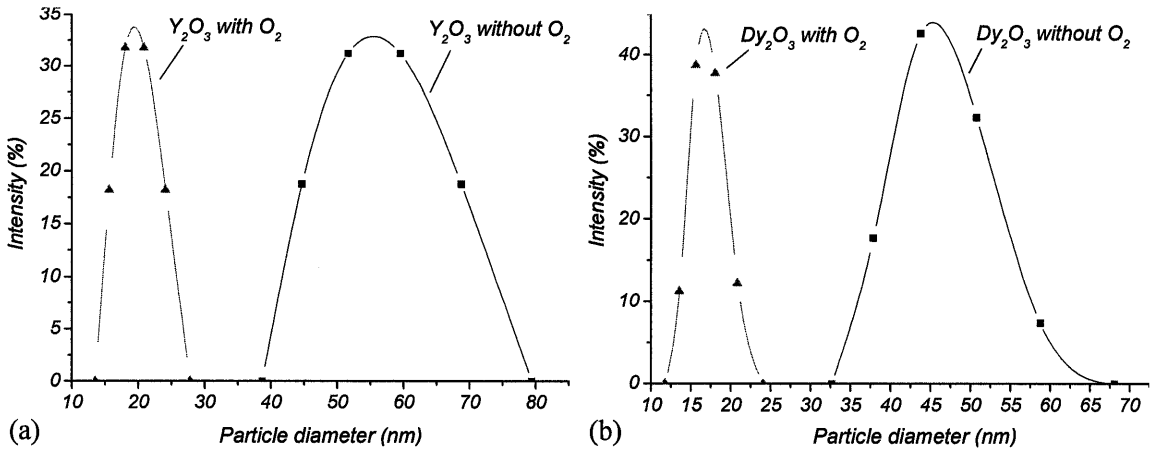

Fig. 4.11. Size distributions of C3 particles from powder feed spraying by Ar and Ar/O_2 plasma. (a) Y_2O_3; (b) Dy_2O_3

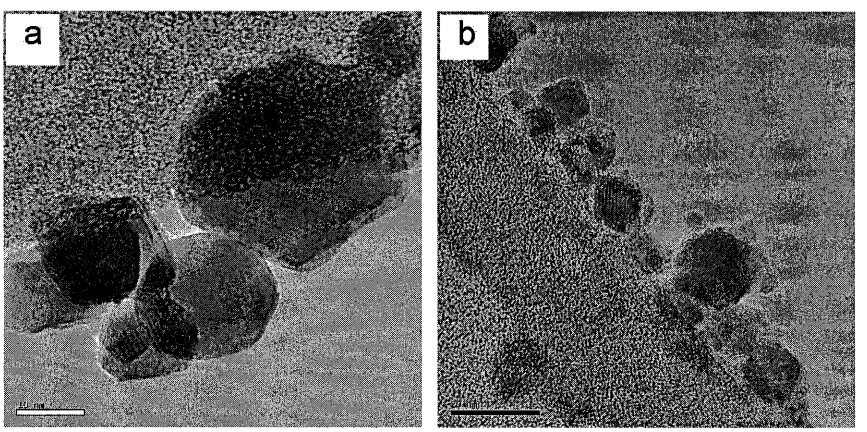

Fig. 4.12. TEM micrographs of nanoparticles from powder feed spraying by Ar/O_2 plasma. (a) Y_2O_3; (b) Dy_2O_3

4.2.2 Productivity

The productivity of C3 sprayed particles from powder feed spraying by Ar/O_2 plasma is illustrated in **Fig. 4.13**. It can be seen that O_2 addition increased C3 productivity by more than two times for all the oxides studied. However, the order of the productivities is still the same as in Ar plasma spraying.

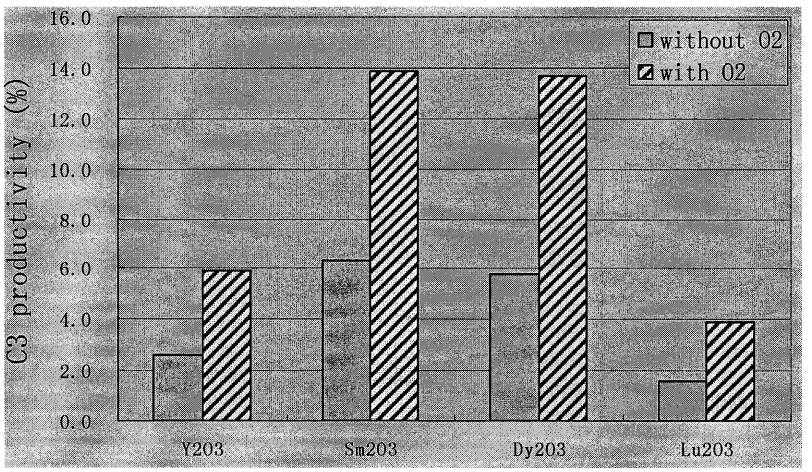

Fig. 4.13. Productivities of C3 nanoparticles from powder feed spraying by Ar and Ar/O_2 plasma

4.2.3 Crystal structure

As mentioned in section 4.1.3, plasma spraying induced a cubic→monoclinic phase transformation. This phenomenon also occurred in Ar/O_2 plasma spraying, and the effect was enhanced by O_2 introduction. As determined by the XRD pattern in **Fig. 4.14** (a), Y_2O_3 raw material has only cubic phase reflections. However, after spraying by Ar or Ar/O_2 plasma, besides the cubic phase, there is a Y_2O_3 monoclinic phase present, which is represented by the reflections between diffraction angles 29.8°-33.3° (**Fig. 4.14**, (b) and (c)). As can be seen from the XRD patterns, Y_2O_3 particles sprayed by Ar/O_2 plasma have higher intensity of monoclinic reflections than those sprayed by Ar plasma, indicating that O_2 introduction resulted in a higher degree of cubic→monoclinic phase transformation. Similarly, XRD patterns show that Dy_2O_3 sprayed particles by Ar and Ar/O_2 plasma

consist of both cubic and monoclinic phase reflections (**Fig. 4.15**, (b) and (c)), in comparison with the pure cubic phase Dy_2O_3 raw material. The monoclinic phase proportion also increased after spraying by Ar/O_2 plasma. Quantitative phase analysis data in **Fig. 4.16** obtained by XRD patterns refinement reveals the exact phase transformation degree. In both Y_2O_3 and Dy_2O_3 cases, Ar/O_2 plasma treatment resulted in a 3 wt% increase of monoclinic phase as compared to Ar plasma.

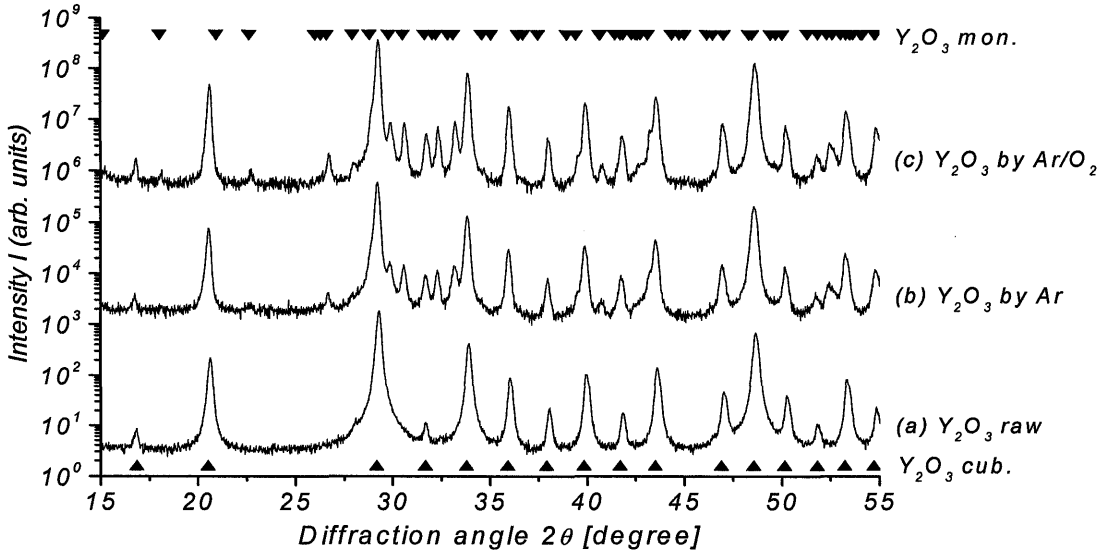

Fig. 4.14. XRD patterns of Y_2O_3 C2 particles from raw material and powder feed spraying by Ar and Ar/O_2 plasma

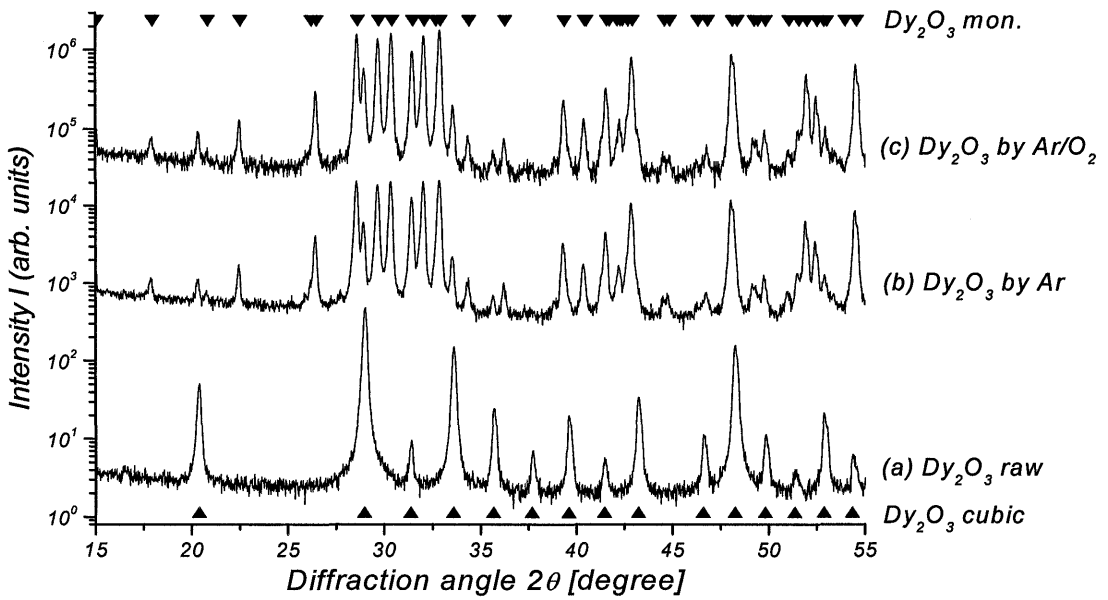

Fig. 4.15. XRD patterns of Dy_2O_3 C2 particles from raw material and powder feed spraying by Ar and Ar/O_2 plasma

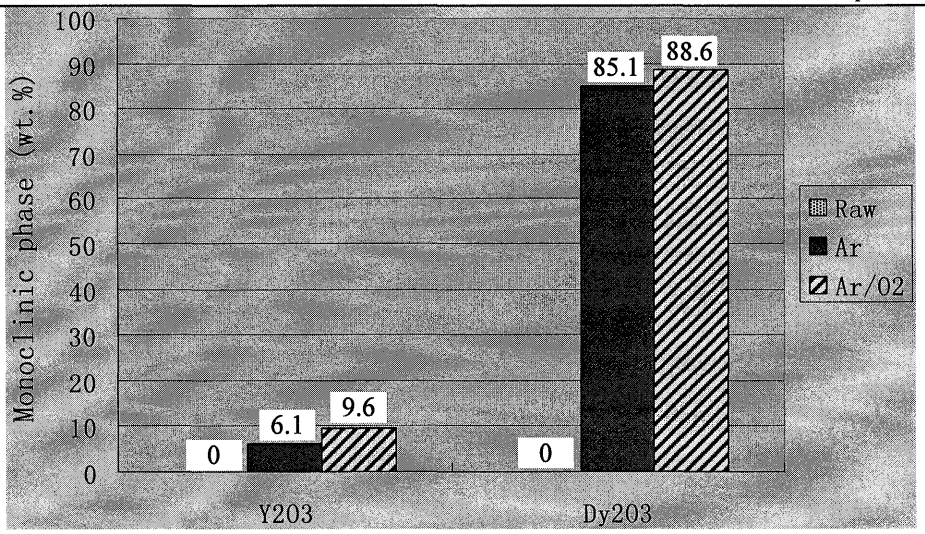

Fig. 4.16. Quantitative phase analysis using Rietveld refinement for Y_2O_3 and Dy_2O_3 C2 particles from powder feed spraying by Ar and Ar/O_2 plasma

4.3 Suspension feed spraying of Y_2O_3 with various solvents and concentrations, with Ar plasma

Although introduction of O_2 improved the plasma enthalpy and heat treatment significantly, clogging issues at the powder feeder and tubes in the powder feed spraying were still severe. This clogging problem resulted from the large molecular weight of the rare earth oxide and the small raw material particle size. It affected the consistency of the feed and, consequently, the stability of the plasma and uniformity of the products. The best way to solve this problem was to use the suspension plasma spraying (SPS) that had been developed in 1997 by Bouyer et al. [62]. Nevertheless, the SPS process has been used for only a very few low-melting point materials and its potential has not been fully explored yet. In the present research, SPS was adopted both to tackle the clogging problem and to thoroughly investigate its potential. Initially, Y_2O_3 was used to study the processing parameters such as suspension concentration and solvent type.

4.3.1 Water solvent SPS with various concentrations

The morphology and particle size distribution of Y_2O_3 raw material are shown in Fig.

4.17. At first, deionized water was used to make Y_2O_3 suspensions at concentrations of 10 wt%, 20 wt%, and 30 wt%. During plasma spraying, the suspension was gas-atomized into micron-sized droplets and fed into the plasma plume. The droplets were flash dried through liquid vaporization, and the particles were then partially melted and vaporized. Subsequently, the vapor phase underwent an extremely fast quenching and condensed into nanoparticles. On the other hand, the partially melted particles ended up with micron-sized spherical particles. Fig. 4.18 (a) shows the morphology of as-sprayed particles from 10 wt% concentration suspension (pictures of 20 wt% and 30 wt% not shown). The irregular-shaped particles indicated inadequate heat treatment, while the spherical particles with smooth surface signify a melting and vaporization history. The morphology of particles from all three concentrations is similar, except that the ratio of irregular and spherical particles varies with concentrations. The particles from 20 wt% suspension have more spherical particles and nanoparticles and less irregular particles than those from 10 wt% and 30 wt% suspensions. Thus, 20 wt% could be the optimum concentration for water SPS as it rendered the best heat treatment. However, it has to be noted that this optimum concentration may vary with solvent type. As determined by XRD patterns in Fig. 4.19 (c), the as-sprayed particles from all three concentrations are pure cubic phase with space group $Ia\bar{3}$ (JCPDS-ICDD 41-1105), identical to the starting material.

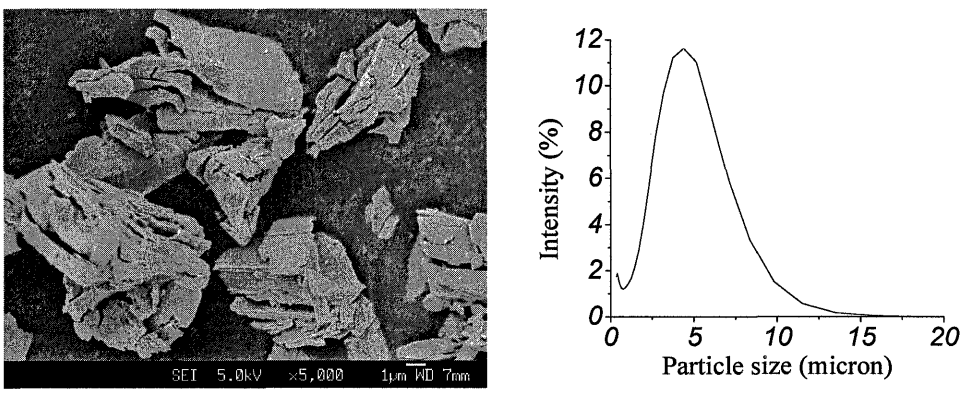

Fig. 4.17. Morphology and particle size distribution of Y_2O_3 raw material

4.3.2 Organic solvent SPS

Since water consumed a large portion of the plasma enthalpy during vaporization and degraded the plasma heat treatment, organic solvents are preferable because they absorb less heat when vaporized. Therefore, ethanol and acetone were used to prepare 10 wt% suspensions for SPS. In comparison with as-sprayed particles from water suspension (**Fig. 4.18** (a)), the particles from ethanol and acetone suspensions have fewer irregular-shaped particles and more spherical micron-sized particles with smaller size (**Fig. 4.18** (b) and (c)), suggesting an elevated heat treatment. However, these particles have a fluffy appearance and an unusual dark color in contrast to the white-colored Y_2O_3 raw material. Through XRF analysis, carbon element was identified existing in the as-sprayed particles besides yttrium and oxygen elements. Also, the XRD patterns presented in **Fig. 4.19** (a) and (b) clearly indicate the presence of several other reflections besides cubic phase Y_2O_3 reflections. As an example, the refinement curves of acetone solvent suspension spraying are shown in **Fig. 4.20**. Besides Y_2O_3 cubic phase reflections, there are some additional reflections and a structured background which is characteristic for the presence of an amorphous phase. This amorphous phase, whose morphology is identified by TEM and shown in **Fig. 4.21** (a), might be the consequence of the extremely fast cooling. Some of the additional reflections belongs to Y_2O_3 monoclinic phase which has been found in powder feed spraying (**Fig. 4.14**). The rest of the unknown reflections could be attributed to a previously unknown yttrium oxycarbide ($Y_2O_2C_2$), which is isotypic to $La_2O_2C_2$ reported by Butherus and Eick [102, 103]. The weight ratio of Y_2O_3 cubic, Y_2O_3 monoclinic, and $Y_2O_2C_2$ phases in the as-sprayed particles from C2 was refined to 93:2:5 for ethanol solvent SPS and 89:1:10 for acetone within the margins of error. EDX mapping of the nanoparticles from acetone solvent in **Fig. 4.22** reveals that the carbon element, i.e. the amorphous carbon and $Y_2O_2C_2$, distributes uniformly in Y_2O_3 matrix.

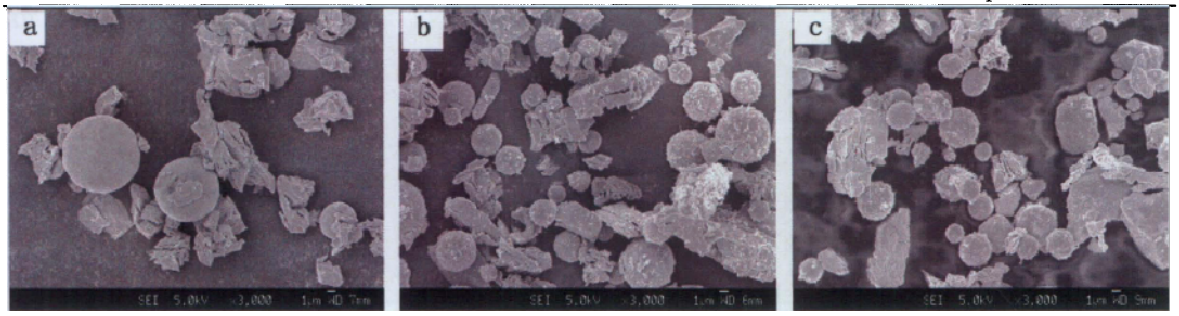

Fig. 4.18. As-sprayed Y_2O_3 C1 particles from 10 wt% SPS with a solvent of (a) water; (b) ethanol; (c) acetone

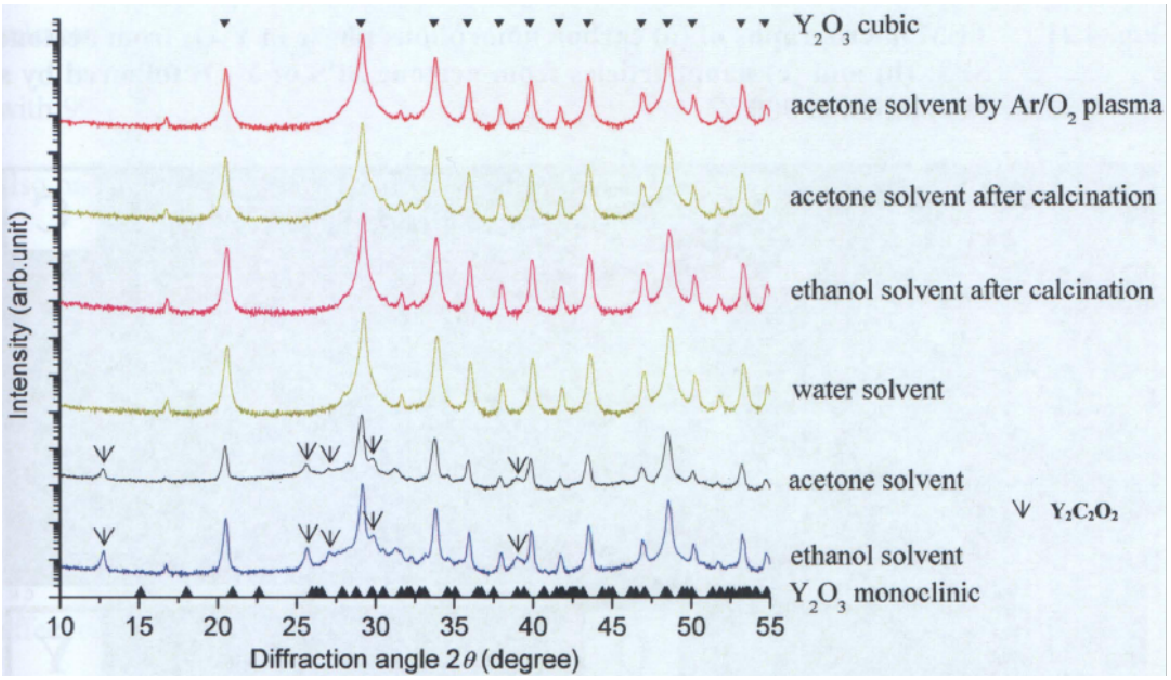

Fig. 4.19. XRD patterns of Y_2O_3 C2 particles from SPS with various solvents

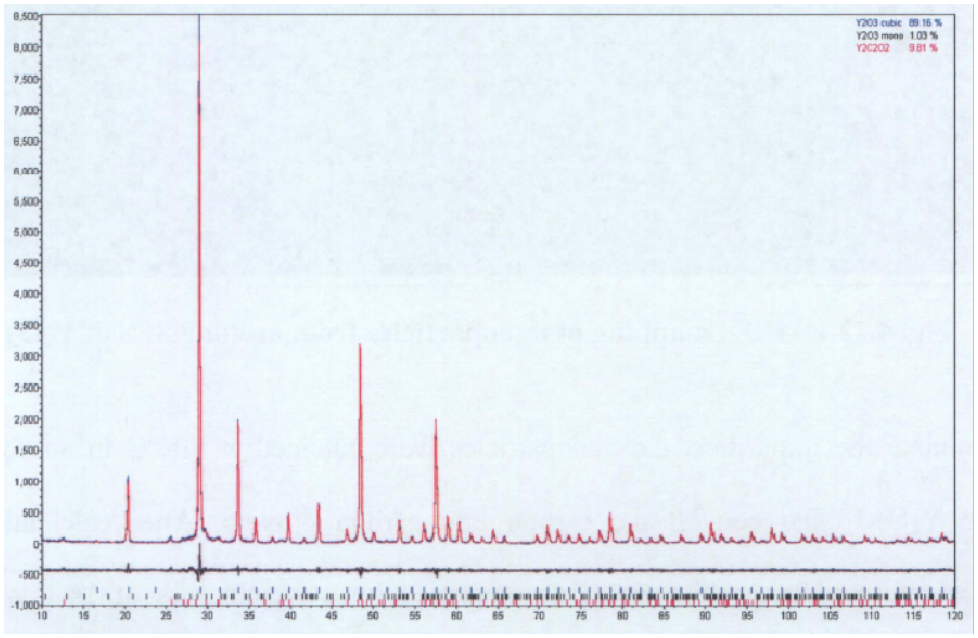

Fig. 4.20. Rietveld refinement of XRD pattern of Y_2O_3 C2 particles from acetone solvent SPS by Ar plasma

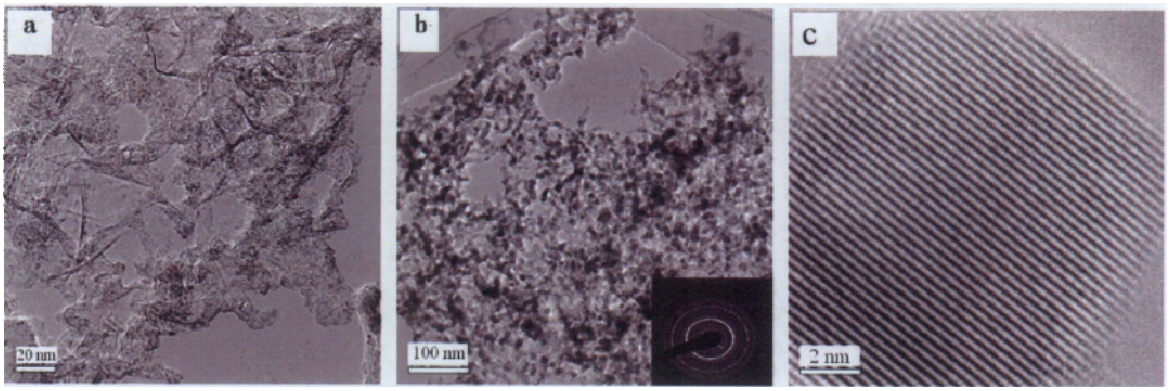

Fig. 4.21. TEM micrographs of (a) carbon amorphous phase in Y_2O_3 from acetone SPS; (b) and (c) nanoparticles from acetone SPS of Y_2O_3 followed by a calcination at 700 °C

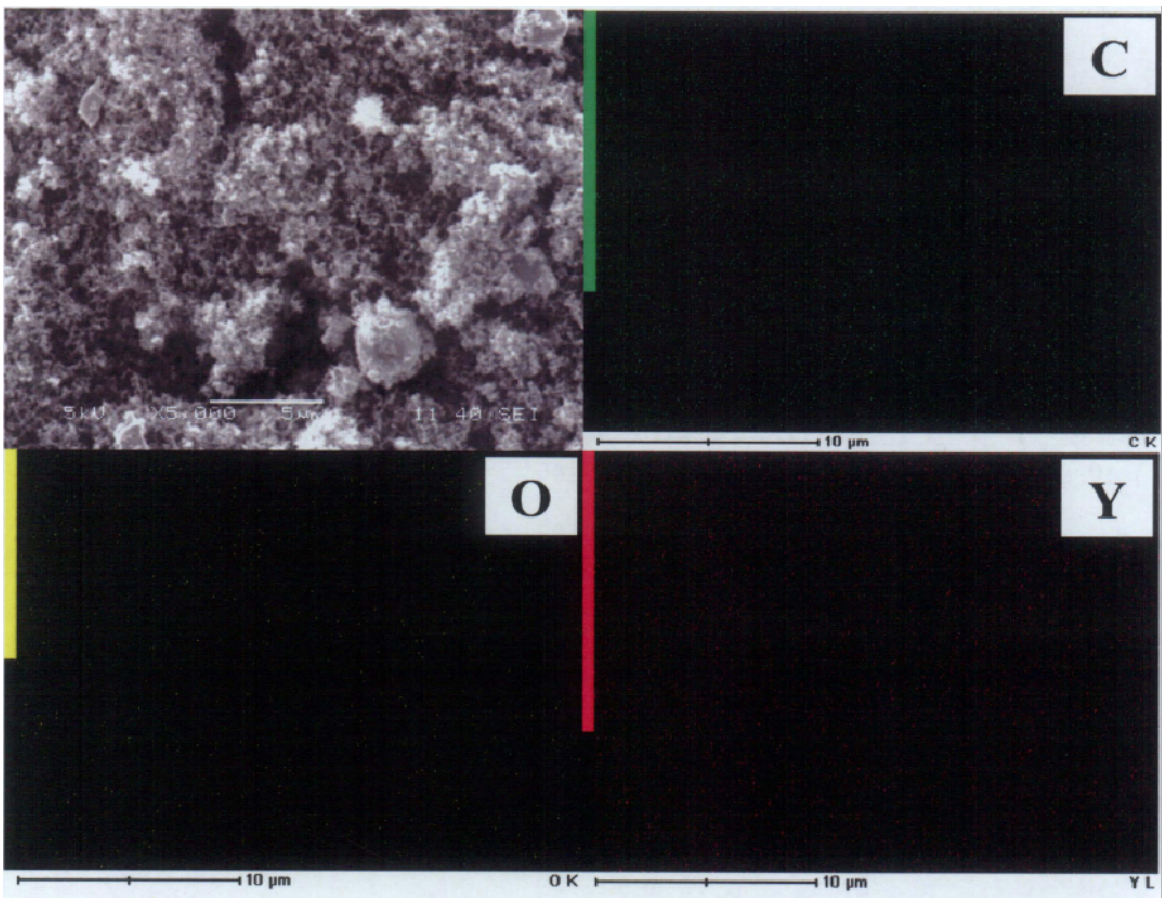

Fig. 4.22. EDX mapping of nanoparticles from acetone SPS of Y_2O_3

To eliminate the impurities, the nanoparticles were calcined at 700°C in air for 6h to oxidize $Y_2O_2C_2$ and convert the carbon into carbon dioxide. After calcination, the particles returned to a white color, accompanied by a weight loss of 14.1 wt%. No crystallite growth was observed. Finally, productivities of C3 were calculated as 3.6 g/h

for ethanol SPS and 5.1 g/h for acetone SPS, in comparison with 1 g/h for water suspension. The TEM diffraction pattern in **Fig. 4.21** (b) and high resolution micrographs in **Fig. 4.21** (c) of the calcined nanoparticles show that the nanoparticles were monocrystalline and well-dispersed. XRD patterns of the calcined particles in **Fig. 4.19** (d) and (e) show that the hump-shaped reflection caused by carbon amorphous phase and the reflections of $Y_2O_2C_2$ presented in **Fig. 4.19** (a) and (b) disappeared completely after calcination. Quantitative phase analysis indicates that the calcined particles are pure Y_2O_3 with 99 wt% cubic phase structure and 1 wt% monoclinic phase structure. XRF analysis also proved that the carbon element has been totally removed.

The size distributions of the calcined nanoparticles from an organic solvent SPS and nanoparticles from a water solvent SPS were measured by Malvern Zetasizer Nano ZS and shown in **Fig. 4.23**. It is found that the mean particle size decreases in the order of water→ethanol→acetone solvent SPS. This trend was confirmed by the peak broadening effect of the corresponding XRD patterns in **Fig. 4.19**.

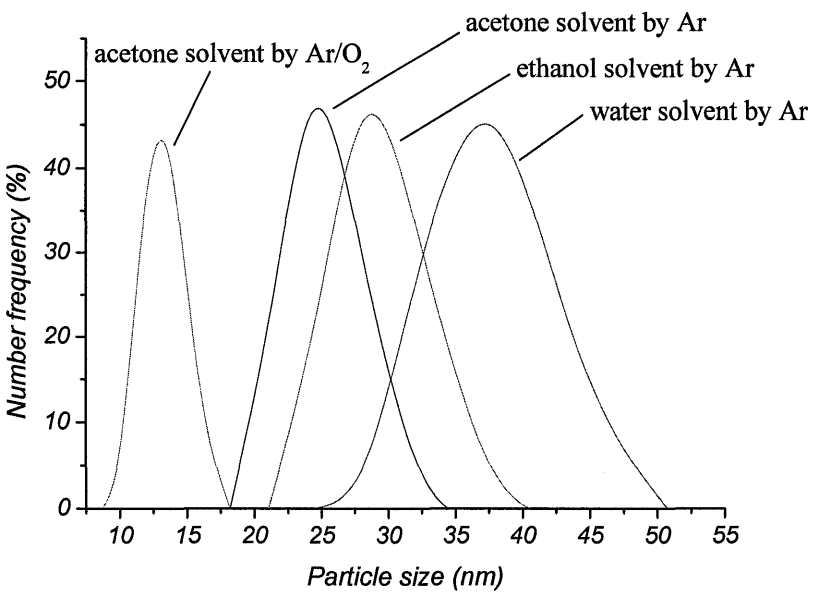

Fig. 4.23. Size distributions of Y_2O_3 C3 nanoparticles from SPS with various solvents and plasma gases

4.3.3 Combustion-aided SPS

As discussed above, the amorphous carbon and $Y_2O_2C_2$ compound resulted from the decomposition of the organic solvent and the consequent carbon impurity. Hence, complete combustion of the solvent by oxygen will effectively avoid the generation of these impurities. In this section, a novel spraying technique called combustion-aided SPS was applied for the first time, intended to avoid the generation of the impurity as well as to elevate the plasma enthalpy. O_2 was introduced in both the sheath and central plasma gas with Ar during acetone SPS to help the combustion of the solvent. As a result, the plasma plume became much brighter and more divergent than without combustion. XRD analysis of the as-sprayed particles (**Fig. 4.19**, (f)) and its refinement result reveal that the product is pure Y_2O_3 as a cubic phase. The organic solvent was completely combusted and there was no carbon-related impurity in the particles. The morphology of as-sprayed micron-sized particles is shown in **Fig. 4.24** (a). It can be seen that most particles are spherical, suggesting a much higher heat treatment level than Ar plasma. In addition, the productivity of C3 increased to 8.4 g/h. Judging from the TEM micrograph shown in **Fig. 4.24** (b) and the size distribution curve in **Fig. 4.23**, the mean size of the as-sprayed nanoparticles decreased further and the size distribution became narrower compared with those from Ar plasma spraying.

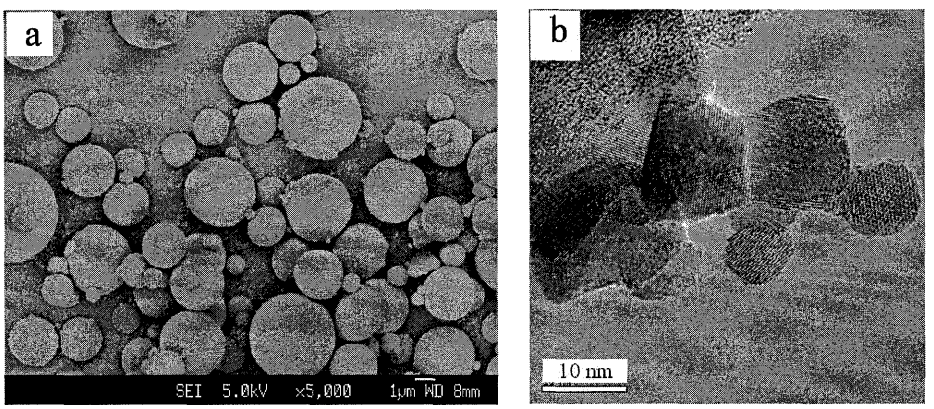

Fig. 4.24. As-sprayed Y_2O_3 particles from combustion-aided SPS. (a) micron-sized particles; (b) nanoparticles

4.4 Suspension feed spraying of R_2O_3 with various solvents by Ar and Ar/O_2 plasma

Since the combustion-aided SPS succeeded in impurity removal and enthalpy elevation for Y_2O_3, the method was extended to other rare earth oxides. In this section, four spraying schemes were adopted for each rare earth oxide: water SPS by Ar, water SPS by Ar/O_2, acetone SPS by Ar, and acetone SPS by Ar/O_2 (combustion-aided SPS). The results of C1 and C2 particles in comparison with those of powder feed spraying are discussed here.

4.4.1 Particle morphology

The morphology of Dy_2O_3 C1 particles from water SPS by Ar, water SPS by Ar/O_2, acetone SPS by Ar, and acetone SPS by Ar/O_2 are shown in **Fig. 4.25** (a), (b), (c), and (e), respectively. Judging by the proportion of spherical and irregular-shaped particles, water SPS with Ar had the lowest heat treatment level (**Fig. 4.25** (a)), followed by water SPS with O_2 (**Fig. 4.25** (b)) and acetone SPS with Ar (**Fig. 4.25** (c)), whereas acetone SPS with Ar/O_2 (i.e. combustion-aided SPS) exhibits a dramatic improvement in heat treatment and particle morphology (**Fig. 4.25** (e)). This situation is true for the other rare earth oxides too, as can be seen in **Fig. 4.24** (a) for Y_2O_3, and **Fig. 4.25** (d) and (f) for Sm_2O_3 and Lu_2O_3. Fig. **4.26** shows the SEM micrographs of R_2O_3 C2 particles from combustion-aided SPS. It can be seen that most of the C2 particles are in the nano size range. TEM analysis in **Fig. 4.27** reveals that nanoparticles below 50 nm are monocrystalline, in various shapes and well-dispersed. Their particles size distributions were measured by DLS and illustrated in Fig. **4.28**. The mean particle size decreases in the order of $Lu_2O_3 \rightarrow Y_2O_3 \rightarrow Dy_2O_3 \rightarrow Sm_2O_3$. Due to agglomeration effects, the smaller nanoparticles observed in TEM micrographs (**Fig. 4.27**) could not be identified by DLS.

In the case of Lu_2O_3, a small amount of micron-sized particles is present in SEM micrograph (**Fig. 4.26** (d)) and were not found in DLS either, because they were separated before measurement by ultrasonic vibration.

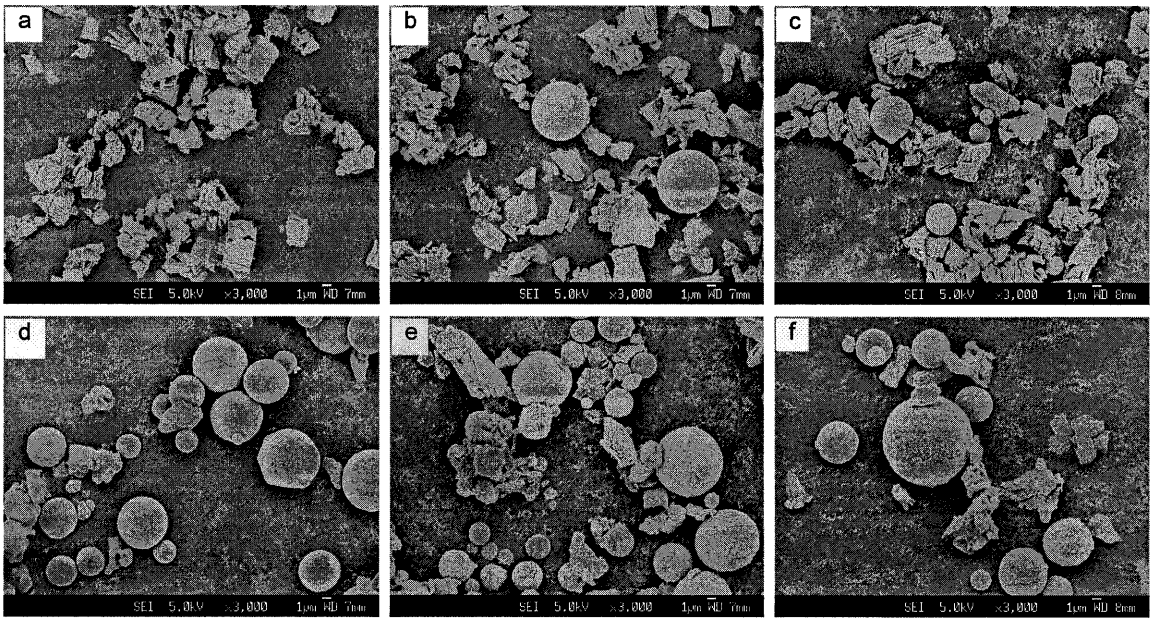

Fig. 4.25. SEM micrographs of R_2O_3 C1 particles from SPS. (a) Dy_2O_3 from water SPS by Ar; (b) Dy_2O_3 from water SPS by Ar/O_2; (c) Dy_2O_3 from acetone SPS by Ar; (d), (e), and (f): Sm_2O_3, Dy_2O_3, and Lu_2O_3 from acetone SPS by Ar/O_2, respectively

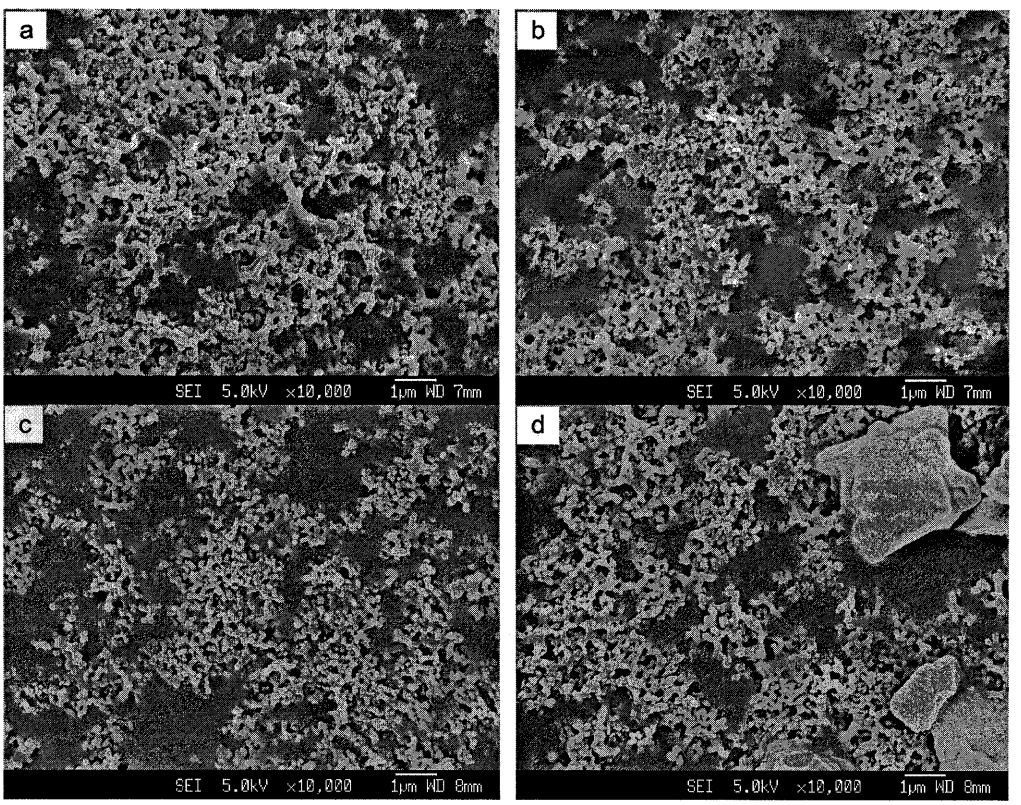

Fig. 4.26. SEM micrographs of R_2O_3 C2 nanoparticles from acetone SPS by Ar/O_2 plasma. (a) Y_2O_3; (b) Sm_2O_3; (c) Dy_2O_3; (d) Lu_2O_3

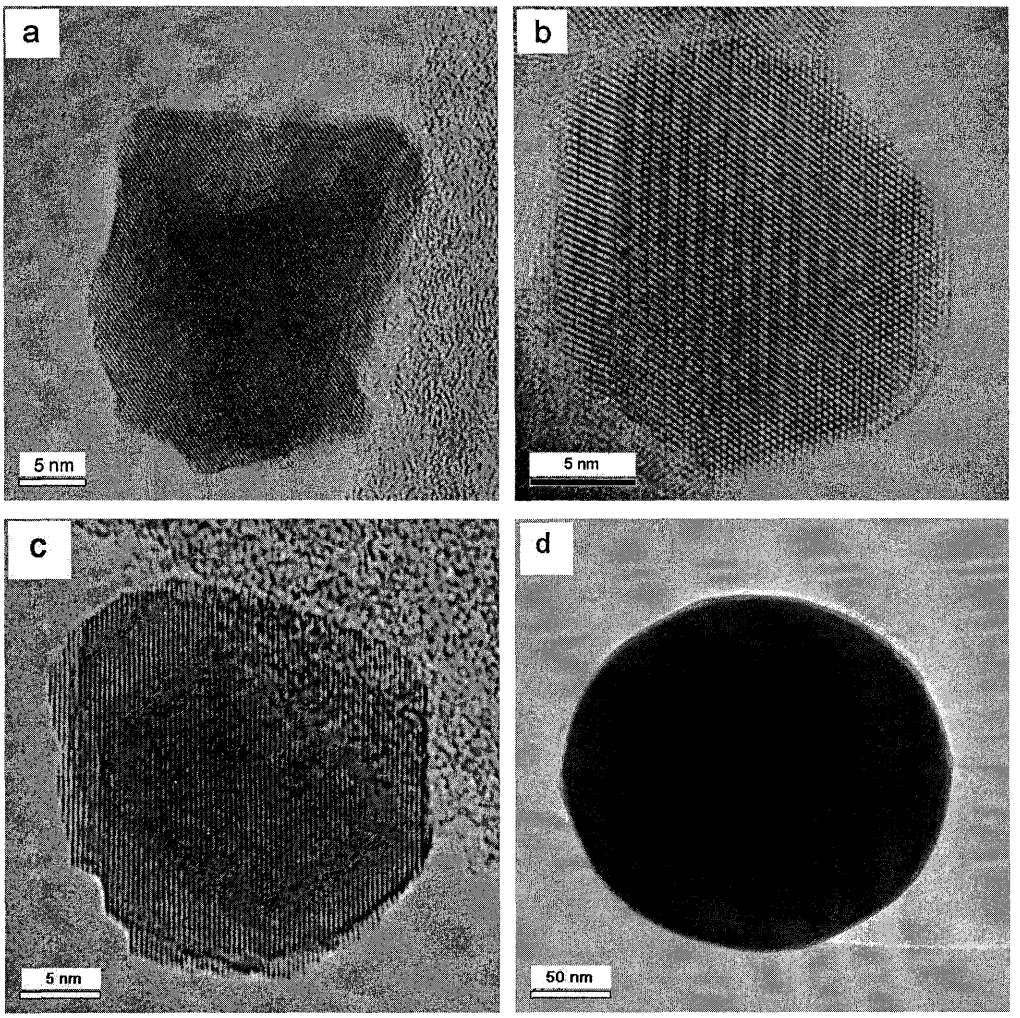

Fig. 4.27. TEM micrographs of R_2O_3 C2 nanoparticles from acetone SPS by Ar/O_2 plasma. (a) Y_2O_3; (b) Sm_2O_3; (c) Dy_2O_3; (d) Lu_2O_3

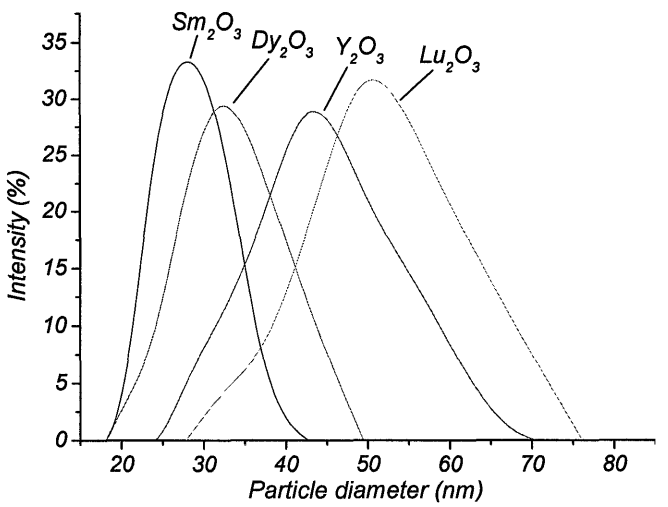

Fig. 4.28. Size distributions of R_2O_3 C2 nanoparticles from acetone SPS by Ar/O_2 plasma

4.4.2 Productivity

The productivities of R_2O_3 C2 particles from water and acetone SPS by Ar and Ar/O_2 plasma are illustrated in **Fig. 4.29**. Although the values may not be very accurate due to some loss in the system, it still can be seen that combustion-aided SPS has improved the productivity remarkably. The value almost doubles for all cases.

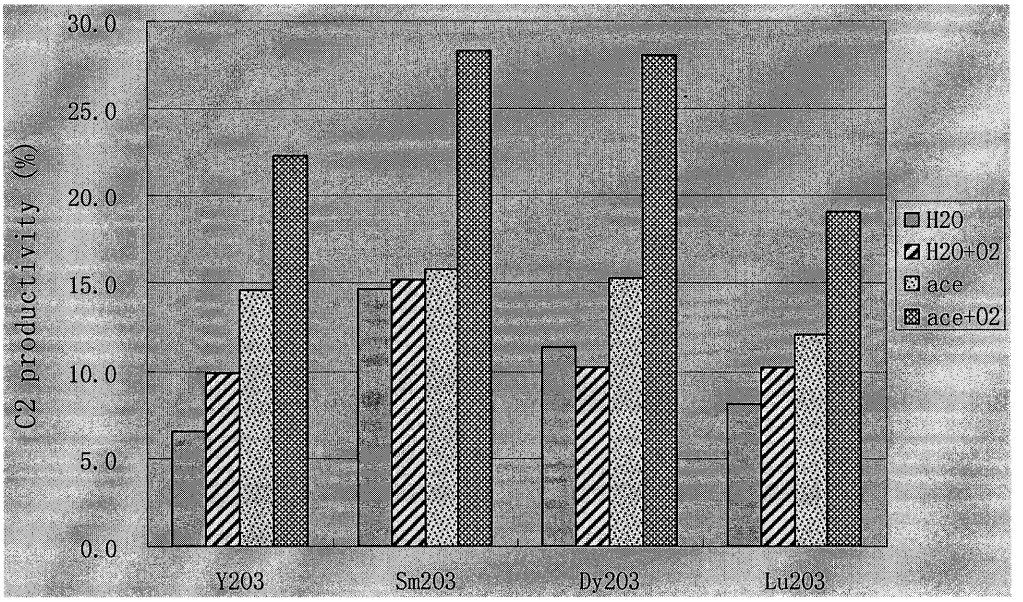

Fig. 4.29. Productivities of C2 particles from water and acetone SPS by Ar or Ar/O_2 plasma

4.4.3 Crystal structure

The influence of SPS on the crystal structure of R_2O_3 was studied by XRD and Rietveld refinement in comparison with that of powder feed spraying. Specifically, two factors were investigated for both C1 and C2 as-sprayed particles: phase composition and unit cell volume. To some extent, these two factors are associated with the plasma enthalpy. **Fig. 4.30, 4.31, 4.32**, and **4.33** illustrate the phase composition and unit cell volume of Y_2O_3, Sm_2O_3, Dy_2O_3 and Lu_2O_3 as-sprayed C1 and C2 particles respectively. From the analysis of the figures, a number of observations can be outlined.

(i) For the raw materials of the rare earth oxides studied, Y_2O_3, Dy_2O_3 and Lu_2O_3 had a pure cubic phase, while Sm_2O_3 raw material was mostly monoclinic.

(ii) All the oxides tended to transform from cubic (C-type) to monoclinic (B-type) structure after plasma treatment, but the degree of transformation varied with oxides and spraying conditions.

(iii) With the same spraying conditions, Dy_2O_3 had the highest degree of phase transformation degree (**Fig. 4.32**), while Y_2O_3 and Sm_2O_3 only transformed by a small extent (**Fig. 4.30** and **4.31**), and Lu_2O_3 did not even show transformation in C1 and C2 particles (**Fig. 4.33**).

(iv) As far as spraying conditions are concerned, basically, powder feed spraying gave a higher degree of phase transformation than SPS. For both powder and suspension spraying, the spraying with O_2 gas had a higher degree of phase transformation than without O_2. C2 particles had a higher degree of transformation than C1.

(v) As for the unit cell volumes, it appears that they had a correlation with the degree of phase transformation. In most cases, when the degree of phase transformation was high, the unit cell volumes of both cubic and monoclinic phase were smaller. Furthermore, the cell volume decreased remarkably by powder spraying with O_2 and combustion-aided SPS. However, there were also occasions that the phase composition relationship did not apply, e.g. the Lu_2O_3 case (**Fig. 4.33**).

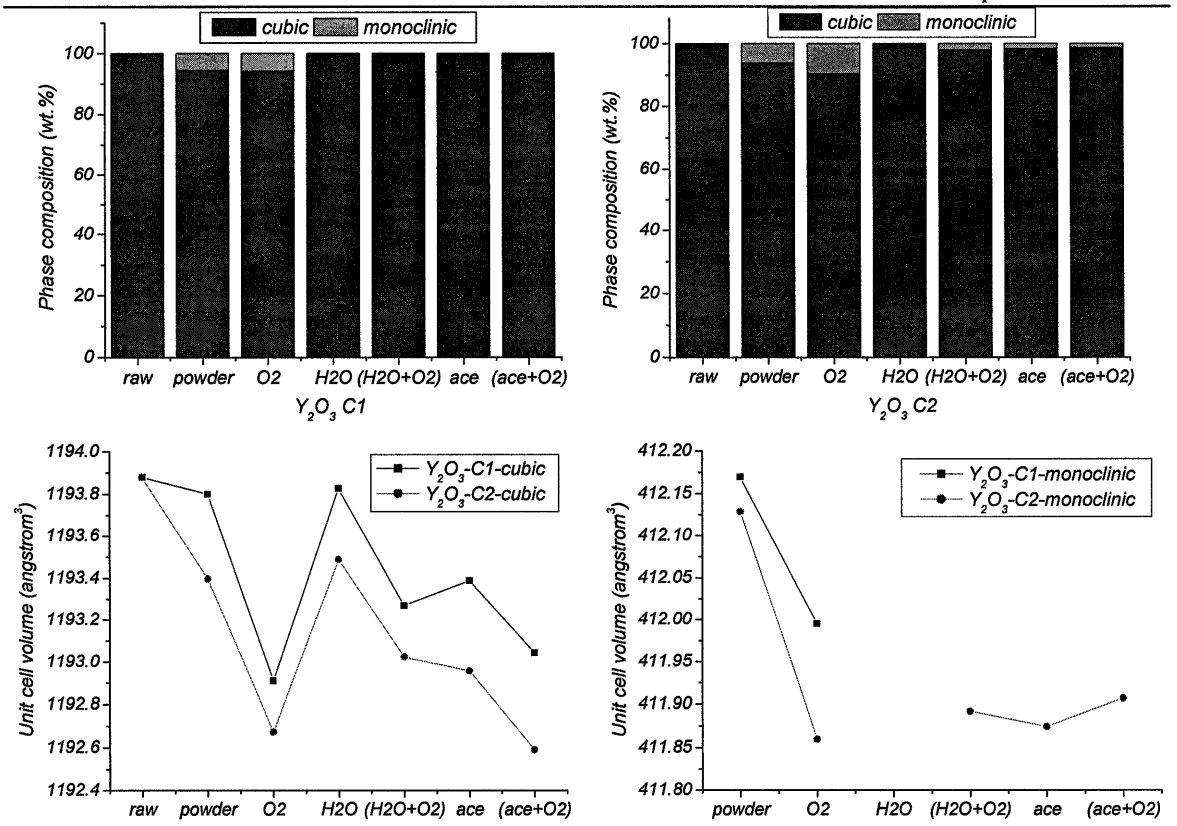

Fig. 4.30. Phase compositions and unit cell volumes of Y_2O_3 from various schemes. (raw: raw material; powder and O_2: powder spraying by Ar and Ar/O_2; H_2O, (H_2O+O_2), ace, and (ace+O_2): SPS with various solvents and gases)

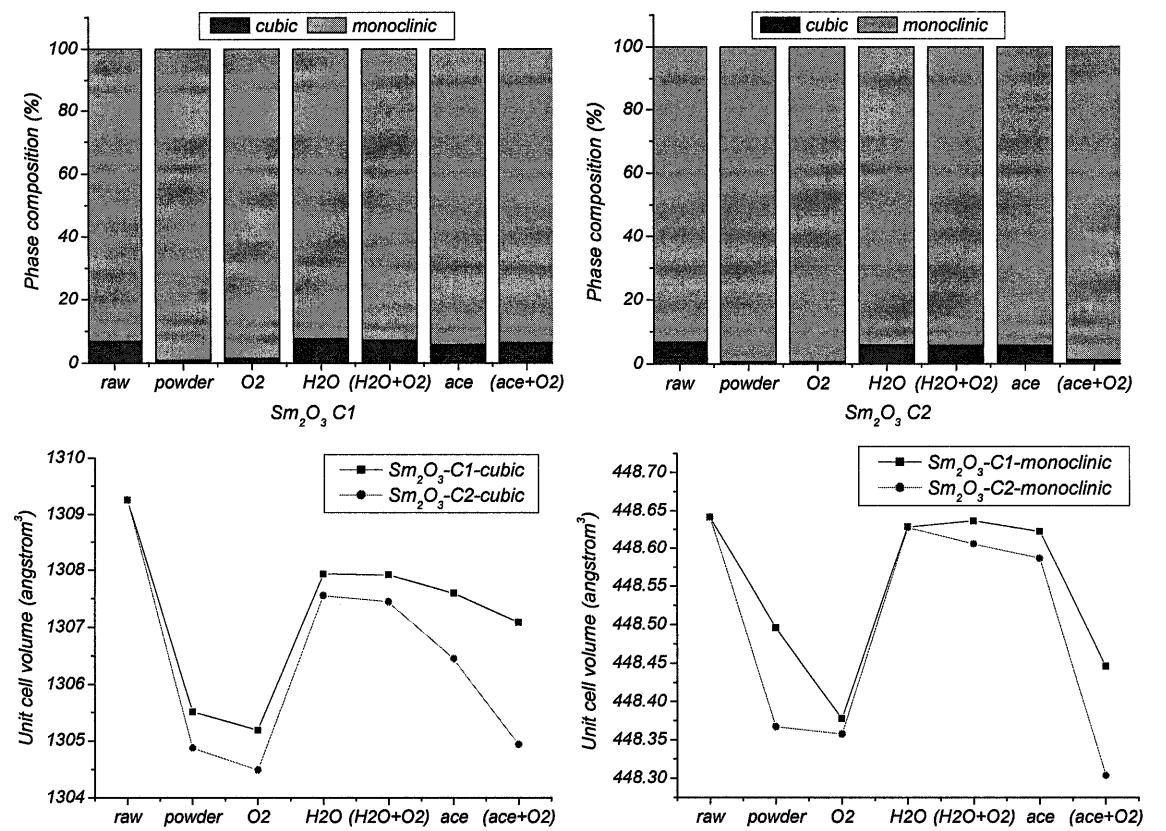

Fig. 4.31. Phase compositions and unit cell volumes of Sm_2O_3 from various schemes

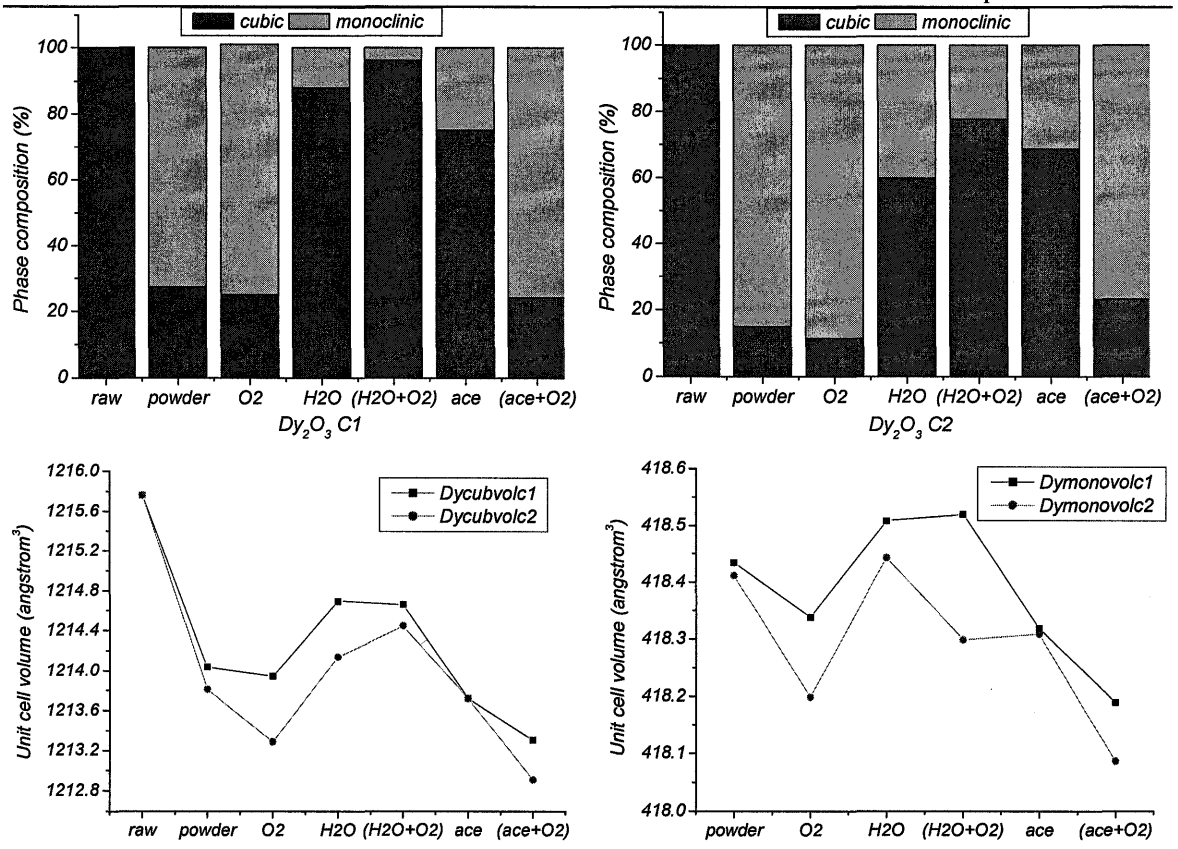

Fig. 4.32. Phase compositions and unit cell volumes of Dy_2O_3 from various schemes

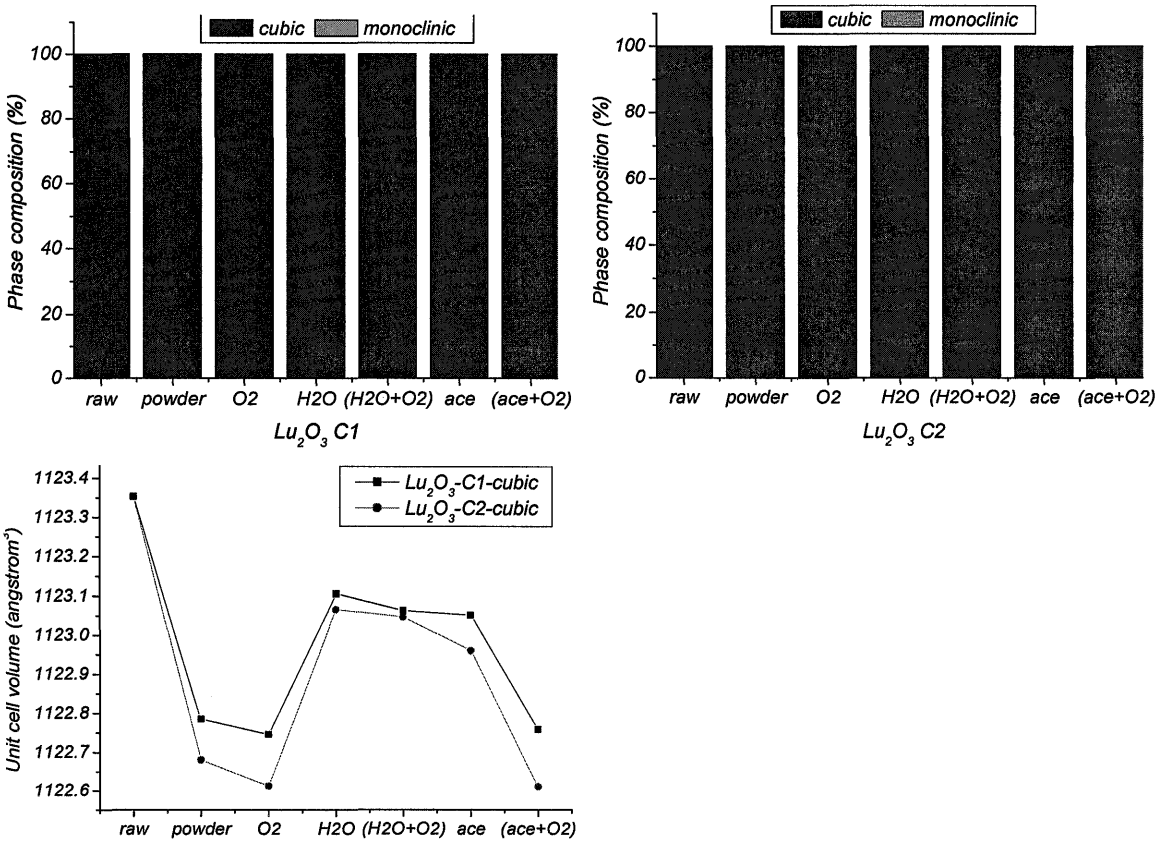

Fig. 4.33. Phase compositions and unit cell volumes of Lu_2O_3 from various schemes

4.5 Spraying synthesis of $Sm_{2-x}Lu_xO_3$ rare earth mixed oxide nanoparticles

To explore the synthesis of rare earth mixed oxide nanoparticles, Sm-Lu mixed oxides were synthesized using two approaches. In the first, the in-flight synthesis of mixed oxides nanoparticles was tried. A mixture of Sm_2O_3 and Lu_2O_3 with an atomic ratio of 1:1 was prepared by ball milling and then sprayed by Ar plasma. However, the mixture failed to combine into mixed oxide. In a second approach, the ball milled mixture of Sm_2O_3 and Lu_2O_3 was first pressed into pellets and sintered to form mixed oxide. Afterwards, the pellets were ground into powders and sprayed to synthesize nanoparticles.

4.5.1 Spraying synthesis of $Sm_{1.0}Lu_{1.0}O_3$ nanoparticles without pretreatment

The diffraction pattern of the as-sprayed Sm_2O_3 and Lu_2O_3 mixture particles with a ratio of Sm:Lu = 1:1 in the first approach is shown in **Fig. 4.34**, curve (b). In principle, it can be characterized as a superposition of the diffraction patterns of pure Sm_2O_3 and Lu_2O_3 (**Fig. 4.34**, curves (a) and (c)). Due to their low intensities, some small additional Bragg reflections which are not caused by contaminations remain, however, unexplained. Thus, it is concluded that besides a possible small fraction of solid solution phases, the sprayed mixture consists mainly of monoclinic Sm_2O_3 and cubic Lu_2O_3, which is confirmed by the evaluation of the corresponding unit cell parameters. This result implies that there was almost no reaction between the two rare earth oxides during spraying. Because of their high thermodynamic stability short residence time in the plasma plume, the partial pressures of the reactant vapors were too low for them to fully contact. Hence, the reaction was hard to carry out.

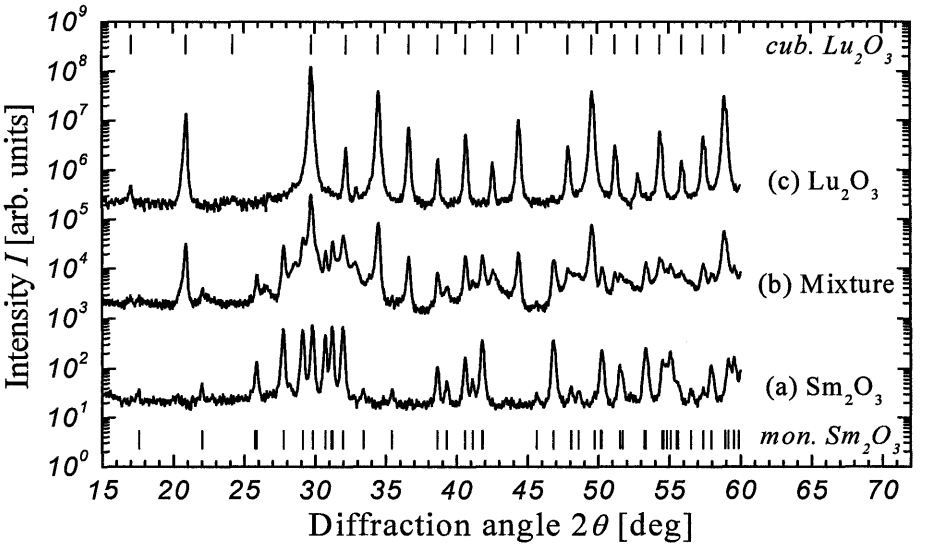

Fig. 4.34. XRD patterns of sprayed Sm_2O_3 (a), Lu_2O_3 (c), and their mixture (b) collected from chamber C2

4.5.2 Spraying synthesis of $Sm_{1.0}Lu_{1.0}O_3$ nanoparticles with pretreatment

In the alternative second approach, $Sm_{1.0}Lu_{1.0}O_3$ mixed oxide was first formed by sintering. The XRD pattern of the sintered pellet is shown in **Fig. 4.35**, curve (a). The material consists mainly of two phases, a monoclinic and a cubic one, in a mass ratio of 1:15. By Rietveld refinement, their lattice parameters were determined. In the case of the monoclinic phase, the associated unit cell volume is smaller compared to that one of sprayed monoclinic Sm_2O_3, and for the cubic phase, the unit cell volume is larger compared to that one of sprayed pure Lu_2O_3. Therefore, a mixture of two solid solution phases forms during sintering. This result is in accordance with the observations by Schneider and Roth [104], who reported the coexistence of a Sm-rich B type phase and a Lu-rich C type phase for Lu contents 44 at.% $< x_{Lu} <$ 54 at.% in the Sm_2O_3-Lu_2O_3 phase diagram. In the diffraction pattern of the pellet (**Fig. 4.35**, curve (a)), there are, however, additional Bragg reflections which cannot be assigned to any known phase of samarium or lutetium oxide. As these diffraction maxima disappear during grinding (**Fig. 4.35**, curve (b)), they are not associated with contamination in the sample, but might be due to

the formation of a metastable phase during sintering. As shown in **Fig. 4.36** (a), grinding the sintered pellets results in micron-sized particles with irregular shapes. The particles have a polycrystalline microstructure and consist of monoclinic B type and cubic C type phase solid solutions whose mass ratio was determined to be 1:6. Grinding does not lead to significant changes of the corresponding unit cell parameters (**Fig. 4.35**, curve (b)).

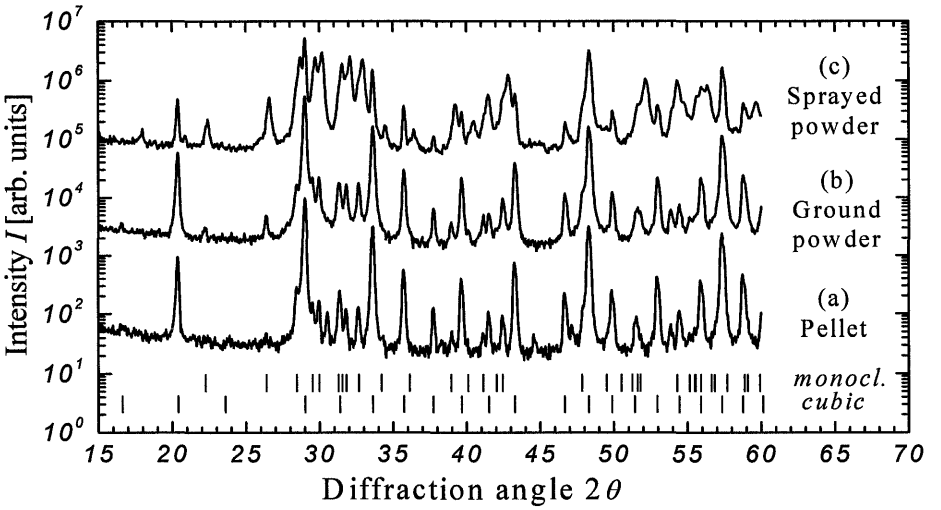

Fig. 4.35. XRD patterns of sintered $Sm_{1.0}Lu_{1.0}O_3$ pellet (a), its ground powder (b), and sprayed powder from chamber C2 (c)

After plasma processing of the ground material, the sprayed powders were separately collected in two chambers C1 and C2 as large and fine particles, respectively. The large particles of C1 had an almost spherical shape with diameters in the micron range. The smooth surface indicated a history of surface melting (**Fig. 4.36** (b)). The fine powder in chamber C2 consisted of both smaller micron-sized balls and nanoparticles. The latter ones are indicated in **Fig. 4.36** (c) as light-gray cloudy clusters. TEM results (**Fig. 4.37**) show that the nanoparticles are crystallites with size less than 100 nm and in various shapes. When the raw material is fed into the plasma plume, it experiences a flash melting, partial or complete evaporation, and subsequently is quenched at an extremely high rate when leaving the plume. While the melted particles form solid spheres, the vaporized material crystallizes into nanoparticles. To characterize the phase composition after

spraying, a diffraction pattern was recorded (**Fig. 4.35**, curve (c)) and analyzed. Besides the cubic C type phase and the monoclinic B type phase which are already present in the diffraction pattern after grinding (**Fig. 4.35**, curve (b)), the remaining Bragg reflections can be described with an additional monoclinic B type phase, having a smaller unit cell. Its appearance during spraying may be due to a partial transformation of the cubic phase. This assumption was confirmed by a decrease of the cubic phase content which is indicated by an intensity reduction of the corresponding Bragg reflections.

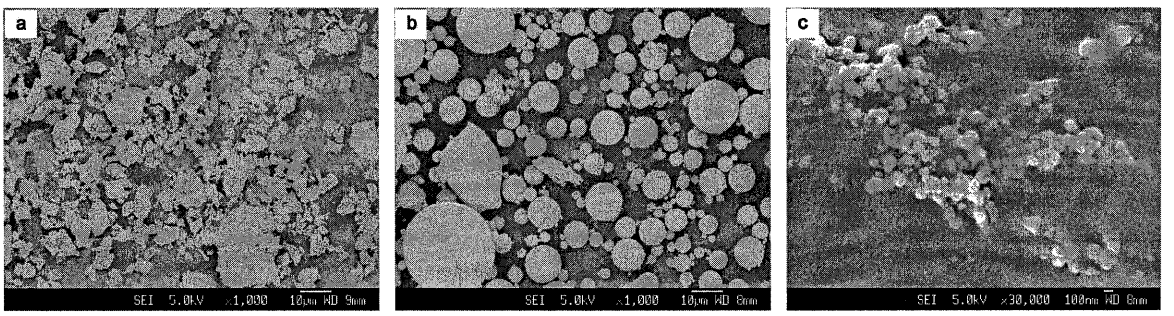

Fig. 4.36. SEM micrograph of $Sm_{1.0}Lu_{1.0}O_3$ ground powder from sintered pellets (a), as-sprayed C1 particles (b), and C2 particles (c)

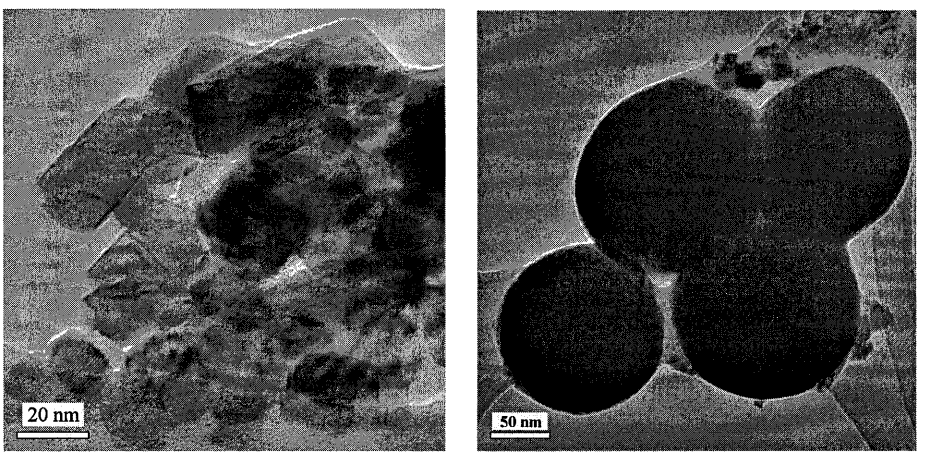

Fig. 4.37. TEM micrographs of $Sm_{1.0}Lu_{1.0}O_3$ nanoparticles from C2

4.5.3 Spraying synthesis of $Sm_{2-x}Lu_xO_3$ nanoparticles with pretreatment

The second approach (spraying with pretreatment) that succeeded in preparing $Sm_{1.0}Lu_{1.0}O_3$ nanoparticles was extended to the whole range of the $Sm_{2-x}Lu_xO_3$ (x = 0, 0.1,

0.2, 0.4, 0.6, 0.68, 0.8, 0.87, 1.0, 1.06, 1.2, 1.4, 1.6, 1.8, 2.0) mixed oxides series. The XRD patterns of sintered pellets, the corresponding ground powders, and their sprayed particles are shown in **Fig. 4.38**, **4.39**, and **4.40**. Their phase compositions and lattice parameters were determined by Rietveld refinement. Monoclinic Sm_2O_3 and cubic Lu_2O_3 structural information were used for the refinement of the patterns. The refined XRD pattern showed that in the sintered pellets pattern group, in addition to the B and C type solid solutions, three different metastable phases were present (**Fig. 4.38**), which disappeared after grinding of the pellets into powders (**Fig. 4.39**). For the ground powder group, according to the study of Schneider and Roth [104], the phase diagram of Sm_2O_3-Lu_2O_3 can be divided into three regions: Sm-rich, middle, and Lu-rich regions (**Fig. 4.41**, (a)). The Sm-rich region has a B-type monoclinic phase solid solution of Sm_2O_3 and Lu_2O_3. The Lu-rich region has a C-type cubic phase solid solution of Sm_2O_3 and Lu_2O_3. The middle region comprises both of these B and C solid solutions. However, in our study, it was found that the middle region shifts to the left and its range becomes wider (**Fig. 4.41**, (b)). In the sprayed powder group, the phase diagram is similar to that of ground powder, except that a new B-type monoclinic phase occurs in the middle region and Lu-rich regions (**Fig. 4.40 and 4.41**, (b)). This new B structure is probably the consequence of a C→B transformation induced by plasma treatment, after which the B structure is subsequently retained by the extremely high cooling rate. The new B structure is stable at ambient temperature, and shows no re-conversion to the C structure even at an annealing temperature of 400°C.

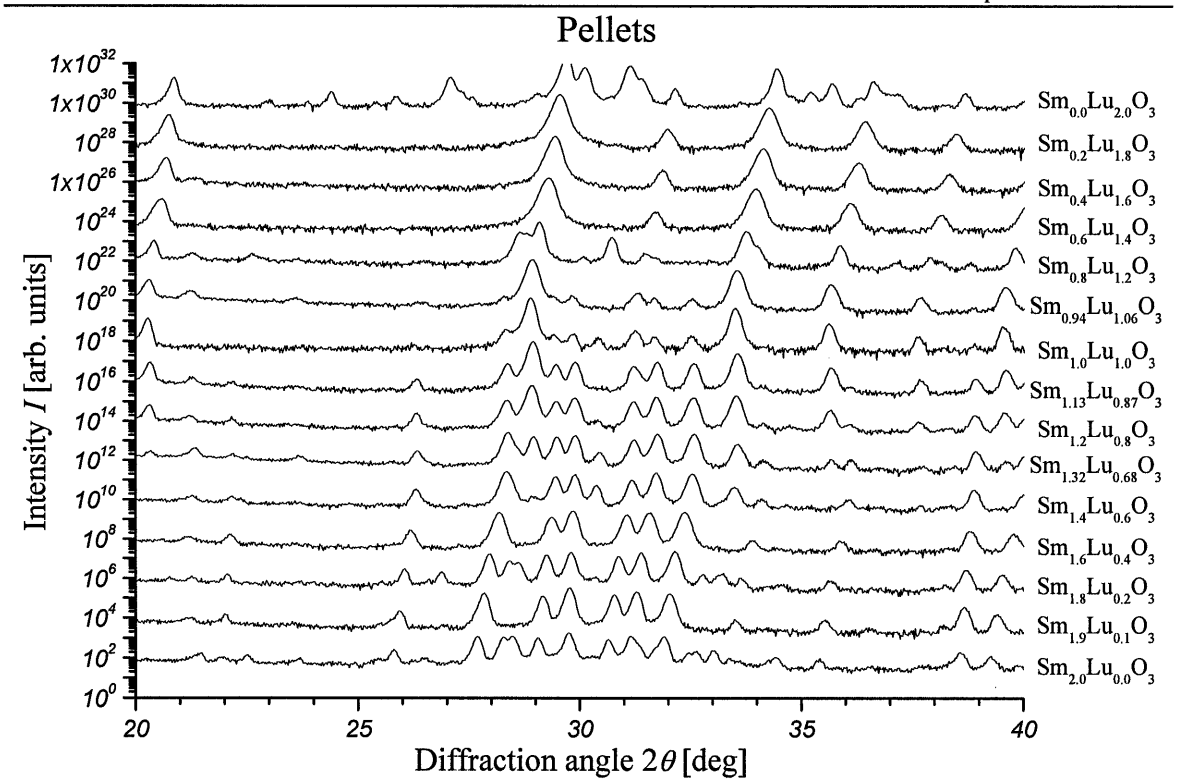

Fig. 4.38. XRD patterns of sintered pellets of $Sm_{2-x}Lu_xO_3$

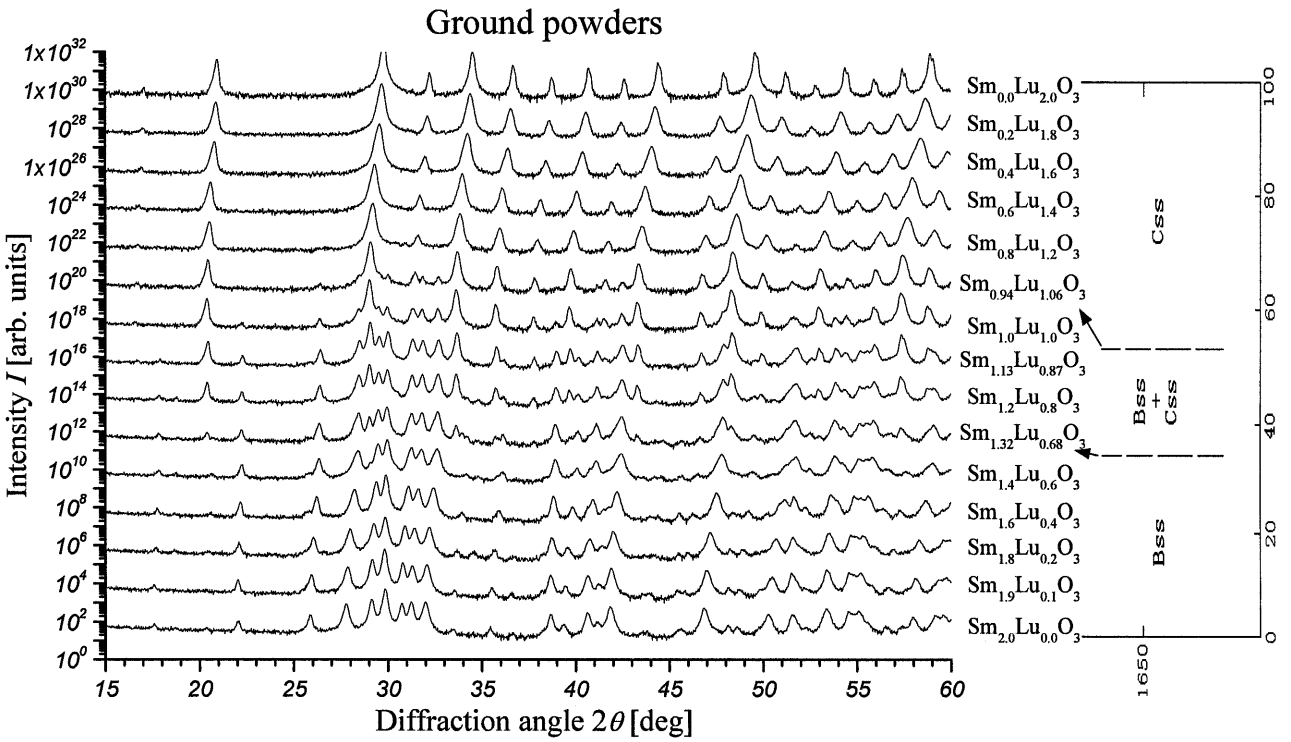

Fig. 4.39. XRD patterns of ground powders of sintered pellets of $Sm_{2-x}Lu_xO_3$

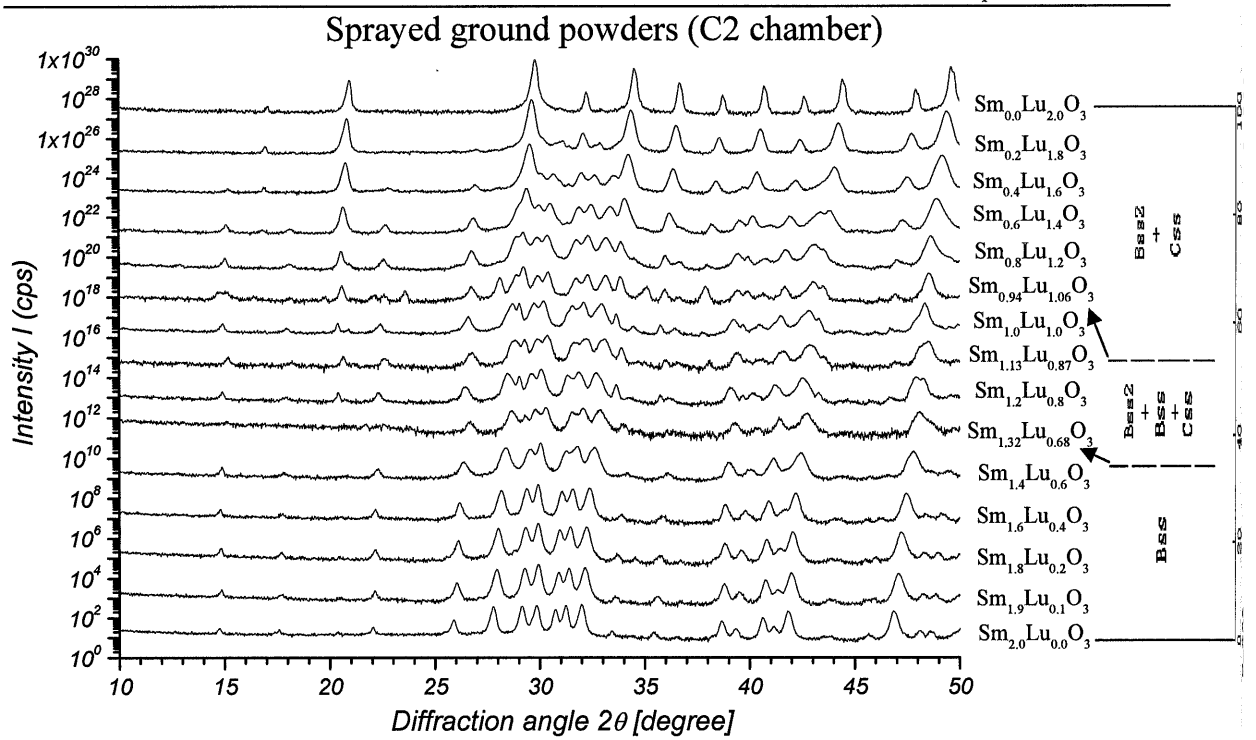

Fig. 4.40. XRD patterns of sprayed ground powders from C2 of $Sm_{2-x}Lu_xO_3$

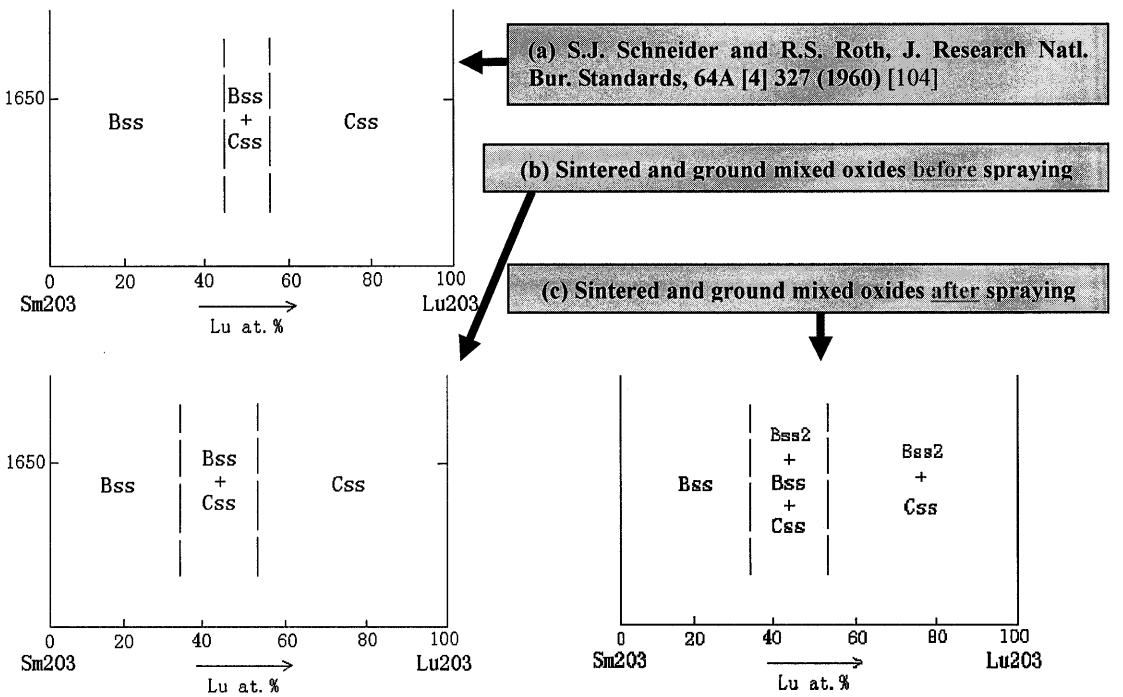

Fig. 4.41. Sm_2O_3-Lu_2O_3 binary phase diagrams

Chapter Five: Modeling of RF-ICP Spraying

To gain further understanding of the fundamentals of RF-ICP plasma spraying with Ar/O_2 and combustion-aided SPS, numerical models were developed using computational fluid dynamics (CFD) analysis program FLUENT V6.3.2©. The CFD code is a very powerful and cost-effective tool for representing the plasma heat generation and the plasma-material interactions. The approach in modeling the plasma heat generation was by means of the conventional constant volumetric heat source model. The plasma-material interactions such as energy and momentum transfer were considered to be one-way coupling. In the present modeling, to compare the behaviors of different spraying conditions and to investigate the subsequent effects on in-flight rare earth oxide particles, three spraying schemes were modeled: powder spraying by Ar plasma, powder spraying by Ar/O_2 plasma, and acetone SPS by Ar/O_2 plasma (combustion-aided SPS).

The simulation of RF-ICP spraying process involved two stages and was performed using commercial software FLUENT V6.3.2© (FLUENT Inc., 10 Cavendish Court, Lebanon, NH03766-1442). In the first stage, a steady state thermal fluid solution for plasma and carrier gas flow without particle injection was obtained. In the second stage, rare earth oxide particles were introduced through injector as solid entities, and the heat and momentum transfer from plasma to particles were calculated so as to obtain the in-flight particle properties (temperature, velocity, size, and number concentration). The plasma and particle interaction was considered one-directional, i.e. the process of energy and momentum transfer only proceeded from the plasma to particles but not in reverse. This will greatly simplify the computational task, but may also result in deviation from the realistic conditions since the particles act as local heat sinks and reduce the local plasma

temperature and velocity [86]. Nevertheless, in our spraying, the particle flow was set to very dilute (1 g/min) with the purpose of minimizing the influence of particles on plasma [87]. As a result, the energy and momentum the plasma received from or transferred to the particles would not be sufficient to alter the plasma temperature and velocity.

5.1 Plasma heat generation

The mathematical model in FLUENT V6.3.2© was built based on the Navier-Stokes equations and Reynolds method of averaging the time dependent equations, coupled with standard κ-ε model for turbulence representation. With the appropriate boundary conditions, the governing equations were solved using an iterative finite volume method.

5.1.1 Model geometry

The geometry of the models was developed using the commercial software GAMBIT V2.3.16© (FLUENT Inc., 10 Cavendish Court, Lebanon, NH03766-1442.), as shown schematically in **Fig. 5.1**. The cylindrical computational domain included the RF-ICP torch (diameter×length) Φ35×109 mm and part of the free space of the chamber underneath the torch exit Φ266×500 mm. (Dimensions were taken from the manual of 35 kW TEKNA Plasma System with PL-35 induction RF plasma torch.)

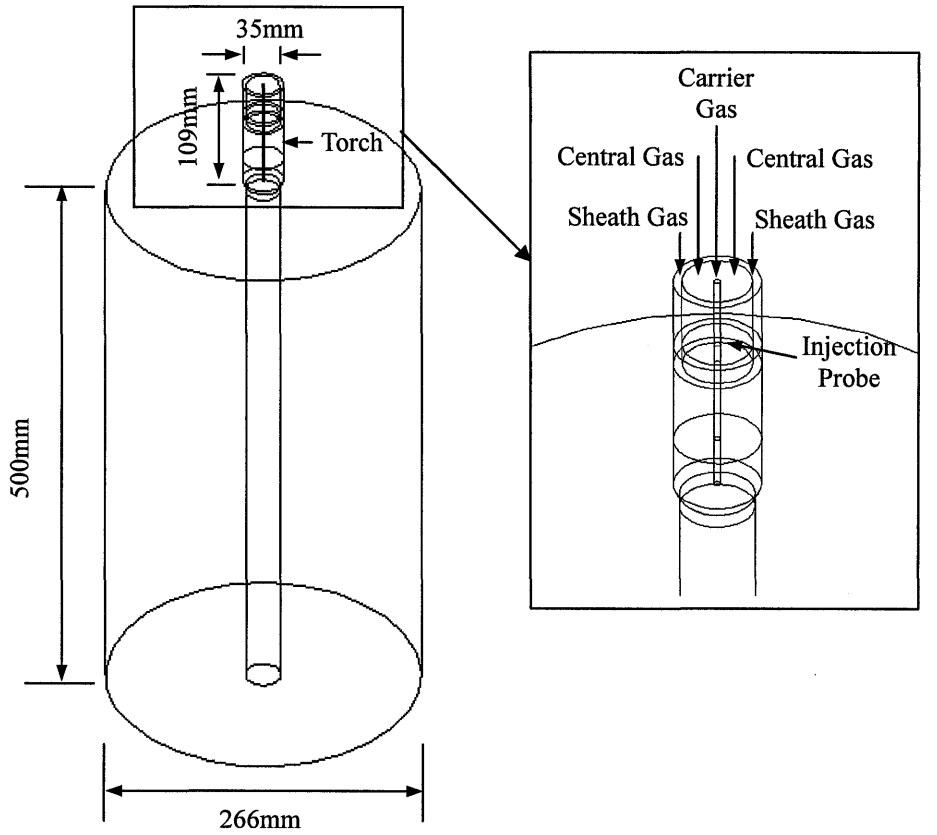

Fig. 5.1. Modeling geometry for inductively coupled radio frequency plasma spraying (RF-ICP). On the right gives the enlarged view of the torch, showing the injection of carrier gas, central gas and sheath gas

5.1.2 Modeling assumptions

The modeling of the free turbulent steady state RF-ICP flow was based on the following assumptions:

(i) The plasma gas was assumed to be in local thermodynamic equilibrium (LTE), so that the plasma could be considered as a continuous fluid with only a single value of properties such as density and viscosity.

(ii) In order to simplify the modeling, plasma characteristics were not modeled. Therefore, Lorentz flow (flow induced due to the potential differences in electric and magnetic fields) was neglected in this analysis. The plasma heat was assumed to be generated by volumetric heat source which was determined by power input and torch efficiency. (Calculation example in **Appendix I**)

(iii) The plasma gases have temperature dependent thermodynamic and transport properties. The properties of Ar and O_2 plasma gases were taken from [105] and input as a piecewise linear profile in FLUENT©.

(iv) Oxygen molecules were assumed to be completely dissociated in the torch and recombined in the chamber. The ionization process of O atoms was ignored. The reason is twofold. Firstly, the O atom has a much higher ionization energy compared to O_2 dissociation, and only a small number of the O atoms can be ionized. The number density of O^+ in the plasma was two orders lower than O [80], thus, the influence of ionization was negligible. Secondly, it was hard to determine the ionization rate as it varies with plasma conditions, and there was no previous research relevant to our spraying.

(v) The plasma flow was assumed to be optically thin and no radiation was taken into consideration. This can be justified according to reference [106] that the heating of particles by gas radiation was negligible compared to convective heat transfer.

(vi) The plasma flow was considered as incompressible both inside the plasma torch and inside the chamber. It is assumed that no swirl was present in the plasma heat generation since the plasma gas was injected axially into the center of the torch.

(vii) In order to determine the significance of buoyancy force, Gr/Re_∞^2 (ratio of Grashof number to Reynolds number squared) was evaluated. The value was approximately 10^{-5}. This means that inertia was the dominant force for flow acceleration in comparison with the buoyancy force. Therefore, operation of the torch was assumed to be in the steady state with negligible gravity effect.

5.1.3 Governing equations

Based on the above assumptions, there are five governing equations of fluid flow

representing mathematical statements of the conservation laws of physics, conservation of chemical species, and turbulence [95].

5.1.3.1 Mass conservation equation

The mass conservation equation is the reflection of the continuum assumption. The physical meaning of this equation is that the fluid will occupy continuously every point of the space in the flow domain. Eq. (5-1) indicates the steady state of mass continuity equation.

$$\frac{\partial}{\partial x_i}(\rho u_i) = 0 \tag{5-1}$$

where ρ is the density and u is the velocity of the flow.

5.1.3.2 Momentum conservation equation

The momentum conservation equation links the flow velocity of a fluid element with surface forces acting on it. It can be written in Cartesian tensor form as follows,

$$\frac{\partial}{\partial x_j}(\rho u_i u_j) = -\frac{\partial p}{\partial x_i} + \frac{\partial}{\partial x_j}\left[\mu\left(\frac{\partial u_i}{\partial x_j} + \frac{\partial u_j}{\partial x_i} - \frac{2}{3}\delta_{ij}\frac{\partial u_k}{\partial x_k}\right)\right] + \frac{\partial}{\partial x_j}(-\rho\overline{u_i' u_j'}) \tag{5-2}$$

where p is the pressure, μ is the dynamic viscosity. The suffixes i, j, and k indicate the three directions of Cartesian coordinates. δ_{ij} is given by δ_{ij} =1 if i=j and δ_{ij} =0 if i≠j. The additional term due to Reynolds stresses, $-\rho\overline{u_i' u_j'}$ represents the effects of turbulence, where u' is the turbulence velocity. A common expression of the relation between Reynolds stresses and mean velocity gradients is Eq. (5-3), where k is the thermal conductivity and μ_t is the turbulent viscocity.

$$-\rho\overline{u_i' u_j'} = \mu_t\left(\frac{\partial u_i}{\partial x_j} + \frac{\partial u_j}{\partial x_i}\right) - \frac{2}{3}(\rho k + \mu_t\frac{\partial u_i}{\partial x_j})\delta_{ij} \tag{5-3}$$

5.1.3.3 Standard κ-ε equation

The state of a flow can be determined by the value of its Reynolds number *Re*. When *Re* > 2400, the flow is turbulent. The RF-ICP flow is turbulent and the standard κ-ε turbulence model can be applied since local turbulence kinetic energy is necessary for determination of the turbulent dispersion of particles in the particle dynamics and heat transfer formulation. The standard κ-ε equations are shown in Eq. (5-4) and (5-5).

$$\frac{\partial}{\partial x_i}(\rho u_i \kappa) = \frac{\partial}{\partial x_i}[(\mu + \frac{\mu_t}{\mathrm{Pr}_{t,\kappa}})\frac{\partial \kappa}{\partial x_i}] + 2\mu_t S_{ij} S_{ij} - \rho\varepsilon \qquad (5\text{-}4)$$

$$\frac{\partial}{\partial x_i}(\rho u_i \varepsilon) = \frac{\partial}{\partial x_i}[(\mu + \frac{\mu_t}{\mathrm{Pr}_{t,\varepsilon}})\frac{\partial \varepsilon}{\partial x_i}] + C_{1\varepsilon}\frac{\varepsilon}{\kappa}2\mu_t S_{ij} S_{ij} - C_{2\varepsilon}\rho\frac{\varepsilon^2}{\kappa} \qquad (5\text{-}5)$$

where $S_{ij} = \frac{1}{2}\left[\frac{\partial u_i}{\partial x_j} + \frac{\partial u_j}{\partial x_i}\right]$, $\mu_t = \rho C_\mu \frac{\kappa^2}{\varepsilon}$. The last two terms in the equations represent the rate of production and destruction of κ and ε, respectively. The five adjustable constants are set as $C_\mu = 0.09$; $\mathrm{Pr}_{t,\kappa} = 1.00$; $\mathrm{Pr}_{t,\varepsilon} = 1.30$; $C_{1\varepsilon} = 1.44$; $C_{2\varepsilon} = 1.92$.

5.1.3.4 Energy equation

The variation of plasma temperature is determined by the transport equation for energy as in Eq. (5-6).

$$\frac{\partial}{\partial x_i}[u_i(\rho E + p)] = \frac{\partial}{\partial x_j}[k_{eff}\frac{\partial T}{\partial x_j} - \sum_n h_n J_n + u_i(\tau_{ij})_{eff}] + S_h \qquad (5\text{-}6)$$

where $E = h - \frac{p}{\rho} + \frac{u^2}{2}$

$h = \sum_n Y_n H_n + \frac{p}{\rho}$ for incompressible flow

$h_n = \int_{T_{ref}}^{T} C_{pn} dT$

$$(\tau_{ij})_{eff} = (\mu + \mu_t)(\frac{\partial u_j}{\partial x_i} + \frac{\partial u_i}{\partial x_j}) - \frac{2}{3}(\mu + \mu_t)(\frac{\partial u_i}{\partial x_j})\delta_{ij}$$

$$k_{eff} = k + \frac{C_p \mu_t}{\mathrm{Pr}_t}$$

The first three terms on the right-hand side represent energy transfers due to conduction, species diffusion, and viscous dissipation, respectively. S_h is the source term accounting for the heat of chemical reaction or any other heat source. J_n is the diffusion flux, Y_n is the mass fraction of species n and T_{ref} is 298.15 K. In this study, the volumetric heat source from the inductively coupled RF powder is defined in Eq. (5-7) and included as the source term, S_h in the energy governing equation.

$$S_h = P'''_{in} = \frac{\eta_t EI}{V} \tag{5-7}$$

where P''' is the volume-averaged heat source, EI the input plasma power, and V the volume of the torch. Torch efficiency, η_t, which results mainly from the heat loss through the cooling water in the plasma torch and injector, is set to 67% after the technical report of TEKNA Plasma Systems Inc (http://www.tekna.com/).

5.1.3.5 Species equation

There were two kinds of gas involved in this spraying, Ar and O_2. To solve the conservation equation for chemical species, FLUENT© predicts the local mass fraction of each species, Y_n through the solution of a convection-diffusion equation for the n^{th} species as in Eq. (5-8)

$$\frac{\partial}{\partial x_i}(\rho u_i Y_n) = \frac{\partial}{\partial x_i}(\rho D_n + \frac{\mu_t}{Sc_t})\frac{\partial Y_n}{\partial x_i} \tag{5-8}$$

where D_n is the diffusion coefficient for species n in the mixture and Sc_t is the turbulent Schmidt number defined as $Sc_t = \frac{\mu_t}{\rho D_{nt}}$, where μ_t is the turbulent viscosity and D_{nt} is the

turbulent diffusivity.

5.1.4 Representation of oxygen recombination and acetone combustion

The general modeling governing equations and procedure discussed above is only applicable to the Ar plasma case. In the Ar/O_2 plasma and combustion-aided SPS cases, dissociation process of oxygen molecules that happened inside the torch absorbed a large amount of heat from the plasma field, which would otherwise dissipate mainly through water-cooling of the torch and injector. This additional heat was released through the subsequent recombination of oxygen atoms that took place in the free space underneath the torch exit, with an effect of elevating remarkably the enthalpy there. Hence, the oxygen gas literally increased the torch efficiency by carrying more heat to the free space below the torch exit where the particles were heat-treated.

One way to represent the oxygen dissociation and recombination and the acetone combustion is to increase the torch efficiency and energy source. However, in FLUENT©, a simpler way can be used by considering these processes as chemical reactions and applying the eddy dissipation model. The eddy dissipation model is a turbulence-chemistry interaction model based on the work of Magnussen and Hjertager [107]. The model assumes that reaction rates are controlled by the turbulence, so that the computationally expensive Arrhenius chemical kinetic calculations can be avoided. This is reasonable for oxygen dissociation and recombination and acetone combustion cases because their processes are instantaneous and the overall rate of the reaction is controlled by relatively slow turbulent mixing. For this reason, the reactions are said to be mixing-limited, and the complex, and often unknown, chemical kinetic rates can be safely neglected. The mixing and transport of chemical species can be modeled by solving

conservation equations describing the convection, diffusion, and reaction source for each component species. In practice, it was assumed that O_2 absorbed heat and dissociated totally once fed into the torch, and subsequently the resulting O atoms completely recombined in the chamber and released the heat. The released heat was accounted for by the source term S_h in energy equation, and the O recombination reaction was represented by adding an additional source term R_i in the species transport equations. Therefore, the species transport equation was modified as in Eq. (5-9),

$$\frac{\partial}{\partial x_i}(\rho u_i Y_n) = \frac{\partial}{\partial x_i}(\rho D_n + \frac{\mu_t}{Sc_t})\frac{\partial Y_n}{\partial x_i} + R_i + S_i \qquad (5\text{-}9)$$

where R_i is the net rate of production of species i by chemical reaction and S_i is the rate of creation by addition from the dispersed phase, plus any other sources. The net rate of production of species i due to reaction r, $R_{i,r}$, is given by the smaller of the two expressions below,

$$R_{i,r} = v'_{i,r} M_{w,i} A\rho \frac{\varepsilon}{k} \min_R (\frac{Y_R}{v'_{R,r} M_{w,R}}) \qquad (5\text{-}10)$$

$$R_{i,r} = v'_{i,r} M_{w,i} AB\rho \frac{\varepsilon}{k} (\frac{\sum_P Y_P}{\sum_j^N v''_{j,r} M_{w,j}}) \qquad (5\text{-}11)$$

These are species production rate equations based on the work of Magnussen and Hjertager [107], where $v'_{i,r}$ and $v''_{j,r}$ are the stoichiometric coefficient for reactant i and product j in reaction r, respectively; M_w is the molecular weight of species; Y_P is the mass fraction of any product species, P; Y_R is the mass fraction of a particular reactant, R; A and B are empirical constants equal to 4.0 and 0.5 respectively.

For the combustion-aided SPS case, besides oxygen recombination, the acetone solvent combustion reaction also needs to be accounted for. Fortunately, in FLUENT©, multiple simultaneous chemical reactions can also be modeled, which enables the incorporation of

both oxygen recombination and acetone combustion in the model. Therefore, the acetone combustion can be represented in the same way as that for oxygen recombination by Eq. (5-9).

5.1.5 Wall functions

The mean velocity of the free turbulent plasma flow is at a maximum far away from the wall and sharply decreases in the near-wall region. High values of velocity fluctuations are found adjacent to the wall where the large mean velocity gradients ensure that turbulence production is high. To have an accurate representation of the flow in the near-wall region, semi-empirical formulas called wall functions were used to link the viscosity-affected region with the wall and the fully turbulent region. Equations (5-12) and (5-13) show that the flow close to the wall is influenced by viscous effects and does not depend on free stream parameters. The plasma velocity at an adjacent element to the wall, U_A strongly depends on the distance, y from the wall, plasma density, ρ and viscosity, μ and the wall shear stress, τ_w [108]. Equations (5-12) and (5-13) are called the law-of-the-wall for mean velocity and were used as the wall functions [109].

$$U^* = y^*, \quad y^* < 11.225 \tag{5-12}$$

$$U^* = \frac{1}{K} \ln (By^*), \quad y^* > 11.225 \tag{5-13}$$

where U^* and y^* are the dimensionless velocity and distance from the element to the wall, K is the von Kármán constant (= 0.42), B the empirical constant (= 9.81). U^* and y^* are defined as:

$$U^* = \frac{U_A C_\mu^{1/4} \kappa_A^{1/2}}{\tau_w / \rho} \tag{5-14}$$

$$y^* = \frac{\rho C_\mu^{1/4} \kappa_A^{1/2} y_A}{\mu} \tag{5-15}$$

where C_μ is the empirical constant (= 0.09), κ_A is the turbulent kinetic energy at point A (near-wall element) and y_A is the distance from point A to the wall.

Reynolds' analogy between momentum and energy transport gives a similar logarithmic law for temperature [110]. As in the law-of-the-wall for mean velocity, the law-of-the-wall for temperature employed in FLUENT© comprises the following two different laws:

(i) Equation (5-16) is the linear law for the thermal conduction sublayer where conduction is important [109].

(ii) Equation (5-17) is the logarithmic law for the turbulent region where effects of turbulence dominate conduction [109].

$$\frac{(T_w - T_A)\rho C_p C_\mu^{1/4} \kappa_A^{1/2}}{\dot{q}} = Pr\, y^*, \quad y^* < y_T^* \tag{5-16}$$

$$\frac{(T_w - T_A)\rho C_p C_\mu^{1/4} \kappa_A^{1/2}}{\dot{q}} = Pr_t \left[\frac{1}{K} \ln (By^*) + P\right], \quad y^* > y_T^* \tag{5-17}$$

where T_A is the plasma temperature at an adjacent element to the wall, T_w is the wall temperature, C_p is the plasma specific heat capacity, $\dot{q}$ is the heat flux to the wall, y_T^* is the non-dimensional thermal sublayer thickness and Pr_t is the Prandtl number: $Pr_t = \upsilon_t / \alpha_t$. P was computed using the formula given in Eq. (5-18) by [111].

$$P = 9.24 \left[\left(\frac{Pr}{Pr_t}\right)^{3/4} - 1\right](1 + 0.28\, e^{-0.007\, Pr/Pr_t}) \tag{5-18}$$

5.1.6 Operating and boundary conditions

Three spraying schemes were modeled: powder spraying by Ar, powder spraying by Ar/O_2, and acetone SPS by Ar/O_2 (combustion-aided SPS). Their operating conditions are listed in Section 3.3 and **Table 5.1**. The torch efficiency was 67% for Ar RF-ICP according to TEKNA technical report. For Ar/O_2 and (Ar/O_2+acetone) cases, since the additional energy from oxygen recombination and acetone combustion was represented by the source term in the energy governing equations, their torch efficiencies for heat source calculation were still set to 67%. The plasma gas and carrier gas were both input along the centerline of the torch. The axial exit boundaries were selected a distance far away from the exit of the torch such that atmospheric boundary conditions were applied there. The boundary conditions for the turbulence model at inlets of the torch and injector were turbulence intensity and characteristic length. The turbulence intensities at central, sheath, and carrier gas inlets were calculated based on Eq. (5-19) as:

$$T_i = 0.16\,(Re_{HD})^{-0.125} \tag{5-19}$$

where Re_{HD} is the Reynolds number calculated for the gas flowing through the respective inlets, on the basis of the hydraulic diameter as the characteristic length. O_2 sink and O source were calculated from the O_2 gas flowrate with the assumption that oxygen was 100% dissociated and recombined.

Table 5.1. Operating conditions for plasma spraying simulation

Operating condition/unit	Ar	Ar/O_2	(Ar/O_2+acetone)
Torch diameter / mm	35	35	35
Nozzle diameter / mm	1	1	1
Torch exit diameter / mm	30	30	30
Powder size / μm	1-20	1-20	1-20
Power / kW	22	22	22
Torch efficiency / %	67	67	67
Heat source / W/m^3	4.164901E+08	4.164901E+08	4.164901E+08
Turbulence intensity-central gas / %	5.70	6.06	6.21
Turbulence intensity-sheath gas / %	6.62	7.03	7.03
Turbulence intensity-carrier gas / %	5.74	5.74	8.07
O_2 sink / kg/m^3s	0	-51.4414	-14.3108
O source / kg/m^3s	0	102.8829	28.6215

5.1.7 Solution scheme

The five governing equations of mass, momentum, turbulence, energy, and species were solved by the FLUENT V6.3.2© commercial package using the control volume technique. This technique converts governing equations into algebraic equations that can be solved numerically. This numerical approach stores scalar variables at the center of the control volume. The face values of scalar variables are also required for the convection terms and their values are obtained from interpolation. First order upwind scheme was used to calculate the face values of the scalar variables as the problem was convection-dominated flow. For pressure and velocity coupling, the SIMPLE algorithm was employed [68, 95]. As for the solution algorithm, the segregated solver was selected. The segregated solution strategy is to solve each single variable field by taking into account all control volumes at the same time, followed by solving next field variable in the same way and so on [109].

5.2 Particle dynamics and heat transfer formulation

After attaining the converged solution for the RF-ICP field, Y_2O_3 particles were injected through the injector and their motion and thermal evolution were calculated within the computational domain for the three cases. The particles were modeled in FLUENT as discrete Lagrangian entities that received momentum and energy from the plasma in one-directional coupling. Particle in-flight behavior, e.g. particle velocities and particle temperatures, were predicted based on the Newton second law of motion and the energy balance equation, respectively.

In the particle dynamics formulation, particle vaporization and formation of nanoparticles were not modeled because of the software limitation and computational difficulty. Only micron-sized particles were considered and their shapes were considered as spherical. It

was assumed that the dominant driving force for particle acceleration was viscous drag force generated by the high speed plasma flow passing the particles. In comparison, other forces acting on a particle such as buoyancy force, gravity, or thermophoresis force are insignificant and hence neglected. The particle to particle interaction was assumed to be absent. Based on the calculation and chart provided by [112], the values of carrier gas and powder feed rate used in this study gave rise to a mean distance between two particles much larger than their mean diameter, which is far enough apart to ignore the interaction between particles. The Knudsen effect was not considered either, because the particle size was not small enough [113]. As for particle heating or cooling, convective heat transfer from plasma to particle and vice versa was considered. The heating of particle by gas radiation was ignored because this effect is slight compared to convective heat transfer to particles. In addition, the particle was assumed to have uniform temperature distribution, i.e. they have perfect thermal conductance or zero thermal resistance. Although a heat transport model which accounts for the heat flow into the particle would be more appropriate, it cannot be achieved at this time due to the following reasons. There are approximately one million particles being injected in this study and it is computationally unfeasible to consider internal conduction for each individual particle. Secondly, the software capability is limited to perfect heat conductance within the particle and special codes need to be developed for predicting heat flow and resultant non-uniform temperature distribution internal to the particle. However, the conclusions of this modeling will remain positive because the main purpose of our modeling is to examine the relative effects of different spraying conditions.

5.2.1 Governing equations

The momentum transport equation coupled with stochastic tracking determines the

particle motion and trajectory. For particle heat transfer formulation, particle heating, cooling, melting, and solidification are governed by the energy transport equation.

5.2.1.1 Momentum transport

Based on Newton second law of motion, the force balance equation in a Lagrangian reference frame that equates particle inertia with the viscous drag force acting on the particle is as follows,

$$\frac{d\boldsymbol{u}_p}{dt} = F_D \tag{5-20}$$

where F_D is the drag force per unit mass and which can be represented as

$$F_D = \frac{3\mu C_D(\boldsymbol{u}-\boldsymbol{u}_p)Re_r}{4\rho_p D_p^2} \tag{5-21}$$

where Re_r is the relative Reynolds number and C_D is the drag coefficient which are defined as,

$$Re_r = \frac{\rho D_p(\boldsymbol{u}-\boldsymbol{u}_p)}{\mu} \tag{5-22}$$

$$C_D = a_1 + \frac{a_2}{Re_r} + \frac{a_3}{Re_r^2} \tag{5-23}$$

where a_1, a_2 and a_3 are constants applicable for smooth spherical particles for a range of Reynolds number [109].

5.2.1.2 Stochastic tracking

When a particle interacts with continuous turbulence eddies, random variations in the instantaneous drag force acting on the particle need to be considered. To account for the turbulence effect on particle trajectories, the "Random Walk Model" was utilized. In this model, the instantaneous value of fluctuating gas flow velocity was used and assumed to

be isotropic and obey the Gaussian probability distribution [109, 114] so that

$$\boldsymbol{u}' = \psi\sqrt{\overline{\boldsymbol{u}'^2}} \tag{5-24}$$

where ψ is a normally distributed random number and $\sqrt{\overline{\boldsymbol{u}'^2}}$ is local root mean square value of the velocity fluctuations. Thus, in Eqs. (5-21) and (5-22), instead of $\boldsymbol{u} = \bar{\boldsymbol{u}}$, the velocity fluctuation was included as $\boldsymbol{u} = \bar{\boldsymbol{u}} + \boldsymbol{u}'$.

5.2.1.3 Energy transport

The concept of energy balance was adopted for convective and latent heat transfer from the surrounding plasma to the particle or vice versa. For the particle heating or cooling phase, the energy equation is

$$h\,A_{\mathrm{p}}\,(T_{\infty} - T_{\mathrm{p}}) = m_{\mathrm{p}}\,C_{\mathrm{p}}\frac{\mathrm{d}T_{\mathrm{p}}}{\mathrm{d}t} \qquad \text{for } T_{\mathrm{p}} < T_{\mathrm{m}} \text{ or } T_{\mathrm{p}} > T_{\mathrm{m}} \tag{5-25}$$

where A_{p}, m_{p}, and C_{p} are the cross section area, mass, and specific heat capacity of the particle, respectively; T_{∞} and T_{p} are the temperature of far field region and the particle, respectively; T_{m} is the melting point of the particle. The heat transfer coefficient, h in Eq. (5-25) was based on [115] correlation and is given in Eq. (5-26),

$$h = \frac{k}{D_{\mathrm{p}}}\,(2.0 + 0.6\,Re_{r}^{0.5}\,Pr^{0.33}) \tag{5-26}$$

As for particle melting or solidification, energy balance is defined as:

$$h\,A_{\mathrm{p}}\,(T_{\infty} - T_{\mathrm{p}}) = m_{\mathrm{p}}\,H_{\mathrm{f}}\frac{\mathrm{d}\varsigma}{\mathrm{d}t} \qquad \text{for } T_{\mathrm{p}} = T_{\mathrm{m}} \tag{5-27}$$

where ς is the liquid fraction and H_{f} is the latent heat of fusion.

5.2.2 Particle size distribution and properties

To introduce Y_2O_3 particles in the model, the particle size distribution in terms of diameter versus percentage weight was curve-fitted via a Rosin-Rammler distribution and

numerically introduced to the plasma field. The thermodynamics and transport properties of Y_2O_3 particles required in the simulation are shown in **Table 5.2**. In addition, **Fig. 5.2** shows the flow chart of the solution procedure for particles laden plasma flow.

Table 5.2. Thermodynamic and transport properties of Y_2O_3 particles

Property	Value
Density ρ_p, kg/m^3	5030
Specific heat capacity C_p, J/kg K	*Eqn. below
Latent heat of fusion H_f, J/kg	3.71×10^5
Thermal conductivity k_p, W/mK	12
Kinematic viscosity v_p, m^2/s	5.8×10^{-6}
Melting point T_m, K	2703
Boiling point T_b, K	4573

* For $273 < T_p < 873$K,

$C_p = 3.6273\times10^{-8}\ T_p^3 - 2.02475\times10^{-4}\ T_p^2 + 0.38864\ T_p + 362.26349$

For $T_p > 3000$ K, $C_p = 674.5$

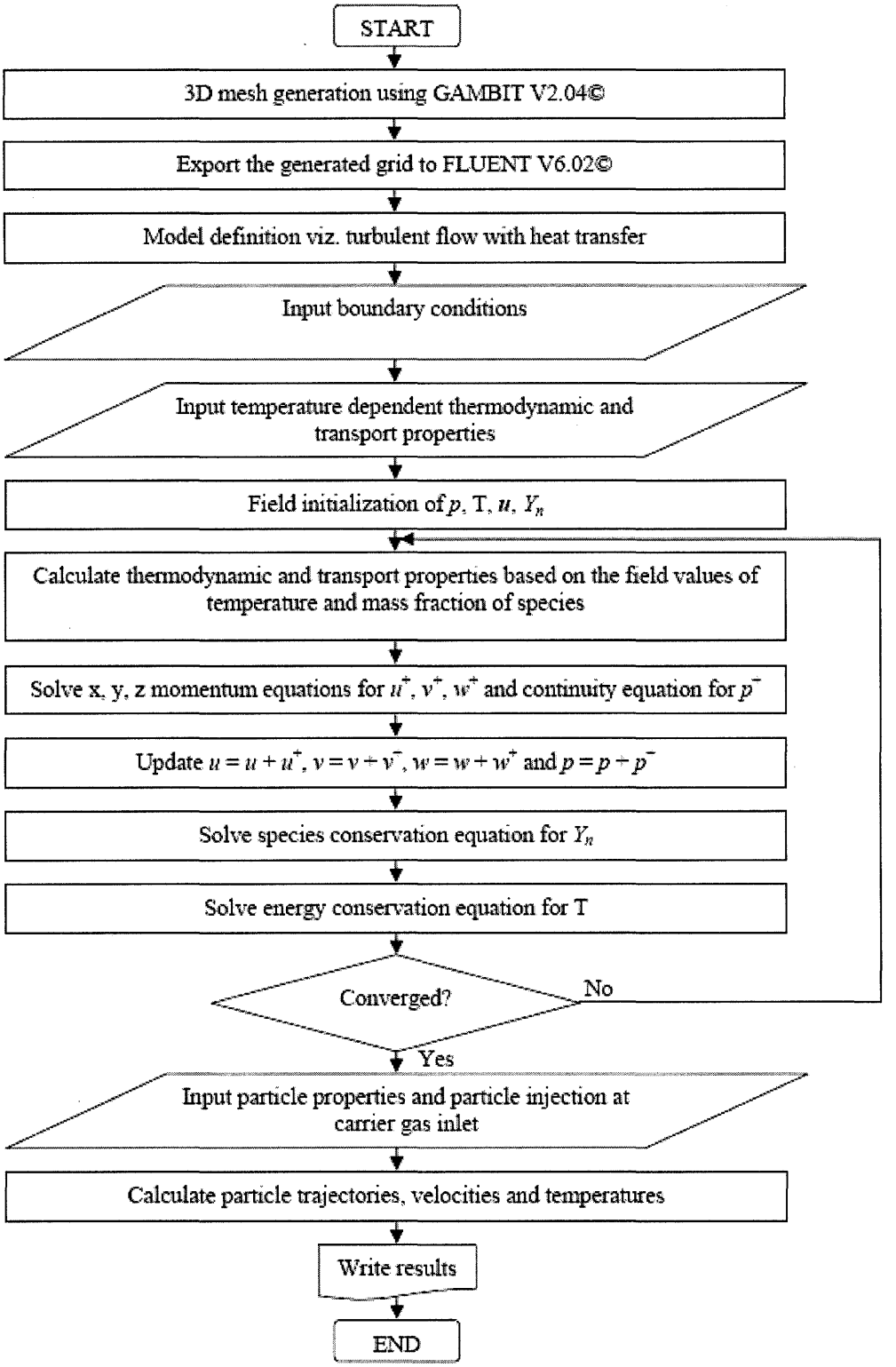

Fig. 5.2. Flow chart of the solution procedure for particles laden plasma flow

5.3 Modeling results

5.3.1 Plasma temperature

Fig. 5.3, **5.4**, and **5.5** illustrate the temperature flood and contour of Ar, Ar/O_2, and (Ar/O_2 + acetone) RF-ICP field, respectively. It can be seen that for all the three cases, the highest temperature is always located in the torch zone which is surrounded by the coils. Once released to the free space in the chamber beneath the torch exit, the plasma temperature started to drop at a certain gradient which varied with processing conditions. The value of highest temperature only describes the temperature field inside the torch. It is the volume average temperature of the chamber that is crucial for evaluating the plasma enthalpy level and comparing the particle heat treatment degree. For the three modeled cases of Ar, Ar/O_2, and (Ar/O_2 + acetone) plasma, the highest temperature is 10613 K, 9560 K, and 11453 K, and the volume average temperature of chamber is 617 K, 2410 K, and 2627 K, respectively. Obviously the Ar/O_2 plasma field had much higher enthalpy level than Ar plasma, and the combustion-aided plasma field's enthalpy was even higher.

The shape and size of the plasma plume were different after introducing O_2 as secondary gas. In order to define the plume zone, we may take the isotherm of 4000 K, which is the boiling point of Sm_2O_3, as the boundary of the plasma plume. From the illustration of Ar plasma in **Fig.5.3**, the plume is narrow and approximately 0.15 m long, concentrating at around torch exit along the centerline of the chamber. However, in **Fig. 5.4** Ar/O_2 plasma, the plume is about two times broader and two times longer. For the (Ar/O_2 + acetone) plasma in **Fig. 5.5**, the plume is even broader but shorter than Ar/O_2 plasma. If we take the isotherm of 2600 K, which is the melting point of Sm_2O_3, as the boundary of plasma diffused zone, it is only a narrow shuttle-shaped zone along the centerline for Ar plasma,

whereas that one of Ar/O_2 and (Ar/O_2 + acetone) plasma spreads almost to the overall chamber domain.

Examining the temperature distributions along axial and radial directions of the three cases would be of much help in the understanding of the temperature diversity. In **Fig. 5.6** (a) the axial direction temperature distribution curves along the centerline, the maximum of the three cases are all located at the zone right after the torch exit, with the values decreasing in the order of Ar→Ar/O_2→(Ar/O_2+acetone) plasma. However, after the maximum, the temperature of Ar plasma drops much more sharply than the other two, followed by Ar/O_2 plasma. From the radial views at 0.1 m and 0.2 standoff positions in **Fig. 5.6** (b) and (c), it can be clearly seen that the temperature distributions of Ar plasma are quite narrow, and the high-temperature field concentrates at around the torch centerline. In comparison, the Ar/O_2 plasma has its temperature and enthalpy dispersed twice as broadly as the Ar plasma across the radial direction, and the (Ar/O_2+acetone) plasma field is even broader than the Ar/O_2 plasma but shorter. Combining the temperature distributions and chamber volume average temperature results, the following conclusions can be drawn.

(i) Ar/O_2 and (Ar/O_2+acetone) plasmas have much higher volume average temperature and average enthalpy than Ar plasma throughout the computational domain. The values increase in the sequence of Ar → Ar/O_2 → (Ar/O_2+acetone).

(ii) In the three modeling cases, most of the plasma enthalpy is concentrated at a shuttle-shaped zone beneath the torch exit along its centerline, the temperature of which is above 4000 K. The dimension of this zone is 0.02×0.15 m (width×length) for Ar plasma, 0.05×0.3 m for Ar/O_2 plasma, and 0.06×0.25 m for (Ar/O_2+acetone) plasma.

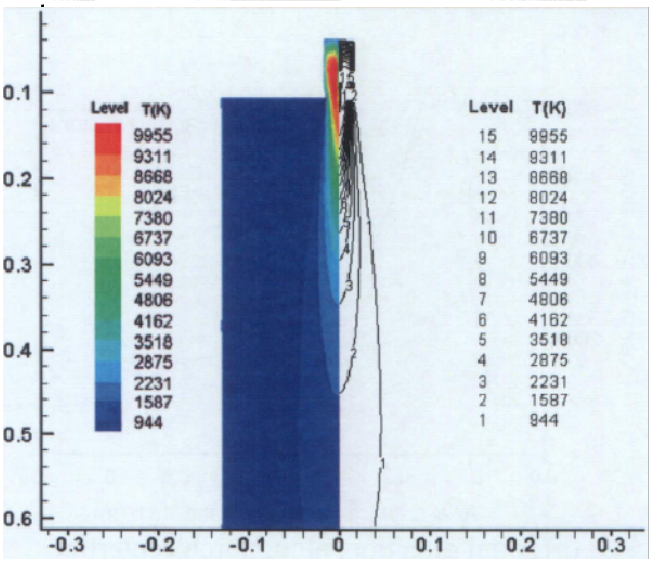

Fig. 5.3. Temperature flood and contour of Ar RF-ICP

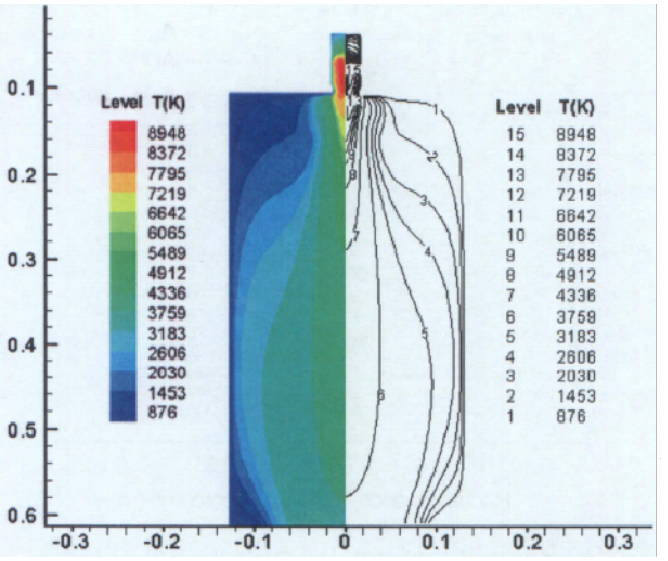

Fig. 5.4. Temperature flood and contour of Ar/O_2 RF-ICP

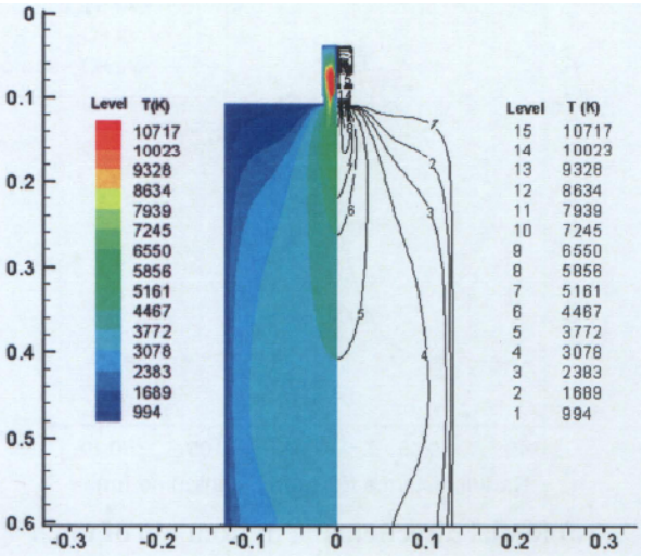

Fig. 5.5. Temperature flood and contour of (Ar/O_2 + acetone) RF-ICP

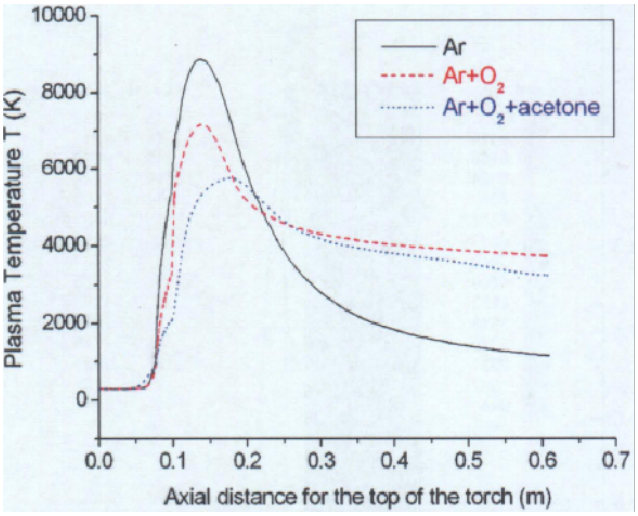

(a) Axial direction, along torch centerline

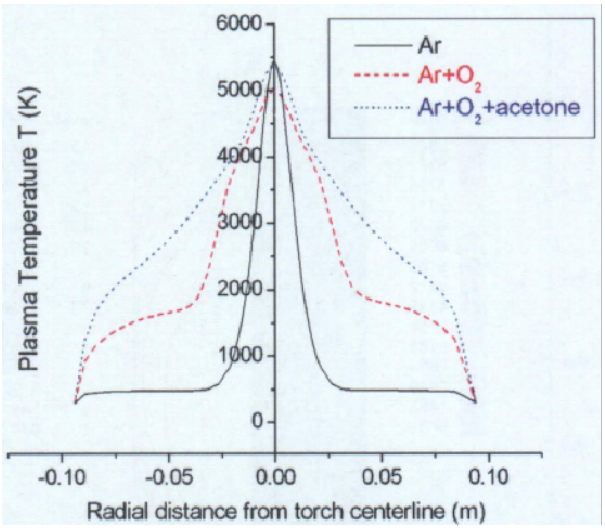

(b) Radial direction, 0.1 m from top of torch

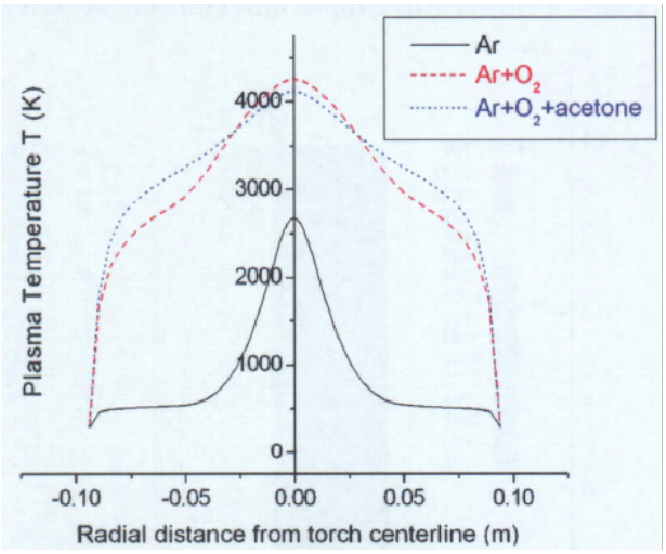

(c) Radial direction, 0.2 m from top of torch

Fig. 5.6. Plasma temperature distributions along axial and radial directions

5.3.2 Plasma velocity

The velocity contours of Ar, Ar/O_2, and (Ar/O_2+acetone) plasma are illustrated in **Fig. 5.7** (a), (b), and (c) respectively. In all cases, plasma velocity reaches its maximum right after leaving the injector nozzle, and drops with a certain gradient when moving downwards. The velocity diversity is large between cases. Ar plasma has the highest starting velocity value at about 400 m/s, and decays to 1 m/s within the computational domain. The Ar/O_2 plasma has a similar contour pattern as Ar plasma, except that the starting velocity is much lower, at 250 m/s. As for (Ar/O_2+acetone) plasma, the velocity is extraordinarily low, with a starting value of 20 m/s.

Likewise, axial and radial direction velocity distributions in **Fig. 5.8** give a better understanding of the velocity diversity. The axial direction velocity distribution curves in **Fig. 5.8** (a) indicate that the maximum of the velocities is located at injector nozzle, and the maximum value decreases dramatically in the sequence of Ar→Ar/O_2→(Ar/O_2+acetone) plasma. Determined from the radial direction velocity distributions in **Fig. 5.8** (b) and (c), the Ar plasma is mainly confined within the 0.1 m wide core-shaped zone around the torch centerline. With the distance from the torch increasing, the velocity difference between cases gets smaller.

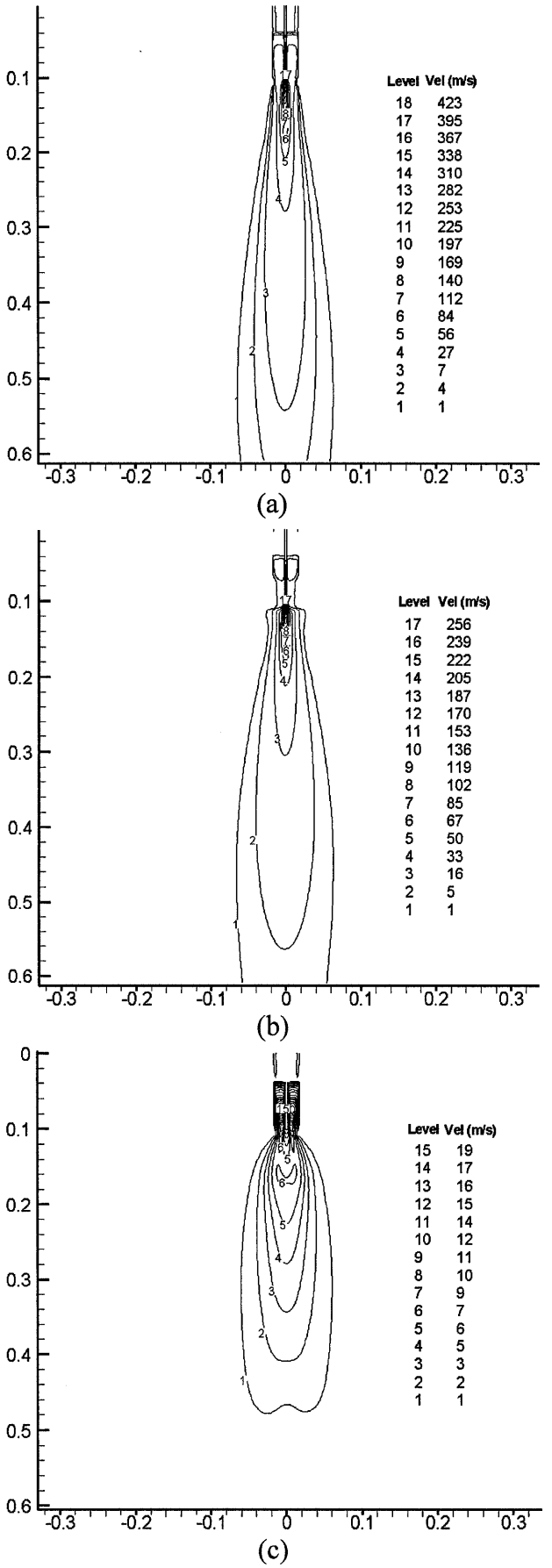

Fig. 5.7. Velocity contour of (a) Ar; (b) Ar/O_2; (c) (Ar/O_2 + acetone) plasma

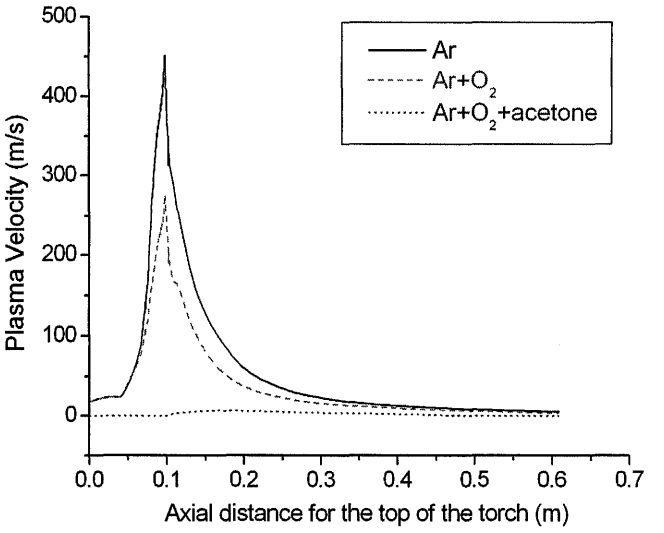

(a) Axial direction, along torch centerline

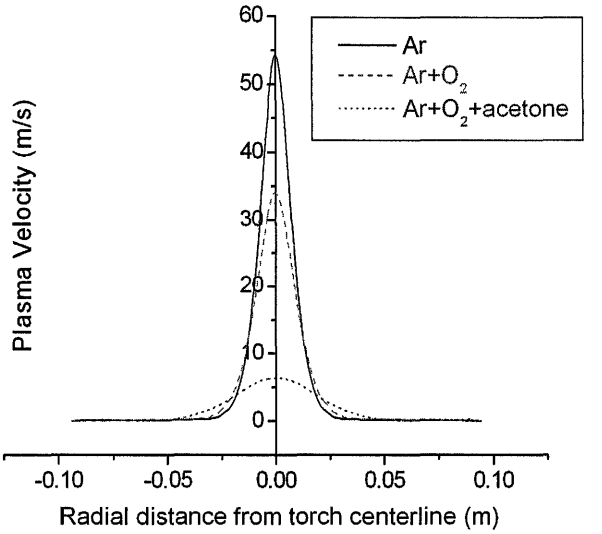

(b) Radial direction, 0.1 m from top of torch

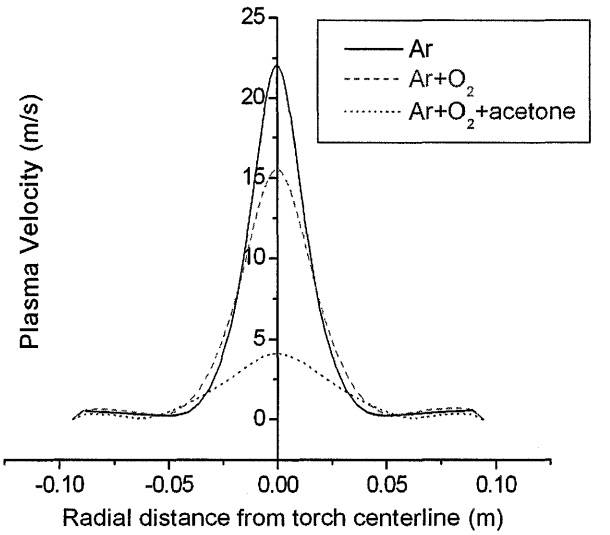

(c) Radial direction, 0.2 m from top of torch

Fig. 5.8. Plasma velocity distributions along axial and radial directions

5.3.3 Particle behavior

Since the particles were entrained in the plasma flow, the in-flight behavior is dependent on two factors: temperature and velocity distributions of the plasma field which transfer energy and momentum to the particles, and particle characteristics such as size and thermodynamic properties. The in-flight behavior of the particles or droplets including temperature, velocity, number concentration, and size was simulated and their contours are shown in **Fig. 5.9**, **5.10**, **5.11**, and **5.12**, respectively. All the views are radial cross sections of the plume at 0.3 m standoff distance from the top of the torch. The contours were plotted by processing the FLUENT© output data through a FORTRAN© program.

The particle temperature distribution contours in **Fig. 5.9** are strongly related to the plasma temperature and velocity distributions. For particles in Ar plasma in **Fig. 5.9** (a), the high temperature contours are concentrated at the center of chamber cross section, on account of the concentrated Ar plasma plume. In contrast, the temperature distributions of particles in Ar/O_2 and (Ar/O_2+acetone) plasma (**Fig. 5.9** (b) and (c)) are much more divergent, which means the particles are heated more homogeneously. In comparison with maximum particle temperature 3000 K of Ar plasma, particles in Ar/O_2 and (Ar/O_2+acetone) plasmas have a maximum temperature at about 4500 K. Obviously this results from the higher plasma enthalpy and longer residence time.

Taking both particle velocity and number distributions into account (**Fig. 5.10** and **5.11**), it can be seen that the particle trajectories are very much associated with the plasma plume shape and velocity. The particle velocity in Ar plasma is the highest for the three cases and the particles concentrate at the core of the plasma plume. This is because the concentrated high-velocity Ar plasma transfers its high momentum to the entrained

particles and the velocity vectors are mostly parallel to the centerline. Whereas for the other two cases, the particles have lower velocities and were dispersed to a much larger area. This indicates that the plasma momentum is distributed more uniformly to the particles, but their velocity direction is more random. To sum up, the particles' dispersivity increases in the order of Ar→Ar/O_2→(Ar/O_2+acetone) plasma, same as the order of plasma plume broadening and velocity decreasing.

The particle size distributions in **Fig. 5.12** represent only the micron-sized in-flight particles. It is the consequence of the particle temperature and trajectory distributions as well as the initial particle size distribution. The traces show qualitatively that the average particle size decreases across Ar→Ar/O_2→(Ar/O_2+acetone) plasma. In addition, the small particles in Ar plasma mainly gather at the core of the plume where the high-temperature zone exists, whereas they dispersed to almost the whole cross section in Ar/O_2 and (Ar/O_2+acetone) plasma because of the diffused plasma enthalpy and longer residence time.

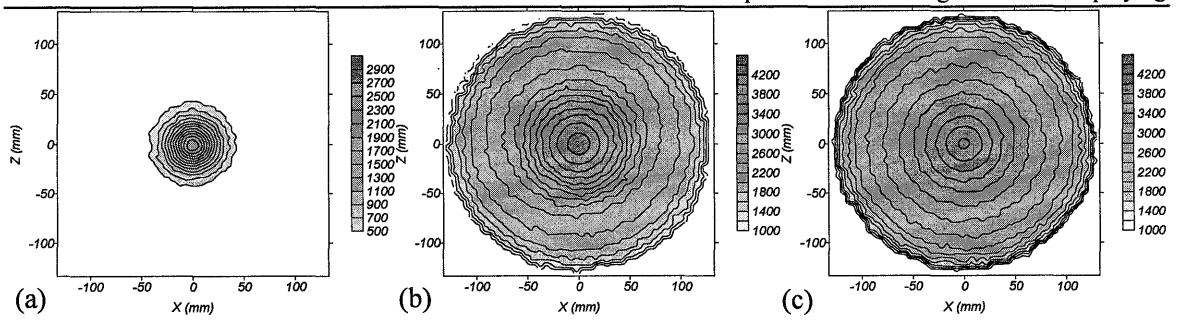

Fig. 5.9. Contour of in-flight particle temperature distribution. (a) Ar; (b) Ar/O_2; (c) (Ar/O_2+acetone)

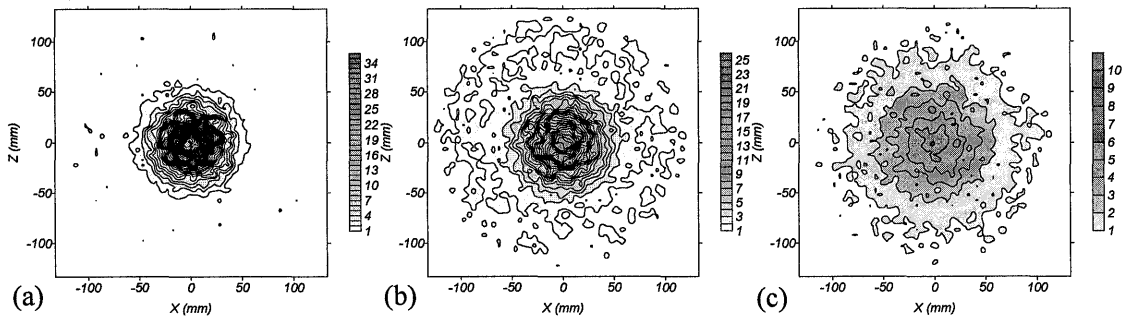

Fig. 5.10. Contour of in-flight particle velocity distribution. (a) Ar; (b) Ar/O_2; (c) (Ar/O_2+acetone)

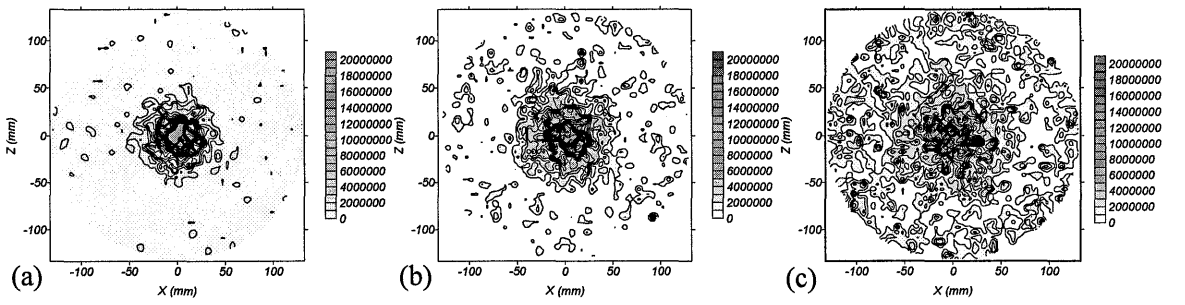

Fig. 5.11. Contour of in-flight particle number distribution. (a) Ar; (b) Ar/O_2; (c) (Ar/O_2+acetone)

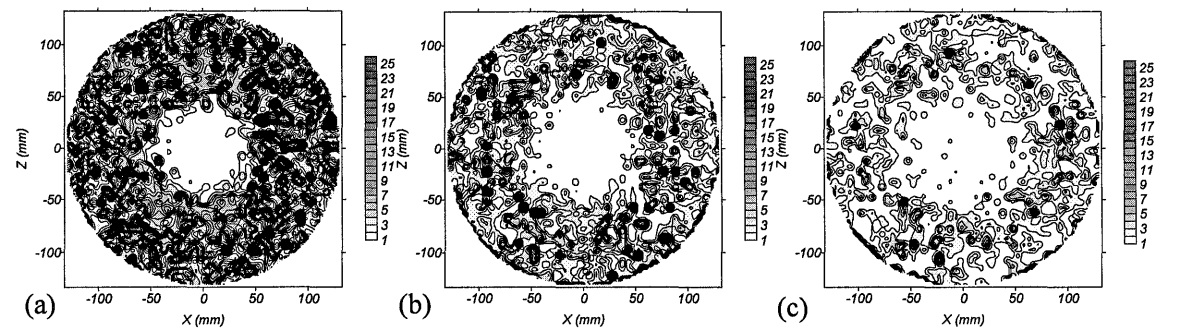

Fig. 5.12. Contour of in-flight particle diameter distribution. (a) Ar; (b) Ar/O_2; (c) (Ar/O_2+acetone)

Chapter Six: Discussion

The discussions in this chapter are based on the results in chapter four and five. Specifically, discussions in Section **6.1** to **6.5** correspond to Section **4.1** to **4.5** respectively.

6.1 Behavior of various rare earth oxides under powder feed spraying

6.1.1 Mechanism of micron-sized particle formation

In Section 4.1.1, there are two trends found in the SEM micrographs in **Fig. 4.1**. Firstly, for all the three sprayed materials, the amount of irregularly shaped large particles decreases from C1 to C3, whereas the amount of nanoparticles increases (**Fig. 4.1**, C1→C3). Quantitative particle size analysis also shows that the particle size decreases in the order of Raw→C1→C2→C3 (**Fig. 4.3** (b), **Fig. 4.4**). This is the consequence of the classification function of the cyclone and chambers. Smaller and lighter particles tend to be carried farther and subside into C3. Secondly, for all the three chambers, the amount of irregular shape particles increases from Sm_2O_3 to Lu_2O_3, whereas the amount of nanoparticles decreases (**Fig. 4.1**, Sm_2O_3→Lu_2O_3). This is attributed to the different thermodynamic stability of the raw materials. From Sm_2O_3, Dy_2O_3 to Lu_2O_3, the stability and the melting and vaporization temperature increases, with Sm_2O_3 the easiest to melt and vaporize whereas Lu_2O_3 the hardest ($T_{m,\ Sm2O3}$ = 2335°C; $T_{m,\ Dy2O3}$ = 2408 °C; $T_{m,\ Lu2O3}$ = 2490 °C). Consequently, under the same spraying conditions, there were less irregularly shaped micron-sized particles and more nanoparticles for Sm_2O_3 than for Lu_2O_3. The diversity in thermodynamic stability of rare earth oxides was also exhibited by means of the nanoparticles productivity, which is an indication of the particle evaporation degree. It is illustrated in **Fig. 4.5** that the nanoparticle productivity descends across

$Sm_2O_3 \rightarrow Dy_2O_3 \rightarrow Lu_2O_3$. Since the nanoparticles almost all came from vapor condensation in plasma spraying, it can be inferred that Sm_2O_3 particles vaporized the most while Lu_2O_3 the least under the same conditions, which is in line with the boiling points of the oxides and the results of particle morphology.

The wide particle size distribution of the micron-sized sprayed particles observed from the SEM micrographs in **Fig. 4.1** can be attributed to two factors. The first is the different degree of heat treatment results from the plasma plume thermal gradient and the different residence times of the injected particles therein. In principle, injected particles undergo heating, flash melting, and subsequent evaporation in the plume. After leaving the plasma plume tail, the material is quenched at a rate up to 10^5 °C/s [116]. The vapor phase condenses into nanoparticles, while the remaining particles become spherical or irregular-shaped micron-sized particles. Generally, the whole process takes about 10 milliseconds depending on the size of the plume, the particle trajectory, and the particle velocity in the plasma [116]. Undoubtedly, increasing the energy input promotes further melting and evaporation and changes particle size. But for the same material under the constant process conditions, the degree of heat treatment for each particle still can be different due to their different residence time. When fed downstream into the plasma plume, particles take various trajectories and velocities due to their size and momentum diversity. All these trajectories form a cone-shaped trajectory zone in the plasma plume as illustrated in **Fig. 6.1**. The residence time is dependent on both particle trajectory and velocity in the plume. Those particles traveling throughout the whole plume length or having low velocities undergo a longer residence time in the plume. They experience a higher heat treatment degree which facilitates melting and evaporation and results in smaller spherical particles. On the other hand, particles with high velocity and short

residence time receive insufficient heat input and results in large spherical or irregular-shaped particles. This effect has been confirmed by modeling results in Chapter Five. The cone-shaped trajectories can be deduced from the particle number distribution in **Fig. 5.11** (a), and particle velocity diversity is shown in **Fig. 5.10** (a). The consequent particle temperature and size diversity are shown in **Fig. 5.9** (a) and **Fig. 5.12** (a). The second factor that affected particle size distribution is the particle size difference within the raw material particles. Due to the high thermodynamic stability of rare earth oxides, large particles only vaporize partially at the surface, while small ones are liable to vaporize totally. After spraying, basically, the size distribution of the resulting micron-sized particles is correlated with their original size distribution. This can be verified from the quantitative particle size analysis in **Fig. 4.3** (a), (c), and (d). For both C1 and C2 particles, the sequence of the mean sizes and distributions follow those of their raw materials. In view of the above two factors, a wide particle size distribution of the micron-sized particles is inevitable. The mechanism of nanoparticles formation is in some ways different from micron-sized particles. It will be discussed in Section 6.3.3.

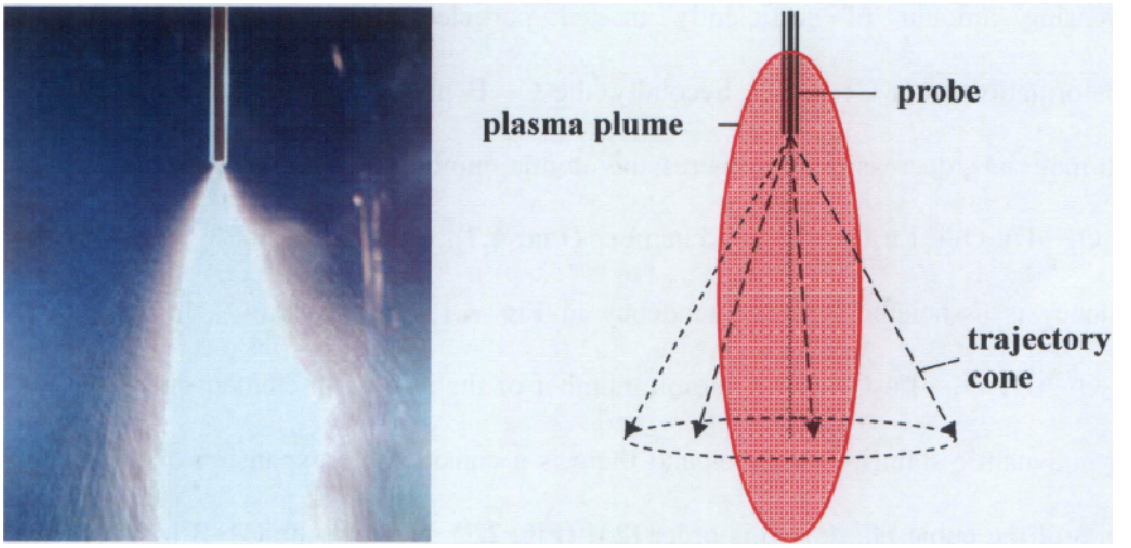

Fig. 6.1. Photograph and schematic diagram of spraying trajectory cone

6.1.2 Influence of heat treatment degree and material properties on phase transformation

From the XRD patterns and their quantitative analysis in Section 4.1.3, two tendencies are observed, which have a strong correlation with the trends observed for particle morphology. Firstly, for each of the rare earth oxide, there is a plasma induced C→B phase transformation after spraying, the degree of which decreases across C1, C2, and C3 (**Fig. 4.7**). A typical example is the Dy_2O_3 patterns shown in **Fig. 4.6**. This tendency is related to that of particle morphology in **Fig. 4.1**, C1→C3, both of which are the consequence of the particles being heat treated differently. The C→B phase transformation is a high temperature-induced process that requires high enthalpy input. As discussed before, the nanoparticles were condensed from a vapor phase, thus they should have undergone higher degree of heat treatment than the irregular-shaped particles that were not even melted. Due to the tendency of increasing proportion of nanoparticles and decreasing proportion of irregular-shaped particles from C1 to C3 (resulted from classification effect according to particle weight), it is safe to conclude that there was an increasing amount of sufficiently treated particles and increasing C→B phase transformation from C1 to C3. Secondly, the C→B phase transformation degree varies with materials, decreasing with increasing atomic number of the rare earth species across Sm_2O_3→Dy_2O_3→Lu_2O_3 for each chamber (**Fig. 4.7**), especially for C3 (**Fig. 4.8**). This tendency is associated with the tendency in **Fig. 4.1**, Sm_2O_3→Lu_2O_3. In the order of Sm_2O_3→Dy_2O_3→Lu_2O_3, as the atomic number of the rare earth element increases, their thermodynamic stability increases and there is a considerable expansion of the stability region of the cubic phase in this order [23] (**Fig. 2.2**). Namely, the C→B transformation threshold temperature increases and cubic structure becomes more and more stable. Therefore, under the same processing conditions, the C→B transformation became harder

across the series $Sm_2O_3 \rightarrow Dy_2O_3 \rightarrow Lu_2O_3$, leading to a decreasing proportion of monoclinic phase in the sprayed particles.

A comparison of the SEM results with those of the XRD analysis suggests that the nanoparticles are mainly composed of crystallites with B-type structure. However, it should be kept in mind that there are also nanoparticles which do not have a monoclinic structure. Lu_2O_3 powder collected in chamber C2, for instance, consists of nanoparticles (**Fig. 4.1**, c_2), but only Bragg reflections of the cubic C-type phase are observable in the diffraction pattern. Furthermore, not all of the large spherical particles are cubic. Sm_2O_3 powder collected in chamber C2 contains a high proportion of micron-sized spheres, whereby the dominant phase is the monoclinic one (**Fig. 4.7**).

Rare earth oxides are remarkably stable materials with respect to chemical reaction and phase stability. Thus, it takes a large amount of energy for the C→B transformation process to proceed, and generally the monoclinic phase only stabilizes at high temperature. The high-temperature equilibrium monoclinic phase found in our study was formed during spraying at very high temperature up to 10000 K, and was retained at room temperature due to the rapid quenching involving a cooling rate of the order of 10^5 K/s. Early in 1989, the plasma-induced rare earth oxide phase transformation phenomenon was reported by Koththavasal et al. [117] in their research on plasma sprayed Dy_2O_3 coating. The coatings consisted mostly of a metastable monoclinic phase and minor amounts of cubic phase, and the monoclinic phase reverted to 50% cubic phase on annealing in air at 800 °C for 5h. According to Kim et al. [101], the monoclinic B-type structure is thermodynamically unstable at room temperature because the lattice is inherently strained and some rare earth atoms are getting so close to each other that strong repulsive forces are developed in the structure. Thus, the B-type structure tends to

transform back into the cubic C-type structure which has larger R-R distances to release lattice strains and the cation charge repulsion by maximizing the volume. This B-type to C-type transformation is displacive, involving the breaking of some R-O bonds and the reconstruction of the coordination. Thus, an energy input is required to overcome the barrier of breaking the R-O bonds in the structure. One possible means is to heat treat the material at below the C→B transformation temperature as Venkatachari et al did [117]. Similarly, in our study, it was found that annealing the sprayed Dy_2O_3 powder at 1000°C for 4 h induced a 88% B-type structure reversion to the C-type structure.

Another crystallographic phenomenon caused by plasma spraying is the unit cell volume change. There was a unit cell volume contraction in the order of Raw→C1→C2→C3 particles for all sprayed oxides (**Fig. 4.9**). The trend is quite obvious for both cubic and monoclinic phases, and the contraction degree varies with material. This is also associated with crystal structure transformation. The rare earth oxide C-type structure is of the cubic bixbyite type in space group $Ia\bar{3}$, containing 32 metal atoms and 48 oxygen atoms per unit cell, related to a doubled-edge fluorite structure with one-fourth of the oxygen sites vacant and regularly ordered. All metal atoms are coordinated by heavily distorted octahedra of oxygen atoms, i.e. the coordination number of the cation is 6 (**Fig. 6.2** (a)). A cubic structure is the most stable phase for most rare earth oxides like Y, Dy, and Lu oxides. Increasing the temperature of the cubic phase results in the formation of B-type structure for these rare earth oxides. The B-type structure has a monoclinic structure with space group C2/m, with 12 metal atoms and 18 oxygen atoms per unit cell. Some of the cations become seven-fold coordinated by oxygen atoms while others are still in a distorted octahedral environment (**Fig. 6.2** (b)). At even higher temperature, the A-type structure, which is closely related to the B-type, is formed. All metal atoms are seven-fold

coordinated, and the cation array is now perfectly hexagonal closed packed (hcp) [23] (**Fig. 6.2** (c)). From C→B→A, the distance between cations becomes shorter and the unit cell volume becomes smaller. The volume difference is large between B and C for rare earth oxides, but small between A and B. For instance, the calculated volume change in the C to B transformation of Dy_2O_3 is -8.9%. Therefore, being heat-treated by plasma at very high temperature, the rare earth oxide cubic unit cell started to lose oxygen and distort, and the cations tended to move closer to each other to form monoclinic unit cells. Likewise, the monoclinic unit cells lost oxygen and the cations tended to move even closer to form A-type or other high-temperature equilibrium phases. The plasma treatment duration was very short. When the materials left the plume and cooled at a high rate, all the movement at high temperature was frozen and retained at room temperature. As a result, some of the cubic unit cells accomplished the transition process and became B-type monoclinic structure, which was represented by the degree of phase transformation discussed previously. On the other hand, those cubic and monoclinic unit cells in the middle of the transition were still identified as being their previous phases, but exhibiting unit cell contraction and distortion phenomena. Certainly, the contraction degree varied with rare earth oxides because the mobility of the atoms in their unit cells is different.

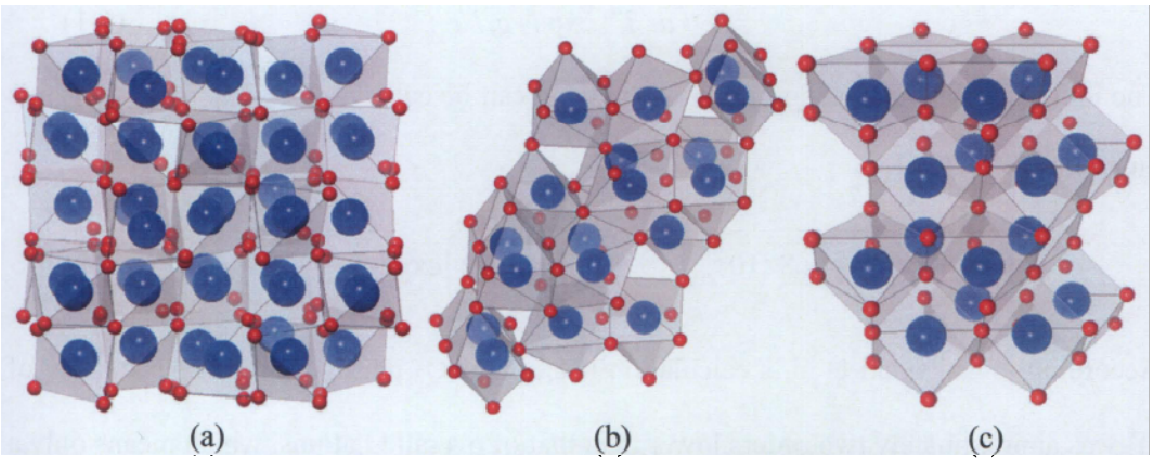

Fig. 6.2. The polyhedral representation of (a) cubic C-type (b) monoclinic B-type (c) hexagonal A-type structure of R_2O_3. The large and small spheres stand for R and O atoms, respectively [118]

6.2 Effects of O_2 introduction on powder feed spraying

6.2.1 O_2 effects on plasma thermophysical properties

In Section 4.2, the comparison of the results of Ar and Ar/O_2 plasma spraying show that the introduction of O_2 secondary plasma gas in both central and sheath gas resulted in a dramatic improvement in plasma enthalpy and heat treatment level. The indicators of O_2 influence and enthalpy elevation were determined as particle morphology, productivity, and crystal structure.

Generally, the working fluid in RF-ICP spraying is pure Ar, but for the elevation of the plasma enthalpy or other particular applications, e.g. chemical reactive spraying, it is often necessary or advantageous to add a secondary molecular gas such as H_2, O_2, or N_2. In our spraying, O_2 was chosen because the rare earth oxides require an oxidizing atmosphere. Six species including Ar, Ar^+, O, O_2, O^+, and e^- were considered to be the dominant reactants in Ar/O_2 plasma, as shown in **Table 6.1**. The dissociation and ionization rates can be calculated by Eq. (6-1). The constants in Eq. (6-1) are presented in **Tables 6.1** taken from Refs. [119-121].

$$k_f = a_l \, T^{b_1} \exp(-c_l / T) \qquad (6\text{-}1)$$

The ionization rate of reaction no. 6 in the table can be calculated by Eq. (6-2), which is taken from Ref. [122].

$$k_f = 1.68\times10^{-20} \, T^{1.5} \left(\frac{135300}{T} + 2\right) \exp\left(-\frac{135300}{T}\right) \qquad (6\text{-}2)$$

According to Takayuki et al.'s calculation [81], in Ar/O_2 plasma, the number density of O^+ was approximately two orders lower than that of overall O atoms, which means only a few percent O atoms present from dissociation were ionized into O^+. Therefore, for

simplicity reason, we can neglect the ionization and only discuss the O_2 dissociation effects in our cases.

Table 6.1. Chemical reactions in Ar/O_2 plasmas

No.	Reaction	a_1 (mol dm^{-3} s^{-1})	b_1	c_1 (K)
1	$O_2 + O_2 \rightarrow O + O + O_2$	2.0×10^{21}	-1.5	59,500
2	$O_2 + O \rightarrow O + O + O$	1.0×10^{22}	-1.5	59,500
3	$O_2 + Ar \rightarrow Ar + O + O$	1.0×10^{22}	-1.5	59,500
4	$O_2 + e^- \rightarrow O + O + e^-$	9.68×10^{22}	-2.0	59,500
5	$O + e^- \rightarrow O^+ + e^- + e^-$	3.91×10^{33}	-3.78	158,500
6	$Ar + e^- \rightarrow Ar^+ + e^- + e^-$	k_f taken from Ref. [122]		

The strong effects of O_2 addition on the character of the plasma can be visually observed. In comparison with Ar plasma, the Ar/O_2 plasma plume was broader and longer and its brightness increased dramatically, which is in accord with the modeling results in **Fig. 5.3** and **5.4**. This extraordinary behavior can be explained by the thermodynamic properties of O_2. Oxygen molecules have a dissociation temperature between 3500 and 4000 K and a low dissociation energy of 5.1 eV. A high plasma temperature field above 4000 K provides enough kinetics for oxygen dissociation. This dissociation process strongly enhances oxygen's specific heat and thermal conductivity. In other words, inside the torch, when the temperature is high enough, oxygen molecules absorb a large amount of energy from the torch and dissociate into O atoms. This additional energy will subsequently be released through recombination of O atoms in the relatively low-temperature zone underneath the torch. It has been demonstrated by Hsu et al. [83] that electron impact dissociation of the O_2 molecules is the dominant reaction that produces O radicals in O_2-containing plasmas. Therefore, specifically in the RF-ICP torch, the electrons from Ar ionization are accelerated by the inductively coupled electrical field and transfer their energy to oxygen molecules by collision. The dissociation product O atoms move downstream into the chamber where the temperature is low enough for their recombination, form oxygen molecules again and release the additional energy in the

form of heat. Hence, the oxygen dissociation and recombination process actually transfers additional energy from torch to chamber and increases the torch efficiency. This additional energy, which would otherwise dissipate through water-cooling of the torch and injector, elevates the plasma enthalpy of the chamber remarkably, as indicated by volume average temperature increase (Ar: 617 K → Ar/O_2: 2410 K) in Chapter Five modeling results. On the other hand, according to our modeling results, the highest temperature in the torch decreases from 10613 K to 9560 K with oxygen introduction. This is because the large energy consumption caused by oxygen dissociation results in a significant temperature drop near the torch wall region. This temperature drop in turn causes a more moderate temperature gradient near the torch wall compared with Ar plasma, and leads to a decrease of heat loss at the wall, which results in higher energy efficiency of the torch.

Velocity of the plasma is also affected by O_2 introduction as revealed by modeling contours in **Fig. 5.7** (a) and (b). The starting velocity of Ar/O_2 plasma at the injector nozzle is almost halved in comparison with Ar plasma, and the velocity drops with a more modest gradient. This can be attributed to the oxygen dissociation and recombination process too. As mentioned above, the electrons from Ar ionization are accelerated by the electrical field in the torch, and transfer energy to oxygen molecules through collisions. The electrons are slowed down during the collisions and their kinetic energy is transferred to oxygen. Since the oxygen molecules are much larger and heavier than electrons and most of the energy they obtain from collisions is spent on their dissociation process, their acceleration is limited and the overall plasma species velocity will be much lower than that of Ar plasma. What is more, the oxygen recombination process elevates the plasma volume average temperature by almost four times, which will increase the kinematic

viscosity of the plasma species (For a plasma, the kinematic viscosity will increase with higher temperature.). This, to some extent, will also reduce the plasma velocity.

6.2.2 Benefits to particle heat treatment

As discussed above, O_2 introduction induced a significant enthalpy elevation and velocity reduction of the plasma field, as well as the broadening and extension of the plasma plume. These changes in plasma properties are very beneficial to the particle heat treatment. For the same material, the heat treatment degree of particles in plasma depends on two factors: the plasma enthalpy and the residence time. Either higher plasma enthalpy or longer residence time benefits the heat treatment of the particles. O_2 introduction accomplishes both of them at the same time by offering a larger plume volume with higher enthalpy and a lower plasma velocity. Additionally, as shown in **Fig. 5.4** and **Fig. 5.9** (b), the high temperature field of Ar/O_2 plasma dispersed to almost the entire chamber. Thus, the non-uniformity of heat treatment caused by the particle spray cone can be reduced considerably. Consequently, the as-sprayed micron-sized particles comprised few irregular-shaped particles and the particle sizes became smaller and more uniform, as confirmed by the modeled particle size distribution in **Fig. 5.12** (b) and the experimental results in **Fig. 4.10**. In addition, the productivity of nanoparticles, which is an indication of the heat treatment level, increased by more than two times compared with Ar plasma for all the sprayed oxide (**Fig. 4.12**). Moreover, the mean size of the nanoparticles decreased and the size distribution became narrower, as shown in **Fig. 4.11**. Both changes are the consequence of the formation of a higher supersaturation degree during the nucleation process, which in turn resulted from the plasma thermophysical properties change due to O_2 introduction. To avoid redundancy, detailed discussion on the mechanism of nanoparticle formation associated with supersaturation degree and cooling

rate will be presented in Section 6.3.3.

As far as the crystal structure is concerned, the C→B phase transformation degree of the oxides studied also increased with O_2 introduction, especially for Y_2O_3 and Dy_2O_3 (**Fig. 4.14**, **4.15**, and **4.16**). But the increased degree was not as significant as that of productivity, with only a 3 wt% increase of monoclinic phase. As discussed previously, for the same rare earth oxide, a higher heat treatment degree leads to an increasing degree of C→B phase transformation. In Ar/O_2 plasma, not only the plasma field was extended with a temperature higher than phase transformation threshold (**Fig. 5.4** (b)), but also the particle residence time in it was prolonged (**Fig. 5.10** (b)). Hence, both reaction kinetics and reaction time for the C→B phase transformation were improved. However, comparing the modeling results to the phase compositions in **Fig. 4.16**, it seems that the correlation between plasma enthalpy and phase transformation degree is not linear. The possible reason could be that the oxidation atmosphere in Ar/O_2 plasma restricted the oxygen loss and the unit cell distortion of the cubic structure, and thereby reduced the degree of C→B phase transformation.

6.3 Effects of suspension concentration and solvent type on SPS

Suspension plasma spraying (SPS) was employed in our research with the intention to improve the flowability of the feedstock. The solvent type and suspension concentration of SPS have to be optimized in the first place because no systematic research on these has been carried out so far.

6.3.1 Suspension concentration influence

In Section 4.3.1, water solvent was used to study the concentration impact on particle

morphology in SPS. A 20 wt% concentration was proved to be a good compromise between heat treatment and flowability for water SPS. In SPS, the plasma provided energy for both droplet drying and particle melting and vaporization. Y_2O_3 has a very high thermodynamic stability (T_m = 2430°C) and requires a high energy to melt and vaporize. However, the 10 wt% suspension had a relatively high content of water, the evaporation of which consumed a large proportion of the total energy. With the water content decreasing, e.g. for 20 wt% concentration, less energy was spent on water evaporation and more energy was left for particle melting and vaporization. Accordingly, the yield of micron-sized spherical particles and nanoparticles increased. However, a 30 wt% concentration did not increase the yield further. This could be associated with the fact that the net particle feed rate in 30 wt% concentration SPS was too high for the finite plasma power of 21 kW, even though the energy share for particles increased due to the decreasing water content. Another disadvantage of 30 wt% suspension was that clogging occurred from time to time during spraying, which caused an inconsistent feed and heat treatment, as in powder feed. To sum up, a proper ratio of solvent and particle in SPS has to be selected to guarantee a comparatively high enthalpy share for particle heating as well as a good flowability of the feed. It should be noted that this ratio could be different when using other solvents or solutes, because successful operation largely depends on the properties of the solvents and solutes, such as viscosity and heat of vaporization.

6.3.2 Solvent type influence

As mentioned in Section 4.3.2, employment of various solvents, water, ethanol, and acetone resulted in different particle morphology and productivity. Since all the processing parameters were fixed, evidently the morphology and productivity diversity of both as-sprayed micron and nano particles arose from the different solvent properties. In

SPS, when the droplets entered the plasma, the solvent vaporized in the first place, consuming a considerable proportion of the plasma enthalpy. As the heat of vaporization of water (2258 kJ/kg) is much higher than of ethanol (838 kJ/kg) and acetone (525 kJ/kg), at the same suspension concentration and feedrate, the water solvent consumed much more energy than the organic solvents. In addition, the organic solvent may be partially combusted and contributed to the plasma enthalpy. Hence, with the fixed plasma power, the enthalpy available for Y_2O_3 particles' melting and vaporization in water suspension spraying was much less than in organic system. This explains the quantity and size difference of micron-sized spherical particles in **Fig. 4.18** and the C3 productivity diversity. It can be seen from **Fig. 4.18** (b) and (c) that the size distribution of the micron-sized spherical particles from organic solvents was still wide. The reason for this wide size distribution is twofold, similar to powder feed spraying.

(i) The Y_2O_3 raw material had a wide particle size distribution and it can affect the final size distribution.

(ii) With a fixed size range and plasma conditions, particle melting and vaporization depends on the residence times linked to their velocity and trajectories within the plasma. When injected via an atomization injector, the suspension was atomized into numerous micron-sized droplets containing one or a few Y_2O_3 particles. At the exit of the injector, droplets exhibited velocity vectors that were not all parallel to the probe axis. Moreover, their size distribution induced a divergence of their momentum which was transferred from the atomization gas. This divergence increases when the mean particle size decreases, especially when it is below 20 μm in diameter [21]. Owing to their various trajectories and momentum, the particles were not heat-treated homogeneously by the plasma. For example, with the same injection velocity, large particles will cross the plasma plume easily whereas small ones will not, thereby the heat treatment they incur

will be different.

Determined by XRF, XRD (**Fig. 4.19**) and Rietveld refinement results (**Fig. 4.20**), the components in the sprayed particles by organic solvent SPS were cubic and monoclinic phase Y_2O_3, amorphous phase carbon, and a previously unknown substance $Y_2O_2C_2$. Apparently, carbon came from the decomposition of organic solvent at high temperature, as shown in Eq. (6-3) and (6-4). Owing to the high cooling rate, carbon formed an amorphous phase that was displayed in the TEM picture in **Fig. 4.21** (a). Since carbon was superfluous during spraying, $Y_2O_2C_2$ impurity could be formed through the reaction in Eq. (6-5).

Ethanol solvent: $C_2H_6O \rightarrow 2C + 6H + O$ (6-3)

Acetone solvent: $C_3H_6O \rightarrow 3C + 6H + O$ (6-4)

$2Y + 2O + 2C \rightarrow Y_2O_2C_2$ (6-5)

The small amount $Y_2O_2C_2$ impurity that formed at high temperature is isotypic to $La_2O_2C_2$, reported by Butherus and Eick in 1973 and 1976 respectively [102, 103]. The $Y_2O_2C_2$ was retained at room temperature since the high quenching rate could "freeze" the high-temperature equilibrium structure. It mixed homogeneously with Y_2O_3 particles, as deduced from EDX mapping results in **Fig. 4.22**, and caused the unusual dark color of the sprayed particles. As reported by our previous research [123], it was found that heat treatment was an effective method to remove the plasma-induced metastable phase. The carbon amorphous phase and $Y_2O_2C_2$ impurity could also be removed in the same way by annealing at 700°C for 6 h, with the size of the Y_2O_3 nanoparticle unaffected (**Fig. 4.21** (b) and (c)). According to our research [123], the reversed reaction of C→B phase transformation and the nanoparticle growth of rare earth oxides only happened above 1000°C.

Since both the carbon amorphous phase and carbon related $Y_2O_2C_2$ impurities resulted from the incomplete combustion and decomposition of organic solvents, a more efficient way to get rid of them is to introduce O_2 secondary gas into the plasma. The effect of O_2 introduction is dual. First, O_2 facilitated the complete combustion of the organic solvent, accompanied by giving out a large amount of enthalpy that is comparable to the plasma energy. Second, O_2 also helped with the particle melting and vaporization by providing an enhanced plasma enthalpy and enlarged heat-treatment zone (**Fig. 5.9** (c)) as well as a much lower plasma and particle velocity (**Fig. 5.7** (c) and (**Fig. 5.10** (c)). As demonstrated by modeling results and the discussion in Section 6.2.1, these effects can be attributed to the oxygen dissociation at about 4000 K in the torch and subsequent recombination in the chamber [124]. As a consequence, the change of plasma thermophysical properties accounts for the considerable particle morphology improvement and size reduction shown in **Fig. 4.24** and **4.23**. Further discussion on combustion-aided SPS will be given in Section 6.4.

6.3.3 Mechanism of nanoparticles formation

Substituting organic solvents for water caused a size reduction and distribution narrowing of the as-sprayed nanoparticles, and the effect was enhanced by introduction of O_2 plasma gas, as shown in **Fig. 4.23**. In terms of the heat of vaporization and heat of combustion of the solvents, the particle heat treatment level increased in the order of water→ethanol→acetone→(acetone+O_2), in accord with the order of particle size decreasing and size distribution narrowing (**Fig. 4.23**). Therefore, in addition to improving the morphology of micron-sized particles and the productivity of nanoparticles, plasma heat treatment conditions also affected the size of nanoparticles.

To elucidate the correlation between plasma conditions and size of nanoparticles, the mechanism of nanoparticle formation has to be addressed. It is in some ways different from the micron-sized particles formation mechanism because nanoparticles are formed by vapor phase homogeneous nucleation and nuclei growth. For the same material, the productivity of nanoparticles depends on the plasma enthalpy and how much the material vaporizes, while the size of nanoparticles depends on the supersaturation degree and quenching rate of the vapor phase [125]. The process of nanoparticle formation is shown schematically in **Fig. 6.3** and described as follows. In SPS, the droplets that carry particles are flash dried and the remaining micron-sized particles are heated. When the particles are heated over their vaporization temperature by the plasma, they start to vaporize and the partial pressure of vapor phase increases and eventually becomes saturated. In the upstream of the plasma plume, saturated vapor pressure is higher than vapor pressure because of the high plasma temperature. In the downstream, decreasing plasma temperature leads to a decrease in the saturated vapor pressure, resulting in supersaturation. Homogeneous nucleation takes place in a supersaturated condition. When the condensation kinetics permit, e.g. the vapor is cooled when moving downstream, the homogeneous nucleation will take place and large numbers of tiny primary nuclei will form instantaneously. Once nucleation occurs, the remaining supersaturation will be relieved by condensation on the surface of the primary nuclei, and nucleus growth will proceed rather than creation of more nuclei. With the vapor pressure quickly depleted and nucleation tapering off, a more prevalent process knows as coalescence begins, through which the nuclei collide due to Brownian motion and unite as clusters, i.e. nanoparticles. The particle size is largely determined by the collision and coalescence rate in this stage. With the temperature further decreasing, another process called coagulation arises, and

the ultrafine nanoparticles combine and form agglomerates. If the quenching is not fast enough and the temperature is still high, the nanoparticles will form hard agglomerates which cannot be fully re-dispersed. Otherwise, the particles will be bound together by Van der Waals forces to form loose agglomerates which can be re-dispersed by ultrasonic vibration into individual nanoparticles [126]. Indeed, there are some other factors that may affect the size of the nanoparticles, such as chamber pressure and injector position. But in this research, these parameters were fixed and only the influence from plasma enthalpy and quenching rate is discussed.

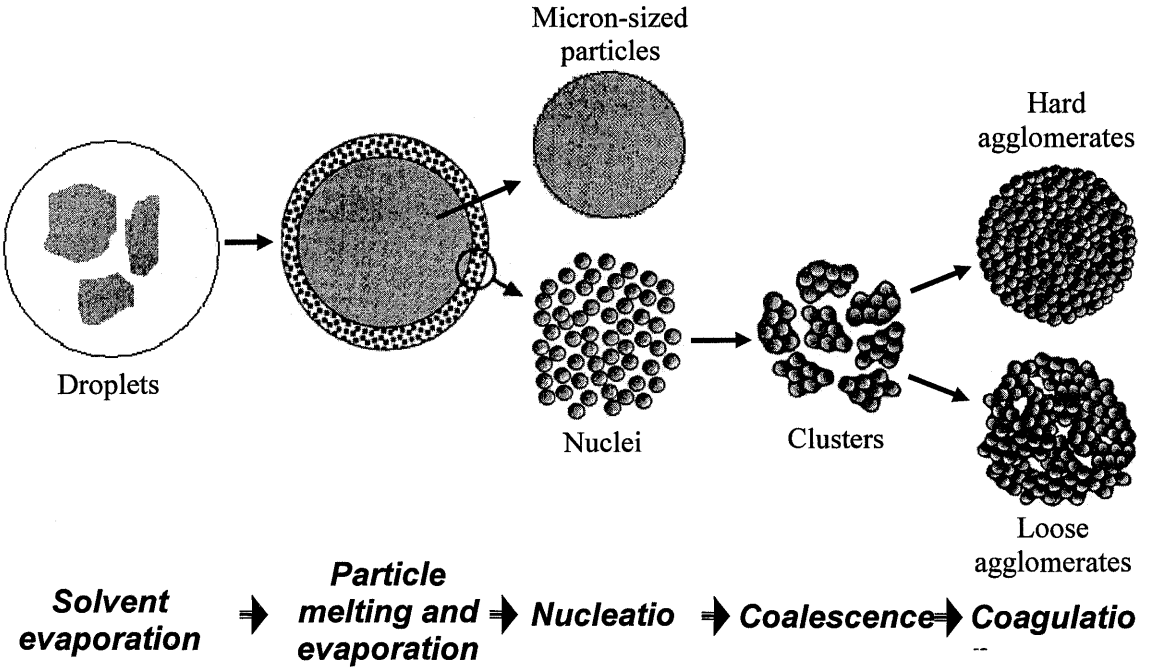

Fig. 6.3. Schematic procedure of nanoparticles formation in SPS

The nucleus diameter d_p produced from nucleation can be estimated from the Gibbs-Kelvin equation [127],

$$d_p = \frac{4\sigma v_1}{kT \ln S} \qquad (6\text{-}6)$$

where σ is the surface tension, k the Boltzmann constant, S the saturation ratio defined as the ratio of the partial pressure of the corresponding species to its saturation vapor

pressure, and v_1 the volume of monomer in the condensed phase. It can be seen that the higher the plasma temperature T and supersaturation ratio S, the smaller the nucleus size. Therefore, to synthesize ultrafine nanoparticles with uniform size, first of all, a high initial nucleus density, and a high supersaturation degree is needed. A high supersaturation degree leads to larger numbers of initial nuclei at the nucleation event, so that the succeeding vapor condensation can be distributed homogeneously to more nuclei. Thus, the individual nucleus growth is limited and the particle size deviation will be small. To achieve a high supersaturation degree, firstly, an enhanced plasma enthalpy or a low plasma velocity is required to increase the heat treatment level and material vaporization. According to Girshick [85, 128], if the vapor concentration is too high, the particle will overgrow to larger size. But in our research, the feedstock was quite dilute and the chamber was large, so that the over-high vapor concentration could not be achieved. Secondly, a sharp quenching is indispensable. Quenching rate is more crucial for controlling the particle size as it impacts both nucleation and succeeding in-flight particle growth. Having achieved sufficient vaporization and vapor pressure, the vapor phase still requires a sharp quenching to rapidly decrease its equilibrium vapor pressure and create a high supersaturation degree before the nucleation event can happen. Once nuclei form from nucleation, they collide and coalesce at a rate that is proportional to the square of their number concentration which is only weakly dependent on particle size [127]. A high quenching rate can shorten the coalescence time and lower the coalescence possibility, thus to restrain the nucleus growth. This is also applicable in the coagulation stage. During coagulation, according to Swihart's study [125], if the quenching rate is low and the temperature is high enough, the particle sinter faster than they coagulate, spherical nanoparticles, i.e. hard agglomerates, are produced. If the quenching rate is very high and the temperature not high enough for sintering, loose agglomerates with an open structure

are formed. At intermediate conditions, partially sintered non-spherical nanoparticles are produced. In our research, loose agglomerates were formed due to fast quenching.

For the nanoparticles from various solvents SPS in **Fig. 4.23**, the mean size decreased and size distribution narrowed in the order of water→ethanol→acetone solvent. The reason is twofold. On the one hand, the increasing plasma enthalpy that resulted from different solvent thermodynamic properties led to a higher degree of material vaporization. On the other hand, the quenching rate was also increased due to the plasma enthalpy elevation. The reason is as follows. When the average temperature of the plasma field increased, the temperature contour curve at which nucleation occurred moved closer to the chamber wall in both radial and axial directions. The chamber wall was at room temperature constantly because of the chamber water-cooling system. Hence, the distance between the nucleation temperature isotherm and ambient temperature isotherm was shortened, and the temperature gradient became steeper. With the same plasma velocity, the cooling rate could be higher. Consequently, the acetone solvent led to the highest quenching rate because of its highest plasma enthalpy and temperature, followed by ethanol and water. In another word, plasma enthalpy elevation was responsible for the particle size diversity in **Fig. 4.23** because it increased both supersaturation degree and quenching rate. This phenomenon has also been discovered in the plasma modeling work done by Desilets et al [91] in 1997. They reported that higher power caused a greater temperature gradient, especially for the radial quenching of the vapor flow, which is more important for a uniform particle size.

As for the powder feed spraying by Ar/O_2, modeling results in Chapter 5 show that O_2 addition elevated the volume average temperature (617 K → 2410 K), i.e. the plasma

enthalpy significantly. Hence both supersaturation degree and cooling rate were increased. Moreover, the plasma plume became broader and longer (0.02×0.15 m → 0.05×0.3 m) and the starting plasma velocity almost halved (400 m/s → 250 m/s) after O_2 addition, both of which literally prolonged the particle residence time in the high-temperature zone thereby advanced the vaporization and supersaturation degree. Although a lower plasma velocity and thereby a lower particle velocity may reduce the quenching rate to some extent, it can be compensated by the substantial increase of quenching rate due to enlarged plasma plume volume. As shown in the modeling contour in **Fig. 5.4**, the isotherm of Ar/O_2 plasma diffusion zone with a temperature above the melting points of Sm_2O_3 (≈ 2600 K) is much closer to the chamber wall than Ar plasma, especially in the radial direction. Since the wall was constantly at room temperature, an increased temperature gradient was generated close to the wall, thus the quenching rate was increased substantially. Combining all these effects caused by O_2 introduction, the mean size of the nanoparticles decreased and the distribution narrowed (**Fig. 4.11**).

In the case of combustion-aided SPS, modeling results reveal that the starting plasma velocity decreases dramatically (20 m/s) and the volume average temperature is higher (2627 K) than Ar/O_2 plasma. Besides this, the shape of the plasma plume also became shorter and broader (0.06×0.25 m). This is because the chemical reaction between acetone and oxygen contributed to the plasma enthalpy, but in the meantime interfered with the momentum transfer from plasma species to particles. Although the shorter plume might reduce residence time slightly, it could be safely compensated by the lower plasma velocity. However, a lower plasma velocity, in turn, would lead to a lower quenching rate which increases particle size. This negative effect was overcome by the further enlarged plasma plume and elevated plasma enthalpy. In combustion-aided plasma, the plume is

shorter and broader, which means the higher enthalpy was confined more at the upper part of the chamber. This will cause a much sharper temperature gradient (**Fig. 5.5**) and faster quenching rate close to the upper chamber wall, taking into account the fact that the radial direction has more impact on the quenching rate [91]. As a whole, the quenching rate was still high enough to induce a high degree of supersaturation, which explains the significant nanoparticle size decreasing and narrowing in **Fig. 4.23**.

6.4 Effects of combustion-aided SPS and comparison of various spraying schemes

6.4.1 Combustion-aided SPS effects on particle morphology and productivity

R_2O_3 water and acetone solvent SPS by Ar and Ar/O_2 plasma were carried out and the resulting particle morphology, productivity, and crystal structure were compared. In SPS, C1 collected mostly micron-sized particles and C2 contained mainly nanoparticles. For the four spraying schemes, it was discovered that (Ar + water) provided the lowest heat treatment level for particles, followed by (Ar/O_2 + water) and (Ar + acetone). (Ar/O_2 + acetone), i.e. the combustion-aided SPS, had the highest heat treatment level. This heat treatment difference is typified by the morphology of micron-sized particle and nanoparticle productivity. Taking Dy_2O_3 as an example, the micron-sized particle morphology of (Ar/O_2 + water) and (Ar + acetone) in **Fig. 4.25** (b) and (c) shows a minor improvement compared with that of (Ar + water) in **Fig. 4.25** (a), whereas the combustion-aided SPS in **Fig. 4.25** (e) exhibits a significant improvement. In addition, the C2 productivities of these four schemes (**Fig. 4.29**) clearly indicate that combustion-aided SPS produced many more nanoparticles than the rest of the schemes for each sprayed oxide, though errors may exist in some data because of the loss during particle collection. These effects can be attributed to the diverse plasma enthalpy of various schemes. As

discussed in previous sections, water has a much higher heat of vaporization and consumes a larger proportion of plasma enthalpy than acetone, thus (Ar + acetone) had a better heat treatment result than (Ar + water). O_2 addition, despite being a great contribution to plasma enthalpy in the combustion-aided case, could not counteract the negative influence caused by water. Hence, the result of (Ar/O_2 + water) is better than (Ar + water) but worse than (Ar/O_2 + acetone). The remarkable improvement in particle morphology and productivity by combustion-aided SPS can be attributed to the elevated plasma enthalpy caused by O_2 recombination and acetone combustion. The considerable contribution of O_2 recombination to plasma enthalpy has been discussed for powder feed spraying in Section 6.2. In combustion-aided SPS, besides the O_2 effect, the combustion of acetone solvent also contributed considerably to the enthalpy. Acetone solvent was flash vaporized and combusted when fed into the plasma field. The combustion reaction is formulated as

$$C_3H_6O + 4O_2 \rightarrow 3CO_2 + 3H_2O + 29000\ kJ/kg \qquad (6\text{-}7)$$

Although acetone vaporization consumed some plasma enthalpy, the plasma enthalpy and particle heat-treatment were still increased dramatically because acetone's heat of combustion (29000 kJ/kg) is two orders higher than its heat of vaporization (525 kJ/kg) and is comparable to the plasma energy. Owing to this additional combustion reaction, its plasma plume (**Fig. 5.5**) became broader and shorter and its volume average temperature was even higher than Ar/O_2 plasma. In addition, its plasma velocity was largely reduced due to the interference in the momentum transfer caused by the chemical reaction. The combination of the above effects offered a more enhanced heat treatment and faster quenching conditions than the Ar/O_2 plasma, and therefore yielded better results.

For different rare earth oxides, their as-sprayed particles reflected the trends associated

with their thermodynamic properties. As examples, the morphology of micron-sized particles from combustion-aided SPS in **Fig. 4.25** (d), (e), and (f), the nanoparticle mean size in **Fig. 4.28**, and the productivities in **Fig. 4.29** all show the same sequence of $Sm_2O_3 \rightarrow Dy_2O_3 \rightarrow Lu_2O_3$ as in Section 6.1.2. The nanoparticles from combustion-aided SPS with diameters below 100 nm are monocrystallites in various shapes and loose agglomerates, as shown in **Fig. 4.26** and **4.27**. This is because the particle growth was frozen at the coalescence stage by the fast quenching, so only loose agglomerates could be formed. The ultrafine nanoparticles observed by TEM were not detected after DLS due to the agglomeration.

6.4.2 Comparison of various spraying schemes

To achieve a comprehensive understanding of the processing conditions' influence on RF-ICP spraying, in this section, an overview of all the spraying schemes and their impact on spraying results has been written.

6.4.2.1 Particle morphology and productivity

The particle morphology and nanoparticle productivity are directly related to the heat treatment level and quenching rate. As discussed before, to achieve a smaller particle size and narrow size distribution at a high productivity, a uniformly distributed, high-enthalpy plasma field is preferred. In powder feed sprayings, this was realized by O_2 introduction as demonstrated by modeling results in Chapter Five. Experimental results show that the morphology of micron-sized as-sprayed particles (**Fig. 4.10** (b) and (c)) and the nanoparticle size distributions (**Fig. 4.11**) and productivities (**Fig. 4.13**) of powder spraying by Ar/O_2 plasma have been improved considerably in comparison with powder spraying by Ar plasma. But this method still had the problems of clogging and insufficient

heat treatment. So, the SPS method was adopted. However, the results of water solvent SPS turned out to be worse than powder spraying by Ar, even with the introduction of O_2 secondary gas. Substituting organic solvent for water solvent did not yield much improvement, but induced carbon-related impurities. Finally, combustion-aided SPS was developed by spraying acetone solvent SPS in Ar/O_2 plasma. Consequently, the particle morphology, productivity, and nanoparticle size distribution were improved dramatically, as shown in **Fig. 4.24**, **4.29**, and **4.23**. Comparing the results of Y_2O_3 from power and suspension spraying by Ar/O_2 in **Table 6.2**, the latter had a smaller nanoparticles' mean size with narrower size distribution, and a higher productivity. This is associated with its more favorable plasma enthalpy, plume distribution, and quenching rate for the synthesis of nanoparticles. Therefore, combustion-aided SPS is the most efficient way for plasma spraying synthesis of rare earth oxide nanoparticles.

Table 6.2. Comparison of Y_2O_3 C3 nanoparticles from powder spraying by Ar/O_2 and combustion-aided SPS

Scheme	*Nanoparticles' mean size (nm)*	*Standard deviation (nm)*	*Productivity (%)*
Powder spraying by Ar/O_2	20	5.3	5.9
Combustion-aided SPS	14	3.5	7.1

6.4.2.2 Crystal structure

For all the oxides studied, they exhibited an inclination for C→B phase transformation induced by plasma treatment, and the transformation degree varied with materials and processing conditions. The C→B phase transformation was induced by high temperature during spraying and retained at room temperature due to fast quenching. Basically, the heat treatment level increased across C1→C2→C3 particles, so the phase transformation degree increased in the same order for a certain oxide and fixed spraying conditions. For different oxides under the same spraying conditions, the transformation degree was

related to the thermodynamic properties, i.e. the melting and vaporization point of the oxide. The higher the thermodynamic stability of the oxide, the lower was the transformation degree. In this section, we are mainly concerned about the crystal structure change induced by processing conditions. As shown in **Fig. 4.30** to **Fig. 4.33**, the C→B phase transformation occurred for both C1 and C2 particles when the oxide powders were treated by Ar plasma. Introduction of O_2 in powder spraying increased the transformation degree, except that the increase was too small to be detected for the Sm_2O_3 and Lu_2O_3 cases. For the SPS, all the spraying schemes, even combustion-aided SPS, had a lower C→B transformation degree than powder spraying. This is contrary to expectations if the phase transformation degree is correlated only to plasma enthalpy, because the modeling results show that combustion-aided SPS has higher enthalpy than powder spraying by Ar/O_2, and therefore should have higher transformation degree. In view of the high reliability of phase determination by Rietveld refinement, it can be deduced that the C→B phase transformation degree is dependent not only on heat treatment level but on some other factors too. Combustion-aided SPS, somehow, restricted the C→B transformation to some extent. This may be attributed to the combustion reaction and its byproducts, because O_2 plasma spray did not show this phenomenon, and the only difference between them is the combustion. The combustion occurred immediately after the mixing of acetone and oxygen in the torch zone. After that, eue to the very high temperature in the torch, the products CO_2 and H_2O would partially decompose into C, O, and H. When they moved downstream, the temperature dropped, and H_2O and CO started to form. When the temperature dropped below 5000˚C, CO_2 started to form [129]. This process is formulated by Eq. (6-8).

$$C_3H_6O + O_2 \rightarrow CO_2 + H_2O \rightarrow C + O + H \rightarrow CO + O + H_2O \rightarrow CO_2 + H_2O \quad (6\text{-}8)$$

Since rare earth sesquioxides are thermodynamically unstable against hydration and

carbonation [130, 131], they are much more liable to react with CO_2 and H_2O at room temperature. Although, in the plasma, the temperature was too high to form any rare earth carbonate or hydroxide, the interaction between the combustion byproducts and oxide could still interfere the oxygen loss and structure reconstruction process of rare earth oxide, thus restrict the C→B phase transformation to some extent.

In addition, the unit cell volumes of both cubic and monoclinic structure exhibited a strong correlation with plasma heat treatment level. As can be seen from **Fig. 4.30** to **4.33**, the volumes decreased with increasing plasma enthalpy and heat treatment level. There may be some errors caused by the Rietveld refinement affecting individual data, but the unit cell contraction tendency induced by heat treatment was quite clear. It has to be noted that the unit cell contraction degree is not correlated with phase transformation degree though it is also caused by crystal structure change. This can be justified by the Lu_2O_3 case in **Fig. 4.33** where the cubic unit cell varied while the oxide maintained the pure cubic phase structure. Indeed, the unit cell contraction represented those unit cells in the process of a C→B transformation or B→A transformation. As mentioned before, rare earth oxides tend to transform across C→B→A structures when temperature increases. During transformation, the unit cells started to lose oxygen atoms and contract due to reconstruction of coordination bonds and cations moving closer to each other. After plasma treatment, those unit cells that finished transformation were identified as a new phase, whereas those in the process of a reconstruction were frozen at room temperature and characterized as unit cell contraction. If we compare the cubic unit cell contraction with the volume difference between the cubic and monoclinic unit cell, the contraction extent was tiny. This signifies that the cubic unit cells were only slightly distorted and at the beginning of the reconstruction. However, the unit cell contraction can still be considered as a rough indication for the plasma heat treatment level. For instance, in all

oxides, both powder spraying by Ar/O_2 and combustion-aided SPS cases showed the smallest unit cell volumes, suggesting a higher heat treatment level, which has been proved to be the case by modeling and experimental results.

6.5 Crystallography of plasma synthesized $Sm_{2-x}Lu_xO_3$ nanoparticles

As for the XRD patterns of sintered pellets series, at the Sm-rich region (x=0 to 0.6), the B-type monoclinic phase was present in all the five patterns (**Fig. 4.38**). All the Bragg reflections shift to higher angles with the Lu fraction increasing from x=0 to 0.6, indicating a decrease in the unit cell dimension of the monoclinic phase. This is because the ionic radius of Lu is smaller than Sm. Additionally, there is a metastable phase represented by the double peaks at around 28.4°. Its intensity seems to have no correlation with the Lu fraction, in some patterns it is pronounced, while in others it is not. Since no relevant structure information is available, the structure and amount of this phase is unable to be determined. The reason this additional phase is metastable and not caused by contamination is that after grinding, it totally disappears (**Fig. 4.39**). A possible explanation for the formation of this metastable phase is that a structure closely related to B-type monoclinic is induced by the grain strain generated during sintering. After grinding, due to the release of the strain, the phase transforms to B structure and disappears. In the Lu-rich region (x=1.2 to 2.0), the known C-type cubic solid solution presents in all patterns. With Lu fraction increase, the peaks also shift to high angles owing to the decreasing unit cell volume. Besides, a second metastable phase occurs in the pattern of $Sm_0Lu_2O_3$, which is different to the one in Sm-rich region. Its structure and amount remains unknown, and it disappears after grinding, too (**Fig. 4.39**). Furthermore, in the pattern of $Sm_{0.8}Lu_{1.2}O_3$, a third metastable phase is found, represented by the main Bragg reflections at 28.7° and 30.7°. In the middle region (x=1.0 and 1.2), the B and C

solid solutions mentioned above coexist. The ratio of B and C solid solution changes with the Lu fraction, while the ratio of Sm/Lu in each solid solution never changes in the region, as the B and C phases in this region have fixed Sm/Lu compositions determined by the border Sm/Lu compositions. Thus, the unit cell parameters and volumes of each phase should be constant. This has been confirmed by refinement. In addition, the third metastable phase is also discovered in the middle region, with the same reflections as the metastable phase in $Sm_{0.8}Lu_{1.2}O_3$.

The situation for the ground powders group is much simpler than for pellets. The phases present in Sm-rich, Lu-rich, and the middle regions are B-type monoclinic solid solution, C-type solid solution and both of them, respectively, which is in accord with Schneider and Roth's study. Nevertheless, the width and position are different according to our calculation. By refinement, the lattice parameters and unit cell volumes of each composition of $Sm_{2-x}Lu_xO_3$ have been determined. Using simple mathematical extrapolation, the border of the middle region has been recalculated and shown in **Fig. 4.41** (b), with the left border at x=0.68 and right border at x=1.06 approximately. Three more pellet and ground powder samples with the compositions of two borders and midpoint were prepared and their XRD patterns fit into both the pellet and ground powder pattern series very well (**Fig. 4.38** and **4.39**). But the two border samples are still slightly within the middle region since there are still both B and C phase solid solution occur.

As for the sprayed powder group, the phase composition can be clearly displayed using the phase diagram in **Fig. 4.41** (c). After spraying, the phase diagram has the same distribution of the three regions as in the ground powder phase diagram before spraying. The only difference is the presence of a new B-type monoclinic phase solid solution in the middle region and Lu-rich region, which can be observed in the XRD patterns of x=0.8 to

1.8 in Fig. 4.16. The structure of this new monoclinic phase is quite similar as the original one, but its unit cell volume is a little smaller, suggested by a small shift of the Bragg reflections. Determination of phase composition is difficult because of the similarity of the two monoclinic structures. This new monoclinic phase induced by plasma spraying is considered to be the consequence of a C→B phase transformation because its unit cell volume is between those of the original monoclinic and cubic phase. A similar C→B phase transformation occurs in the spraying of the single rare earth oxide. It seems that the B structure which transforms from the C structure at high temperature in the plasma is frozen and retained at room temperature due to the high cooling rate. This B structure is stable at ambient temperature, and shows no reversion to C structure after an annealing treatment at 400°C.

Chapter Seven: Conclusions and Future Work

7.1 Conclusions

In the present research, inductively coupled RF plasma spraying was employed to synthesize rare earth oxide nanoparticles. Commercial micron-sized rare earth oxide powders of Y_2O_3, Sm_2O_3, Dy_2O_3, and Lu_2O_3 were used as raw materials. Powder feed spraying and suspension feed spraying with various solvents by Ar and Ar/O_2 plasma were adopted to synthesize single rare earth oxide nanoparticles. In addition, nanoparticles of rare earth mixed-oxide series $Sm_{2-x}Lu_xO_3$ was synthesized through powder feed spraying with Ar plasma. The resulting particles' morphology, productivity, and crystal structure were studied and correlated with processing conditions and modeling results. Finally, the following conclusions could be drawn based on the experimental and modeling results:

(i) Modeling of combustion-aided suspension plasma spraying was carried out for the first time. According to the modeling results, the plasma volume average temperatures of different schemes increased in the sequence of Ar→Ar/O_2→(Ar/O_2+acetone), and their plasma velocities decreased in the same order. The plasma field was substantially altered by the introduction of O_2 secondary gas and the combustion of acetone solvents. The plasma plume was prolonged and broadened and the volume average temperature was elevated dramatically. In addition, the plasma velocity and thereby the entrained particles' velocity decreased remarkably. Therefore, plasma with O_2 addition and acetone combustion could provide rare earth oxide particles with an enhanced and more homogeneous heat treatment.

(ii) For all spraying schemes, due to the classification function of the collectors, the

average size of the collected particles decreased across chamber C1→C2→C3. In addition, because of the thermodynamic properties diversity for the different rare earth oxides, the mean sizes of the nanoparticles obtained increased in the sequence of Sm_2O_3→Dy_2O_3→Lu_2O_3, and their productivities decreased in the same order.

(iii) In the scheme of powder feed spraying by Ar plasma, the micro-sized rare earth oxide particles formed consisted of both spherical and irregular shapes, suggesting an insufficient heat treatment. Moreover, they had a wide size distribution which arose from the raw materials and the inhomogeneous heat treatment. The productivity of the nanoparticles was quite low.

(iv) The situation in Ar plasma spraying was significantly improved using powder feed spraying by Ar/O_2 plasma. The O_2 dissociation and recombination process changed the plasma plume shape, elevated the plasma enthalpy, and prolonged the particles residence time. The quenching rate was also increased. Consequently, the morphology of the as-sprayed micron-sized particles was improved greatly, and the nanoparticles' mean size became smaller and the size distribution became narrower. Furthermore, the productivity of the nanoparticles was doubled compared with Ar plasma.

(v) Water solvent SPS by Ar plasma was efficient in solving the clogging problem which occurred in powder feed sprayings. However, the water solvent consumed a large proportion of the enthalpy for its evaporation, thus the particles obtained were even worse than from powder sprayings. Substituting organic solvents for water did improve the results, but they still cannot compare with those of powder spraying. What is more, the organic solvents caused some carbon-related impurities, which had to be removed by post-spraying heat treatment.

(vi) Combustion-aided SPS developed in this research has proved to be the best way to synthesize rare earth oxide nanoparticles. On account of the dual effects of O_2

recombination and acetone combustion, the particles underwent an even higher level heat treatment than powder spraying by Ar/O_2. The quenching rate was increased further. As a result, the particle morphology was improved dramatically, the nanoparticles' size became smaller and distribution became narrower than those of powder spraying by Ar/O_2. The nanoparticles' productivity increased further. At last, Y_2O_3 nanoparticles with a mean size of 14 nm and a standard deviation of 4.5 nm were able to be produced at a rate of 8.4 g/h. The nanoparticles were well-dispersed with various shapes.

(vii) All the sprayed oxide particles exhibited an inclination towards cubic to monoclinic (C→B) phase transformation induced by the plasma treatment, the degree of which varied with material and processing conditions. Basically, the C→B phase transformation degree increased across C1→C2→C3 particles. The degree also increased when the processed oxide has lower thermodynamic stability. Normally, the higher the heat treatment degree and the lower the thermodynamic stability, the higher the C→B phase transformation degree. Nevertheless, in our sprayings, the C→B phase transformation degree was not determined by these two factors only. In some cases such as powder spraying by Ar/O_2 and combustion-aided SPS, the C→B phase transformation could be restricted by oxygen atmosphere or combustion products.

(viii) RF plasma spraying of sintered $Sm_{2-x}Lu_xO_3$ is a viable approach to produce mixed oxide nanoparticles. These mixed oxides consisted mainly of monoclinic B-type and cubic C-type solid solution phases. The particles showed a wide size distribution. The larger particles had spherical shape, ranging from submicron to micron size, whereas the ultra-fine particles were crystallites with a size less than 100 nm in various shapes. The refined XRD pattern showed that in the sintered pellets pattern group, in addition to the B and C type solid solutions, three different metastable phases were present,

which disappeared after grinding of the pellets into powders. In the ground powder group, the phase composition was in agreement with that reported by previous researchers, with a B type solid solution in the Sm-rich region, a C-type solid solution in the Lu-rich region, and mixed in the middle region. However, by refinement of the lattice parameters and extrapolation, it was found that the position of the middle region in the Sm_2O_3-Lu_2O_3 phase diagram shifts to the left and the peak width is wider in this study. In the sprayed powder group, the phase diagram is similar to that of ground powder, except that a new B-type monoclinic phase occurs in the middle region and Lu-rich regions. This new B structure is probably a consequence of a C→B transformation induced by plasma treatment, after which the B structure is subsequently retained by the extremely high cooling rate. The new B structure is stable at ambient temperature, and shows no re-conversion to the C structure under an annealing treatment at 400°C.

7.2 Future work

In the modeling work of RF-ICP spraying in this research, the conventional constant volumetric heat source model was adopted to represent the plasma heat generation. Therefore, plasma characteristics such as Lorentz flow were not modeled. To remedy this defect, Maxwell's equations should be incorporated in the model to represent the electromagnetic field [77]. The induction electromagnetic fields can be represented using the electromagnetic vector potential to consider the interaction between the applied electromagnetic field of the coils and the induction electromagnetic field of the plasma [93]. The nanoparticle formation was not modeled in this research either because of software limitation. This can be realized by using more powerful software for the modeling of combustion-aided SPS in the future, such as SIMPLER algorithm [68].

Aerosol growth model, presented by Girshick et al. [128], can be applied to account for the nucleation and growth, taking into account homogeneous nucleation, surface condensation, Brownian, coagulation, radial diffusion and thermophoresis phenomena. In our modeling, the torch efficiency was estimated and fixed at 67% for all three cases. However, the efficiency might vary with plasma gases and feeding methods, which can be roughly calculated through the torch and injector cooling water temperature variation. By correcting the torch efficiency value, the heat source generation representation could become more reliable.

In the modeling, several assumptions were made to simplify the computational task. For example, oxygen molecules were assumed to be fully dissociated and recombined, and the ionization process of O atoms was not considered. This is not totally correct because dissociation and recombination reactions could not proceed completely at anytime due to their reverse reactions. O atom ionization was always present in the plasma and contributed to the plasma enthalpy variation. So far, the dissociation and recombination rate of O_2 and the ionization rate of O can only be estimated by empirical equations and are inaccurate. If in the future more reliable data can be obtained by measurement and input into the model, the modeling results would be in greater accord with the realistic situation.

For the experiment part, powder feed spraying was limited by the bad flowability of its feedstock, although its results were comparable with combustion-aided SPS. Besides, combustion-aided SPS is easier and more flexible in the introduction of gases and reactants, thus, it can be used for reactive plasma spraying and has great potential in a wide range of industrial applications. Since combustion-aided SPS was developed and

applied in this research for the first time, the process is far from mature. Only acetone and O_2 was used in our spraying, and the processing parameters such as plasma power, chamber pressure, probe position, and gas flowrate were not optimized. In future research, further work could be conducted on exploration of more efficient suspension solvents and plasma gases or optimization of the processing parameters, aiming at further improvement of the processing capacity and flexibility. In our spraying, the plasma power has reached its limit. Certainly, if the plasma energy can be elevated by upgrading the power supply system, the process would be more suited to tackle refractory materials like rare earth oxides.

The rare earth oxide nanoparticles synthesized by combustion-aided SPS were much better than the conventional plasma spraying method. The results were still not perfect because the nanoparticles were not totally spherical and the diameter of the nanoparticles may be reduced further. To further improve the nanoparticles's yield, size distribution, and shape, tangential injection of cooling gas can be applied combined with combustion-aided SPS. Employment of tangentially injected cooling gas has proved to be an efficient way to increase the quenching rate, thereby controlling the nanoparticles' yield and size [93, 132]. According to Swihart [125], a proper quenching rate may produce spherical nanoparticles if the coalescence process is faster than coagulation. Although it is very hard to control precisely the quenching rate with current techniques, it should be the final goal for plasma spraying to produce nanoparticles with controlled size and morphology. As combustion-aided SPS has shown its ability to alter the plasma's thermophysical properties and increase the quenching rate, it may be possible to manipulate multiple factors of SPS and injected cooling gas to control the plasma temperature distribution and quenching rate as required.

References

1. Bernardi, J., Schrefl, T., Fidler, J., Rijks, T., Kort, K.d., Archambault, V., Péré, D., David, S., Givord, D., O'Sullivan, J.F. *et al.* (2000) Preparation, magnetic properties and microstructure of lean rare-earth permanent magnetic materials *Journal of Magnetism and Magnetic Materials* **219,** 186-198.
2. Williams, D.K., Bihari, B., Tissue, B.M. and McHale, J.M. (1998) Preparation and fluorescence spectroscopy of bulk monoclinic Eu^{3+}:Y_2O_3 and comparison to Eu^{3+}:Y_2O_3 nanocrystals. *Journal of Physical Chemistry B* **102,** 916-920.
3. Xian, L.X., He, C.W. and Ming, X.M. (2006) Preparation of nano Y_2O_2S : Eu phosphor by ethanol assisted combustion synthesis method. *Journal of Rare Earths* **24,** 20-24.
4. Ronda, C.R., Ju¨stel, T. and Nikol, H. (1998) Rare earth phosphors: fundamentals and applications. *Journal of Alloys and Compounds* **275-277,** 669–676.
5. Kishi, H., Kohzu, N., Sugino, J., Ohsato, H., Iguchi, Y. and Okuda, T. (1999) The effect of rare-earth (La, Sm, Dy, Ho and Er) and Mg on the microstructure in $BaTiO_3$. *Journal of the European Ceramic Society* **19,** 1043-1046.
6. Laha, A., Fissel, A., Bugiel, E. and Osten, H.J. (2007) Epitaxial multi-component rare earth oxide for high-K application. *Thin Solid Films* **515,** 6512-6517.
7. Boulay, D.D., Ishizawa, N. and Maslen, E.N. (2004) $GdAlO_3$ perovskite. *Acta Crystallographica* **C60,** 120-122.
8. Jha, P. and Ganguli, A.K. (2004) Complex rare-earth titanates with the perovskite structure: Rietveld studies and dielectric properties *Solid State Sciences* **6,** 663-671.
9. Gschneidner, K.A. (1981) Industrial applications of rare earth elements. *ACS Symposium* American Chemical Society, Washington D.C., Vol. Series 164.
10. Huang, X.H., Zhong, Q. and Zhang, G.S. (2005) Advances on Rare Earth Application in Pollution Ecology. *Journal of Rare Earths* **23,** 5-11.
11. Molycorp, I. (1994) *A lanthanide lanthology, part II.* Molycorp Inc., CA, USA.
12. Okuyama, K. and Lenggoro, I.W. (2003) Preparation of nanoparticles via spray route. *Chemical Engineering Science* **58,** 537-547.
13. Trojan-Piegza, J., Zych, E., Hreniak, D., Strek, W. and Kepinski, L. (2004) Structural and spectroscopic characterization of Lu_2O_3: Eu nanocrystalline

spherical particles. *Journal of Physics: Condensed Matter* **16,** 6983-6994.

14. Chakka, V.M., Altuncevahir, B., Jin, Z.Q., Li, Y. and Liu, J.P. (2006) Magnetic nanoparticles produced by surfactant-assisted ball milling. *Journal of Applied Physics* **99,** 1-3.
15. Cai, C., Hänisch, J., Hühne, R., Stehr, V., Mickel, C., Gemming, T. and Holzapfel, B. (2005) Structural and magnetotransport properties of $YBa_2Cu_3O_{7-\delta}/Y_2O_3$ quasimultilayers. *Journal of Applied Physics* **98,** 1-6.
16. Kishi, H., Mizuno, Y. and Chazono, H. (2004) Base-metal electrode-multilayer ceramic capacitors: past, present and future perspectives. *AAPPS Bulletin* **14,** 2-18.
17. Gschneidner, K.A., Kippenhan, N. and McMasters, O.D. (1973) *Thermochemistry of the rare earth*. Rare-Earth Information Center, Iowa State University, USA.
18. EI-Kaddah, N. (1992) *Thermal plasma applications in materials and metallurgical processing*. Minerals, Metals & Materials Society, Warrendale, Pa.
19. Castillo, I.A. and Munz, R.J. (2005) Inductively coupled plasma synthesis of CeO_2-based powders from liquid solutions for SOFC electrolytes. *Plasma Chemistry and Plasma Processing* **25,** 87-107.
20. Sun, X.L., Tok, A.I.Y., Boey, F.Y.C., Gan, C.L. and Schreyer, M.K. (2007) Solvent and plasma gas influence on the synthesis of Y_2O_3 nanoparticles by suspension plasma spraying. *Journal of Materials Research* **In press**.
21. Fauchais, P. (2004) Understanding plasma spraying. *Journal of Physics D: Applied Physics* **37,** R86-R108.
22. Gschneidner, K.A. and Eyring, L.R. (1979) *Handbook on the physics and chemistry of rare earths*. North-Holland, Amsterdam.
23. Adachi, G., Imanaka, N. and Kang, Z.C. (2004) *Binary rare earth oxides*. Kluwer Academic Publishers, Netherland.
24. Gschneidner, K.A. and Eyring, L. (1966) A study of the polymorphism of rare earth sesquioxides at high temperatures. *M.Foex and J.P.Traverse, Bull. Soc. Fr. Mineral Cristallog.* **89,** 184.
25. Eyring, L. and Holmberg, B. (1963) *Advances in chemistry series*. American Chemical Society, Washington DC.
26. Adachi, G. and Imanaka, N. (1998) The Binary Rare Earth Oxides. *Chemical Reviews* **98,** 1479-1514.
27. Ronda, C.R., Jüstel, T. and Nikol, H. (1998) Rare earth phosphors: fundamentals

and applications. *Journal of Alloys and Compounds* **669,** 275-277.

28. Forlani, O. and Rossini, S. (1992) Rare earths as catalysts for the oxidative coupling of methane to ethylene. *Materials Chemistry and Physics* **31,** 155.

29. Tok, A.I.Y., Luo, L.H., Boey, F.Y.C. and Ng, S.H. (2005) Consolidation and properties of $Gd_{0.1}Ce_{0.9}O_{1.95}$ nano-particles for SOFC electrolytes. *Journal of Materials Research* **21,** 119.

30. Miao, Y.M., Zhang, Q.L., Yang, H. and Wang, H.P. (2006) Low-temperature synthesis of nano-crystalline magnesium titanate materials by the sol-gel method. *Materials Science and Engineering* **B128,** 103-106.

31. Wang, F., Fan, X.P., Pi, D.B. and Wang, M.Q. (2004) Hydrothermal synthesis of Nd^{3+}-doped orthoborate nanoparticles that emit in the near-infrared. *Journal of Solid State Chemistry* **177,** 3346-3350.

32. Zhang, R.B. and Gao, L. (2002) Preparation of nanosized titania by hydrolysis of alkoxide titanium in micelles. *Materials Research Bulletin* **37,** 1659-1666.

33. Gaertner, G.F. and Miquel, P.F. (1993) Review of ultrafine particle generation by laser ablation from solid targets in gas flows. *Nanostructured Materials* **4,** 559-568.

34. Jossen, R., Mueller, R., Pratsinis, S.E., Watson, M. and Akhtar, M.K. (2005) Morphology and composition of spray-flame-made yttria-stabilized zirconia nanoparticles. *Nanotechnology* **16,** 609-617.

35. Sun, X.L., Tok, A.I.Y., Boey, F.Y.C. and Huebner, R. (2006) RF plasma processing of untrafine Sm-Lu mixed oxide powder. *International Journal of Nanoscience* **5,** 487-491.

36. Alvero, R., Bernal, A., Carrizosa, I., Odriozola, J.A. and Trillo, J.M. (1987) Lanthanide oxides: thermochemical approach to hydration. *Journal of Materials Science* **22,** 1517-1520.

37. Akinc, M. and Sordelet, D. (1987) Preparation of yttrium, lanthanum, cerium and neodymium carbonate particles by homogeneous precipitation. *Advanced Ceramic Materials* **2,** 232-238.

38. Flores-Gonzaleza, M.A., Lebboua, K., Bazzia, R., Louisa, C., Perriatb, P. and Tillementa, O. (2005) Eu^{3+} addition effect on the stability and crystallinity of fiber single crystal and nano-structured Y_2O_3 oxide. *Journal of Crystal Growth* **277,** 502-508.

39. Skandan, G., Hahn, H. and Parker, J.C. (1991) Nanostructured Y_2O_3: synthesis and

relation to microstructure and properties. *Scripta Metallurgica et Materialia* **25,** 2389-2393.

40. Skandan, G., Foster, C.M., Frase, H., Ali, M.N., Parker, J.C. and Hahn, H. (1992) Phase characterization and stabilization due to grain size effects of nanostructured Y_2O_3. *Nanosturctured Materials* **1,** 313-322.

41. Zhang, Z.K. and Cui, Z.L. (1994) Phase structure in n-Y_2O_3. *Nanostructured Materials* **4,** 823-831.

42. Okuyama, K. and Lenggoro, I.W. (2003) Preparation of nanoparticles via spray route. *Chemical Engineering Science* **58,** 537-547.

43. Suzuki M., Kagawa M., Syono, Y. and Hirai, T.J. (1992) Synthesis of ultrafine single-component oxide particles by the spray-ICP technique. *Journal of Materials Science* **27,** 679-684.

44. Roth, J.R. (1995) *Industrial plasma engineering, Vol 1*. Institute of Physics Publishing.

45. Chen, F.F. and Chang, J.P. (2003) *Lecture notes on principles of plasma processing*. Kluwer Academic/Plenum Publishers, New York.

46. Bellan, P.M. (2006) *Fundamentals of plasma physics.* Cambridge University Press.

47. Fridman, A. and Kennedy, L.A. (2004) *Plasma physics and engineering.* Taylor & Francis.

48. Reed, T.B. (1961) Induction-coupled plasma torch *Journal of Applied Physics* **32,** 821-824.

49. Savkar, S.D. and Siemers, P.A. (1989) Workshop on industrial plasma applications. *9th Int. Symposium on Plasma Chemistry.* Pugnochiuso, Italy, p. 80.

50. Jiang, X.L., Tiwari, R., Gitzhofer, F. and Boulos, M.I. (1993) On the induction plasma deposition of tungsten metal *Journal of Thermal Spray Technology* **2,** 265-270.

51. Jackson, M.R., Siemers, P.A., Rutkowski, S.E. and Friend, G. (1998) Refractory metal structure produced by low pressure plasma deposition. G.E. Corporate R&D report 88 CRD 096.

52. Sugasawa, M., Kikukawa, N. and Ishikawa, N. (1995) Synthesis of Y-Fe-O ultrafine particles using RF thermal plasma. *J. Soc. Powder Technol. Japan* **32,** 660-667.

53. Sugasawa, M., Kikukawa, N., Ishikawa, N., Kayano, N. and Kimura, T. (1997)

Synthesis of Y-Fe-O ultrafine particles using inductively coupled plasma--the influence of precursor forms on products. *Journal of NIRE* **6,** 231-239.

54. Sugasawa, M., Kikukawa, N., Ishikawa, N., Kayano, N. and Kimura, T. (1998) Synthesis of Y-Fe-O ultrafine particles using inductively coupled plasma. *Journal of Aerosol Science* **29,** 675-686.

55. Watanabe, T., Nezu, A., Abe, Y., Ishii, Y. and Adachi, K. (2003) Formation mechanism of electrically conductive nanoparticles by induction thermal plasmas. *Thin Solid Films* **435,** 27-32.

56. Watanabe, T. and Fujiwara, K. (2004) Nucleation and growth of oxide nanoparticles prepared by induction thermal plasmas. *Chemical Engineering Communications* **191,** 1343-1361.

57. Suzuki, M., Kagawa, M., Syono, Y. and Hirai, T. (1991) Thin films of rare-earth (Y, La, Ce, Pr, Nd, Sm) oxides formed by the spray-ICP technique. *Journal of Crystal Growth* **112,** 621-627.

58. Suzuki, M., Kagawa, M., Syono, Y. and Hirai, T. (1992) Synthesis of untrafine single-component oxide particles by the spray-ICP technique. *Journal of Materials Science* **27,** 679-684.

59. Karthikeyan, J., Berndt, C.C., Tikkanen, J., Wang, J.Y., King, A.H. and Herman, H. (1997) Preparation of nanophase materials by thermal spray processing of liquid precursors. *Nanostructured Materials* **9,** 137-140.

60. Ishigaki, T., Oh, S.M., Li, J.G. and Park, D.W. (2005) Controlling the synthesis of TaC nanopowders by injecting liquid precursor into RF induction plasma. *Science and Technology of Advanced Materials* **6,** 111-118.

61. Li, J.G., Wang, X.H., Kamiyama, H., Ishigaki, T. and Sekiguchi, T. (2006) RF plasma processing of Er-doped TiO_2 luminescent nanoparticles. *Thin Solid Films* **506-507,** 292-296.

62. Bouyer, E., Gitzhofer, F. and Boulos, M.I. (1997) Suspension plasma spraying for hydroxyapatite powder preparation by RF plasma. *IEEE Transactions on Plasma Science* **25,** 1066-1071.

63. Kumar, R., Cheang, P. and Khor, K.A. (2001) RF plasma processing of ultra-fine hydroxyaptite powders. *Journal of Materials Processing Technology* **113,** 456-462.

64. Kumar, R., Cheang, P. and Khor, K.A. (2003) Radio frequency (RF) suspension plasma sprayed ultra-fine hydroxyapatite (HA)/zirconia composite powders.

Biomaterials **24,** 2611-2621.

65. Khor, K.A., Kumar, R. and Cheang, P. (2004) Process-phase-properties relationship in radio frequency (RF) plasma synthesized hydroxyapatite (HA). *Surface and Coatings Technology* **177-178,** 740-746.

66. Monterrubio-Badillo, C., Ageorges, H., Chartier, T., Coudert, J.F. and Fauchais, P. (2006) Preparation of $LaMnO_3$ perovskite thin films by suspension plasma spraying for SOFC cathodes. *Surface & Coatings Technology* **200,** 3743-3756.

67. El-Kaddah, N., McKelliget, J.W. and Szekely, J. (1984) Heat transfer and fluid flow in plasma spraying. *Metallurgical Transactions B* **15B,** 59-70.

68. Patankar, S.V. (1980) *Numerical heat transfer and fluid flow*. Hemisphere Publishing Corp.m McGraw-Hill Book Co., NY.

69. Launder, B.E. and Spalding, D.B. (1974) The numerical computation of turbulent flow. *Computer Methods in Applied Mechanics and Engineering* **3,** 269-289.

70. Dilawari, A.H., Szekely, J., Batdorf, J., Detering, R. and Shaw, C.B. (1990) The temperature profiles in an argon plasma issuing into an argon atmosphere: A comparison of measurements and predictions. *Plasma Chemistry and Plasma Processing* **10,** 321-337.

71. Brossa, M. and Pfender, E. (1988) Probe measurements in thermal plasma jets *Plasma Chemistry and Plasma Processing* **8,** 75-90.

72. Mostaghimi, J., Proulx, P. and Boulos, M.I. (1984) Parametric study of the flow and temperature fields in an inductively coupled plasma. *Plasma Chemistry and Plasma Processing* **4,** 199-217.

73. Mostaghimi, J. and Boulos, M.I. (1989) Two-dimensional electromagnetic field effects in induction plasma modelling *Plasma Chemistry and Plasma Processing* **9,** 25-44.

74. El-Hage, M., Mostaghimi, J. and Boulos, M.I. (1989) A turbulent flow model for the r.f. inductively coupled plasma. *Journal of Applied Physics* **65,** 4178-4185.

75. Chen, K. and Boulos, M.I. (1994) Turbulence in induction plasma modelling. *Journal of Physics D: Applied Physics* **27,** 946-952.

76. Ye, R., Proulx, P. and Boulos, M.I. (1999) Turbulence phenomena in the radio frequency induction plasma torch. *International Journal of Heat and Mass Transfer* **42,** 1585-1595.

77. Girshick, S.L. and Yu, W. (1990) Radio-frequency induction plasmas at atmospheric pressure: mixtures of hydrogen, nitrogen, and oxygen with argon.

Plasma Chemistry and Plasma Processing **10,** 515-529.

78. Paul, K.C. and Sakuta, T. (2000) Properties study of inductively coupled nitrogen plasmas and pressure effects on them. *Electric Power Systems Research* **56,** 185-193.

79. Takechi, K. and Lieberman, M.A. (2001) Effect of Ar addition to an O_2 plasma in an inductively coupled, traveling wave driven, large area plasma source: O_2/Ar mixture plasma modeling and photoresist etching. *Journal of Applied Physics* **90,** 3205-3211.

80. Atsuchi, N., Shigeta, M. and Watanabe, T. (2006) Modeling of non-equilibrium argon-oxygen induction plasma under atmospheric pressure. *International Journal of Heat and Mass Transfer* **49,** 1073-1082.

81. Watanabe, T., Shigeta, M. and Atsuchi, N. (2006) Two-temperature chemically-non-equilibrium modeling of argon induction plasmas with diatomic gas. *International Journal of Heat and Mass Transfer* **49,** 4867-4876.

82. Lee, S.H., Iza, F. and Lee, J.K. (2006) Particle-in-cell Monte Carlo and fluid simulations of argon-oxygen plasma: comparisons with experiments and validations. *Physics of Plasmas* **13,** 057102 1-9.

83. Cheng-Che Hsu, Mark A Nierode, JohnW Coburn and Graves, D.B. (2006) Comparison of model and experiment for Ar, Ar/O_2 and Ar/O_2/Cl_2 inductively coupled plasmas. *Journal of Physics D: Applied Physics* **39,** 3272-3284.

84. McKelliget, J.W., Trapaga, G., Gutierrez-Miravete, E. and Cybulsky, M. (1998) An integrated mathematical model of the plasma spraying process. In Christian Coddet, A.I., (ed.), *Thermal Spray: Meeting the Challenges of the 21st Century, 15th International Thermal Spray Conference.* Nice, France, Vol. 1.

85. Girshick, S.L. (1994) Particle nucleation and growth in thermal plasmas. *Plasma Sources Science and Technology* **3,** 388-394.

86. Proulx, P., Mostaghimi, J., and Boulos, M.I. (1985) Plasma-particle interaction effects in induction plasma modeling under dense loading conditions. *International Journal of Heat and Mass Transfer* **28,** 1327-1336.

87. Proulx, P., Mostaghimi, J. and Boulos, M.I. (1987) Heating of powder in an r.f. inductively coupled plasma under dense loading conditions. *Plasma Chemistry and Plasma Processing* **7,** 29-50.

88. Crowe, C.T., Sharma, M.P. and Stock, D.E. (1977) The particle-source-in-cell (PSI-CELL) for gas-droplet flows. *Journal of Fluids Engineering* **99,** 325-331.

89. Mckelliget, J.W. (1990) Numerical computation of coupled heat transfer, fluid flow, and electromagnetism: the inductively coupled plasma torch. In *Advanced computational methods in heat transfer*. Springer-Verlag, Vol. 3.

90. McFeaters, J.S., Stephens, R.L., Schwerdtfeger, P. and Liddell, M. (1994) Numerical modeling of titanium carbide synthesis in thermal plasma reactors *Plasma Chemistry and Plasma Processing* **14,** 333-360.

91. Desilets, M., Bilodeau, J.F. and Proulx, P. (1997) Modelling of the reactive synthesis of ultra-fine powders in a thermal plasma reactor. *Journal of Physics D: Applied Physics* **30,** 1951-1960.

92. Proulx, P., Mostaghimi, J. and Boulos, M.I. (1991) Radiative energy transfer in induction plasma modelling. *International Journal of Heat and Mass Transfer* **34,** 2571-2579.

93. Shigeta, M., Watanabe, T. and Nishiyama, H. (2004) Numerical investigation for nano-particle synthesis in an RF inductively coupled plasma. *Thin Solid Films* **457,** 192-200.

94. Xiong, H.B., Zheng, L.L., Sampath, S., Williamson, R.L., and Fincke, J.R. (2004) Three-dimensional simulation of plasma spray: effects of carrier gas flow and particle injection on plasma jet and entrained particle behavior. *International Journal of Heat and Mass Transfer* **47,** 5189-5200.

95. Versteeg, H.K. and Malalasekera, W. (1995) *An introduction to computational fluid dynamics--the finite volume method.* Harlow, Essex, England: Longman Scientific & Technical New York.

96. Launder, B.E. and Spalding, D.B. (1974) The numerical computation of turbulent flows. *Computer Methods in Applied Mechanics and Engineering* **3,** 269-289.

97. Cheary, R.W. and Coelho, A.A. (1992) A fundamental parameter approach to X-Ray line profile fitting. *Journal of Applied Crystallography* **25,** 109.

98. Maslen, E.N., Streltsov, V.A. and Ishizawa, N. (1996) A synchrotron X-ray study of the electron density in C-type rare earth oxides. *Acta Crystallographica Section B: Structural Science* **B52,** 414-422.

99. Marsella, L. and Fiorentini, V. (2004) Structure and stability of rare-earth and transition-metal oxides. *Physical Review* **B69,** 172103.

100. Schleid, T. and Meyer, G. (1989) Single crystals of rare earth oxides from reducing halide melts. *Journal of Less-Common Metals* **149,** 73-80.

101. Kim, Y.J. and Kriven, W.M. (1998) Crystallography and microstructural studies of

phase transformations in the Dy_2O_3 system. *Journal of Materials Research* **13,** 10.

102. Butherus, A.D. and Eick, H.A. (1973) Preparation, characterization and some thermodynamic properties of lanthanum oxide carbide, $La_2O_2C_2$. *Journal of Inorganic and Nuclear Chemistry* **35,** 1925.

103. Seiver, R.L. and Eick, H.A. (1976) The crystal structure of dilanthanum dioxide dicarbide, $La_2O_2C_2$. *Journal of Less-Common Metals* **44,** 1.

104. Schneider, S.J. and Roth, R.S. (1960) Phase equilibria in systems involving the rare-earth oxides. part II. solid state reactions in trivalent rare-earth oxide systems. *Journal of Research of the National Bureau of Standards* **64A,** 309-332.

105. Boulos, M.I., Fauchais, P. and Pfender, E. (1994) *Thermal plasmas: fundamentals and applications*. Plenum Press, New York.

106. McKelliget, J., Szekely, J., Vardelle, M. and Fauchais, P. (1982) Temperature and velocity fields in a gas stream exiting a plasma torch: a mathematical model and its experimental verification. *Plasma Chemistry and Plasma Processing* **2,** 317-332.

107. Magnussen, B.F. and Hjertager, B.H. (1976) On mathematical models of turbulent combustion with special emphasis on soot formation and combustion. *In 16th Symp. (Int'l.) on Combustion.*, The Combustion Institute.

108. Launder, B.E. and Spalding, D.B. (1974) The Numerical Computation of Turbulent Flows. *Computer Methods in Applied Mechanics and Engineering* **3,** 269-289.

109. Fluent Inc. (2001) *FLUENT user's guide*, Lebanon, NH 03766.

110. Petukhov, B.S. (1988) *Heat transfer in turbulent mixed convection*. Hemisphere Publishing 548 Corporation, USA.

111. Jayatilleke, C. (1969) *Progress in heat and mass transfer: the influence of Prandtl number and surface roughness on the resistance of the laminar sublayer to momentum and heat transfer*. Pergamon Press, New York.

112. Ang, C.B., Devasenapathi, A., Ng, H.W., Yu, S.C.M. and Lam, Y.C. (2001) A proposed process control chart for DC plasma spraying process. part II: experimental verification for spraying alumina. *Plasma Chemistry and Plasma Processing* **21,** 401-420.

113. Joshi, S.V. and Sivakumar, R. (1992) Prediction of in-flight particle parameters during plasma spraying of ceramic powders. *Material Science and Technology* **8,** 481-488.

114. Ahmed, I. and Bergman, T.L. (2000) Three-dimensional simulation of thermal plasma spraying of partially molten ceramic agglomerates. *Journal of Thermal Spray Technology* **9,** 215-224.

115. Ranz, W.E. and Marshall, W.R. (1952) Evaporation from drops. *Chemical Engineering Progress* **48,** 141-173.

116. Boulos, M.I. (1985) The inductively coupled R.F. (radio-frequency) plasma. *Pure and Applied Chemistry* **57,** 1321-1352.

117. Venkatachari, K.R. and Kriven, W.M. (1989) Investigation of plasma-sprayed dysprosia coatings. *Journal of the American Ceramic Society* **72,** 2023-2026.

118. Zinkevich, M. (2007) Thermodynamics of rare earth sesquioxides. *Progress in Materials Science* **52,** 597-647.

119. Park, C. (1989) A review of reaction rates in high-temperature air. *AIAA Paper* **89,** 1740.

120. Park, C. (1989) Assessment of two-temperature kinetic model for ionizing air. *Journal of Thermophysics and Heat Transfer* **3,** 233-244.

121. Park, J.H., Pfender, E. and Chang, C.H. (2000) Reduction of chemical reactions in nitrogen and nitrogen–hydrogen plasma jets flowing into atmospheric air. *Plasma Chemistry and Plasma Processing* **20,** 165-181.

122. Hoffert, M. and Lien, H. (1967) Quasi-one-dimensional nonequilibrium gas dynamics of partially ionized two-temperature argon. *Physics of Fluids* **10,** 1769-1777.

123. Sun, X.L., Tok, A.I.Y., Huebner, R. and Boey, F.Y.C. (2007) Phase transformation of ultrafine rare earth oxide powders synthesized by radio frequency plasma spraying. *Journal of the European Ceramic Society* **27,** 125-130.

124. Murphy, A.B. and Arundell, C.J. (1994) Transport coefficients of argon, nitrogen, oxygen, argon-nitrogen, and argon-oxygen plasmas. *Plasma Chemistry and Plasma Processing* **14,** 451-490.

125. Swihart, M.T. (2003) Vapor-phase synthesis of nanoparticles. *Current Opinion in Colloid and Interface Science* **8,** 127-133.

126. Flagan, R.C. and Lunden, M.M. (1995) Particle structure control in nanoparticle synthesis from the vapor phase. *Materials Science and Engineering* **A204,** 113-124.

127. Friedlander, S.K. (1977) *Smoke, dust and haze*. John Wiley, New York.

128. Girshick, S.L., Chiu, C.P., Muno, R., Wu, C.Y., Yang, L., Singh, S.K. and

McMurry, P.H. (1993) Thermal plasma synthesis of ultrafine iron particles. *Journal of Aerosol Science* **24,** 367-382.

129 Itoh, N., Sanchez, C.M.A., Xu, W.C., Haraya, K., and Hongob, M. (1993) Application of a membrane reactor system to thermal decomposition of CO_2, *Journal of Membrane Science*, **77**, 245-253.

130. Alvero, R., Bernal, A., Carrizosa, I., Odriozola, J.A. and Trillo, J.M. (1987) Thermochemical approach to hydration *Journal of Materials Science* **22,** 1517-1520.

131. Bernal, S., Botana, F.J., Garcia, R. and Rodriguez-Izquierdo, J.M. (1987) Behaviour of rare earth sesquioxides exposed to atmospheric carbon dioxide and water. *Reactivity of solids* **4,** 23-40.

132. Watanabe, T. and Fujiwara, K. (2004) Nucleation and growth of oxide nanoparticles prepared by induction thermal plasmas. *Chemical Engineering Communications* **191,** 1343-1361.

Publications

1. X.L.Sun, A.I.Y. Tok, F.Y.C. Boey & R. Huebner, "RF Plasma Processing of Ultrafine Sm-Lu Mixed Oxide Powders," *International Journal of Nanoscience,* Vol. 5 No. 4 & 5 (2006), pp. 487-491.
2. X.L. Sun, A.I.Y. Tok, R. Huebner & F.Y.C. Boey, "Phase transformation of ultrafine rare earth oxide powders synthesized by radio frequency plasma spraying," *Journal of the European Ceramic Society,* Vol. 27 (2007), pp. 125-130.
3. A.I.Y. Tok, F.Y.C. Boey, Z. Dong & X.L Sun, "Hydrothermal Synthesis of CeO_2 Nano-Particles," *Journal of Materials Processing Technology,* Vol. 190 (1-3) (2007), pp. 217-222.
4. X.L. Sun, A.I.Y. Tok, F.Y.C. Boey & C.L. Gan, "Solvent and Plasma Gas Influence on the Synthesis of Y_2O_3 Nanoparticles by Suspension Plasma Spraying," *Journal of Materials Research*, Vol. 22(5) (2007), pp. 1-8.
5. X.L. Sun, C.W. Kang, A.I.Y. Tok, H.W. Ng, S.L. Lim, and F.Y.C. Boey. "Combustion-aided Suspension Plasma Spraying of Y_2O_3 Nanoparticles—Synthesis and Modeling". *Journal of Applied Physics*, Vol. 103 (2008), pp. 1-13.
6. R. Huebner, X.L. Sun, A.I.Y. Tok, and F.Y.C. Boey. "Phase characterization of Sm-Lu mixed oxide powders prepared by sintering and radio frequency plasma spraying". *Journal of the European Ceramic Society*. Under review.

Appendix I

Energy Source Calculation

Power Output Calculation

Based on the operating conditions stated in Table 3.3 and 3.5

Power input = I E = 22 kW

With torch efficiency of 67%,

Power output = 22 × 0.67 = 14.74 kW

Geometry Dimension

Torch dimension (diameter × length) = 35 × 109 mm

Torch volume = $(\pi R^2 - \pi r^2) \times L = [\pi (0.035/2)^2 - \pi (0.00267/2)^2] \times 0.037$

$$= 3.539101 \times 10^{-5} \text{ m}^3$$

Energy Source

Energy source needed for FLUENT© calculation is energy per unit volume.

$$\frac{\text{Engergy}}{\text{Volume}} = \frac{14.74 \times 10^3}{3.539101 \times 10^{-5}} = 4.164901 \times 10^8 \text{ W} \cdot \text{m}^{-3}$$

Appendix II

Derivation of General Form of Governing Differential Equation for Plasma Flow

The rate of change of x-momentum of the fluid element equals the total force in the x-direction on the element due to surface stresses and the rate of increase of x-momentum due to sources; the x-component of the momentum equation is as follows:

$$\frac{\partial(\rho u)}{\partial t} + \nabla \cdot (\rho \boldsymbol{u} u) = \frac{\partial(-p + \tau_{xx})}{\partial x} + \frac{\partial \tau_{yx}}{\partial y} + \frac{\partial \tau_{zx}}{\partial z} + S_{Mx} \tag{A.1}$$

In a Newtonian fluid, the viscous stresses are proportional to the rates of deformation. In the case of incompressible flow, the nine viscous stress components, of which six are independent, are:

$$\tau_{xx} = 2\mu \frac{\partial u}{\partial x} \tag{A.2}$$

$$\tau_{yy} = 2\mu \frac{\partial v}{\partial y} \tag{A.3}$$

$$\tau_{zz} = 2\mu \frac{\partial w}{\partial z} \tag{A.4}$$

$$\tau_{xy} = \tau_{yx} = \mu \left(\frac{\partial u}{\partial y} + \frac{\partial v}{\partial x} \right) \tag{A.5}$$

$$\tau_{xz} = \tau_{zx} = \mu \left(\frac{\partial u}{\partial z} + \frac{\partial w}{\partial x} \right) \tag{A.6}$$

$$\tau_{yz} = \tau_{zy} = \mu \left(\frac{\partial v}{\partial z} + \frac{\partial w}{\partial y} \right) \tag{A.7}$$

Substituting Eqs. (A.2) to (A.7) into Eq. (A.1) gives

$$\frac{\partial(\rho u)}{\partial t}+\nabla\cdot(\rho \boldsymbol{u} u)=-\frac{\partial p}{\partial x}+\frac{\partial}{\partial x}\left(2\mu\frac{\partial u}{\partial x}\right)+\frac{\partial}{\partial y}\left[\mu\left(\frac{\partial u}{\partial y}+\frac{\partial v}{\partial x}\right)\right]+\frac{\partial}{\partial z}\left[\mu\left(\frac{\partial u}{\partial z}+\frac{\partial w}{\partial x}\right)\right]$$

$$+S_{Mx} \tag{A.8}$$

$$\frac{\partial(\rho u)}{\partial t}+\nabla\cdot(\rho \boldsymbol{u} u)=-\frac{\partial p}{\partial x}+\frac{\partial}{\partial x}\left(\mu\frac{\partial u}{\partial x}\right)+\frac{\partial}{\partial y}\left(\mu\frac{\partial u}{\partial y}\right)+\frac{\partial}{\partial z}\left(\mu\frac{\partial u}{\partial z}\right)$$

$$+\left[\frac{\partial}{\partial x}\left(\mu\frac{\partial u}{\partial x}\right)+\frac{\partial}{\partial y}\left(\mu\frac{\partial v}{\partial x}\right)+\frac{\partial}{\partial z}\left(\mu\frac{\partial w}{\partial x}\right)\right]+S_{Mx} \tag{A.9}$$

$$\frac{\partial(\rho u)}{\partial t}+\nabla\cdot(\rho \boldsymbol{u} u)=-\frac{\partial p}{\partial x}+\nabla\cdot(\mu\nabla u)+S_{Mx} \tag{A.10}$$

For a steady, turbulent flow and without additional source to increase the momentum in x-direction, Eq. (A.10) can be rewritten as

$$\nabla\cdot(\rho \boldsymbol{u} u) = \nabla\cdot[(\mu_l+\mu_t)\nabla u]-\frac{\partial p}{\partial x} \tag{A.11}$$

Comparing Eq. (A.11) with the general form of governing equation given in Eq. (1),

$$\nabla\cdot(\rho \boldsymbol{u}\Phi) = \nabla\cdot(\Gamma_\Phi\nabla\Phi) + S_\phi \tag{1}$$

the diffusion coefficient, Γ_Φ equals $\mu_l+\mu_t$ and the source term contains $-\frac{\partial p}{\partial x}$.